Materials Science and Engineering B 192 (2015) 52–82

Contents lists available at ScienceDirect

Materials Science and Engineering B

journal homepage: www.elsevier.com/locate/mseb

Review

Mechanisms of aging and fatigue in ferroelectrics

Yuri A. Genenko[a], Julia Glaum[b], Michael J. Hoffmann[c], Karsten Albe[a,*]

[a] Sonderforschungsbereich 595, Institut für Materialwissenschaft, Technische Universität Darmstadt, Alarich-Weiss-Str. 2, 64287 Darmstadt, Germany
[b] Department of Materials Science and Engineering, University of New South Wales, Sydney, Australia
[c] Institut für keramische Werkstoffe, Haid-und-Neu Str. 7, Karlsruhe Institute of Technology, 76131 Karlsruhe, Germany

ARTICLE INFO

Article history:
Received 4 July 2014
Received in revised form
24 September 2014
Accepted 8 October 2014
Available online 22 October 2014

ABSTRACT

A comprehensive review of aging and fatigue phenomena in bulk polycrystalline ferroelectrics is presented. Three material classes are covered, namely the most widely used $Pb[Zr_{1-x}Ti_x]O_3$ (PZT) ceramics and lead-free materials, including those based on bismuth sodium titanate $Bi_{1/2}Na_{1/2}TiO_3$ (BNT) and alkali niobate $[K_xNa_{1-x}]NbO_3$ (KNN). Aging is studied in poled and unpoled states both experimentally and theoretically. The variety of different loading regimes for fatigue includes DC electric field, unipolar, sesquipolar and bipolar cycling and all these differently combined with mechanical loading at different frequencies and temperatures. The role of device geometries and electrode materials is addressed and models describing charge migration and defect dipole re-orientation are discussed in the context of recent experimental studies.

© 2014 Elsevier B.V. All rights reserved.

Contents

1. Introduction 53
 1.1. Relevant material systems 53
 1.2. Characterization of domain structures and defect dipoles 55
 1.3. Aging and fatigue concepts 56
2. Fatigue: experimental results 57
 2.1. Large-signal and small-signal parameters 57
 2.2. Unipolar, bipolar, sesquipolar and DC conditions 58
 2.3. Influence of temperature 60
 2.4. Cycling with electromechanical loading 61
 2.5. Frequency and cycle number 61
 2.6. Electrodes 61
 2.7. Sample geometry – actuators 62
 2.8. Experimental verification of fatigue models 63
  2.8.1. Boundary effects 64
  2.8.2. Cycling at large fields and high temperatures 64
  2.8.3. Results from piezo force microscopy (PFM) 65
  2.8.4. Results from in-situ X-ray diffraction analysis (XRD) 66
3. Aging and de-aging: experimental results 67
4. Point defects and dipoles 70
 4.1. Defect formation 70
 4.2. Dipole formation 71
 4.3. Dipole switching 73

* Corresponding author. Tel.: +49 6151 166374; fax: +49 6151 166263.
E-mail addresses: albe@mm.tu-darmstadt.de, K.Albe@web.de (K. Albe).

http://dx.doi.org/10.1016/j.mseb.2014.10.003
0921-5107/© 2014 Elsevier B.V. All rights reserved.

5. Drift-diffusion models 75
5.1. Charge migration model for aging 75
5.2. 2D drift-diffusion model of aging in unpoled ceramics 75
5.3. 3D drift-diffusion model of aging in poled ceramics 77
5.4. Space charge effects in ferroelectrics with semiconducting features 77
5.5. Phase-field modeling of ferroelectrics with semiconducting features 78
6. Summary 79
6.1. Aging 79
6.2. Fatigue 79
Acknowledgements 80
References 80

1. Introduction

Piezoelectric devices, combined with the development of ferroelectric ceramics, have become a key enabling technology for a wide range of industrial and consumer applications such as transducers, filters, sensors, ultrasonic motors or actuators [1–5]. Common to all ferroelectric ceramics is a phase transformation upon cooling from the sintering temperature. The formation of a spontaneous polarization and a transition from paraelectric to ferroelectric behavior is observed at the Curie point. Mechanical stresses and depolarization fields induced by the spontaneous polarization are relaxed by the formation of domains, which are defined as homogeneous areas of the material with the same polarization orientation. Sintered ceramics do not exhibit a macroscopic polarization, but the domains can be reoriented by applying an electric field (poling) resulting in a remnant polarization as well as dimensional changes of the ceramic [6]. Most of the aforementioned devices operate under small signal conditions. This means that the driving voltage during service is much smaller compared to the electric field applied during poling and the domain configuration does not alter significantly. The optimization of the material parameters for small signal devices is driven by requirements regarding dielectric properties, coupling factor, temperature or frequency dependence, mechanical quality factors, etc. When high strains are desired, as in the case of actuators, the operating fields become comparable to the poling conditions (1–4 kV/mm). In addition to the piezoelectric effect, a large contribution to the strain originates from domain reorientation [7]. The interest in ferroelectric materials operating under these large signal conditions has strongly increased due to needs of the automotive and aerospace industry as well as other industrial areas in high precision positioning systems. One example are piezoelectric driven injection systems for diesel and more recently also directly injected gasoline engines [8], which are now commercially available on the European market [9–11].

All devices are subject to different loading modes and cycle numbers. Thus, requirements on material performance, device design, and drive control are equally diverse. As ferroelectric ceramics are system-enabling components, long-term reliability is of paramount industrial concern. Two major phenomena have to be considered during life time of a device: aging [12] and fatigue [13]. The first one describes gradual changes of materials properties with time under external equilibrium conditions, whereas the latter one is characterized by a gradual change of the properties during service. While aging is more related to the composition of a ferroelectric ceramic, fatigue depends on loading conditions and could only be observed for high electric fields.

Most of the piezoelectric devices used nowadays rely on ferroelectric ceramics and these are still based on $Pb[Zr_{1-x}Ti_x]O_3$ (PZT), although it is known that lead compounds are toxic and harmful. The main reason for that are the superior piezoelectric properties of PZT ceramics over an extended range of operation temperatures. Furthermore, by doping with additives the properties can be adjusted in a wide range to meet the required specifications during operation. However, because of the toxicity of PZT, the European Union (EU) in 2003 included PZT in its directive "Restriction of the use of certain Hazardous Substances in electrical and electronic equipment (RoHS)" to be substituted as a hazardous substances by safer materials [14,15]. This directive gave a boost to the search for lead-free piezoceramics [16]. Heretofore, most commonly known lead-free materials can be divided into bismuth sodium titanate $[Bi_{1/2}Na_{1/2}]TiO_3$ (BNT) based ones and alkali niobate $[K_xNa_{1-x}]NbO_3$ (KNN) containing ones. Consecutively, these three material systems will be briefly introduced and compared.

1.1. Relevant material systems

All three material families crystallize in the perovskite structure. The corresponding phase diagrams are indicated in Fig. 1.

$Pb[Zr_{1-x}Ti_x]O_3$ is known as a solid solution between lead titanate and lead zirconate that exhibits its highest macroscopic piezoelectric properties at the morphotropic phase boundary (MPB) near $x = 0.48$ (Fig. 1a). The MPB has been assigned as a coexistence region of a tetragonal Ti-rich phase and a Zr-rich rhombohedral phase. More recently, detailed structural investigations indicated a monoclinic symmetry for the Zr-rich phase near the MPB [18,19], which is also often related to the formation of nanodomains [18]. Glazer et al. go even one step further and claim that all three structurally different regions can be described by a monoclinic symmetry, when the structures are considered on a suitably small length scale [20]. Regardless of structural refinement details, technically used PZT solid solutions are always modified with dopants. The quantity and type of dopants determine the piezoelectric properties, but also aging and fatigue behavior. Depending on the type of aliovalent doping, two major defect types have to be considered. In case of acceptor doping Pb- or (Ti, Zr)-ions are substituted by ions of lower valence. Charge neutrality will be ensured by formation of oxygen vacancies. Donor doping creates lead vacancies upon substitution of Pb- or (Ti, Zr)-ions with ions of higher valence [6]. Many technical PZT compositions have more than one dopant element and very often combine acceptor and donor doping at the same time to meet the requirements for a certain application [21]. The amount and type of doping can also shift the MPB by a few mole percent and will influence the Curie temperature.

Fig. 1b shows the phase diagram for $[Bi_{1/2}Na_{1/2}]TiO_3$–$BaTiO_3$ (BNT–BT) which is a typical representative for Bi-based ceramics with perovskite structure. The MPB that separates a Bi-rich rhombohedral phase from a Ba-rich tetragonal phase is accompanied by a significant enhancement in dielectric permittivity, electromechanical coupling factor k [22,17], and piezoelectric properties [23,24] similar as for PZT. However, with increasing temperature both ferroelectric phases transform first into an antiferroelectric phase before they form a paraelectric cubic phase above the Curie temperature. The existence of the antiferroelectric phase [17] is controversially discussed and often also described as a relaxor-type phase consisting of polar and non-polar regions [25,26].

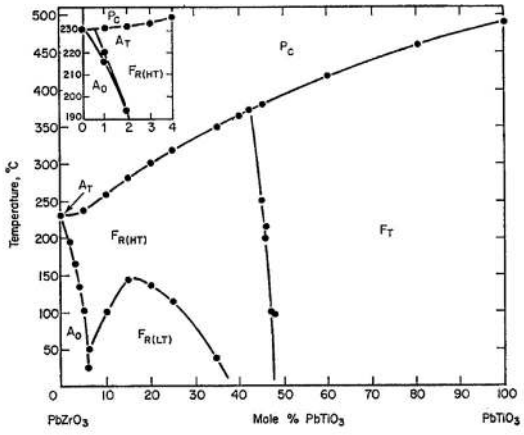

(a) $Pb[Zr_{1-x}Ti_x]O_3$ (PZT) (from Ref. [6])

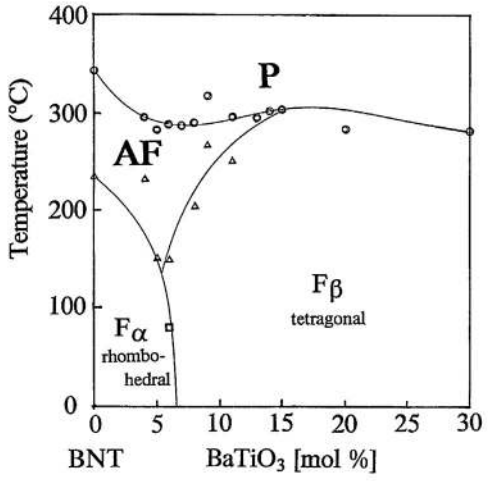

(b) $[Bi_{1/2}Na_{1/2}]TiO_3$–$BaTiO_3$ (BNT-BT) (from Ref. [17])

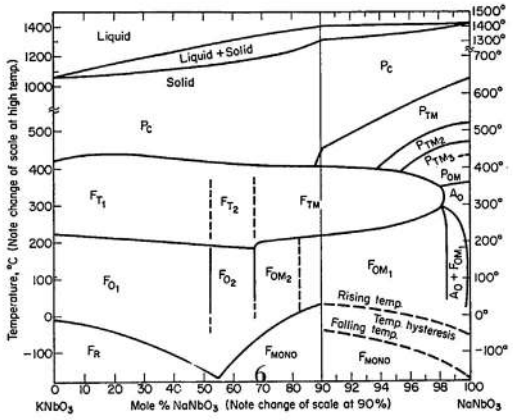

(c) $[K_x,Na_{1-x}]NbO_3$ (KNN) (from Ref. [6])

Fig. 1. Pseudo-binary phase diagrams for the technological most relevant ferroelectric ceramics.

Independent of structural details the phase transition from ferroelectric to antiferroelectric is associated with a vanishing lattice distortion and a macroscopic depolarization. Furthermore, the course of depolarization temperature, limiting the maximum operation temperature of the ferroelectric material, reveals a deep cusp at the MPB, which means that the most efficient material compositions exhibit the lowest thermal stability. Material properties of BNT–BT ceramics can be further tuned by substituting Na by K [27–30], by adding small amounts of KNN [31,32], or by doping with Ta [22]. The addition of KNN and Ta results in a significant increase of the field-induced strain with values up to 0.45% [31], but only in a very narrow temperature and compositional range, probably due to a drop of the cusp at the MPB down to room temperature. This also explains why these materials do not show any domains [32] unless a high electric field is applied that induces a lattice distortion [33]. It should be also mentioned that ceramics containing KNN reveal an ergodic behavior at room temperature which means that the field induced lattice distortion vanishes again after the electric field is released, whereas BNT–BT ceramics without KNN show non-ergodic behavior with a remaining ferroelectric phase after the first poling. Despite some similarities between BNT–BT and PZT with respect to the MPB, the influence of additives or dopants seems to be quite different. In BNT–BT they strongly modify the depolarization temperature and thereby the phase equilibria, whereas in PZT they directly alter the defect chemistry and thus the number and type of mobile charge carriers. So far it is not clear whether similar doping concepts can be applied to BNT–BT-type ceramics.

The phase diagram of KNN (Fig. 1c) shows a complete solid solution between potassium niobate (KN) and sodium niobate (NN) and three MPBs separating 4 orthorhombic phases. More recent structural refinements including neutron diffraction measurements show that the orthorhombic symmetries are indeed monoclinic [34,35]. The end member NN is antiferroelectric and therefore not further considered. Because of the relatively small differences between the orthorhombic structures, the MPBs do not have a very strong impact on materials properties. Nevertheless, most KNN-based ceramics have approximately equal molar ratios of NN and KN with enhanced ferroelectric properties [36]. A characteristic feature of KNN is the nearly composition-independent polymorphic phase transformation (PPT) from orthorhombic to tetragonal (O → T) at ≈200 °C. This PPT leads to a much stronger enhancement of the piezoelectric properties compared to the three MPBs between the different orthorhombic phases since it is associated with a rotation of the polarization vector from $\langle 1\,1\,0\rangle_c$ to $\langle 0\,0\,1\rangle_c$. This is in agreement with the analysis of Damjanovic [37] showing the similarity of the Gibbs free energy profiles of composition dependent (MPB) and temperature dependent (PPT) phase transformations, when a polarization rotation is involved.

In order to improve the piezoelectric properties of KNN-based ceramics Saito et al. [38] investigated the substitution of A-site elements (alkali) by Li and the substitution of the B-site element (Nb) by Ta and Sb and obtained a substantial enhancement of d_{33} from 160 pC/N for pure KNN to 300 pC/N [22]. The results initiated an enormous research activity for further enhancement of the piezoelectric properties. A comprehensive overview on the most relevant findings was given by Rödel et al. [16]. Common to all investigations is the isovalent cation substitution, which does not create any point defects or electronic defects. The origin of the increase in piezoelectric properties is ascribed to a shift of the (O → T) phase transformation down to room temperature, which is associated with a pronounced temperature dependence. The additional impact of the poling state on the piezoelectric properties of modified KNN has been analyzed by Morozov et al. [39]. They obtained a further enhancement of the unipolar strain and dielectric constant for orthorhombic KNN, when the material is poled in the tetragonal state. These enhanced properties can be preserved in a metastable state for applied fields smaller than the coercive field.

There are only a few attempts to transfer the known concepts of PZT for donor and acceptor doping to KNN-based materials. Morozov et al. [40] studied aliovalent Ba- and Mn-doping in modified KNN-ceramics and found that the AC conductivity can be varied by several orders of magnitude by heat treatments under different oxygen partial pressures. The results are explained in

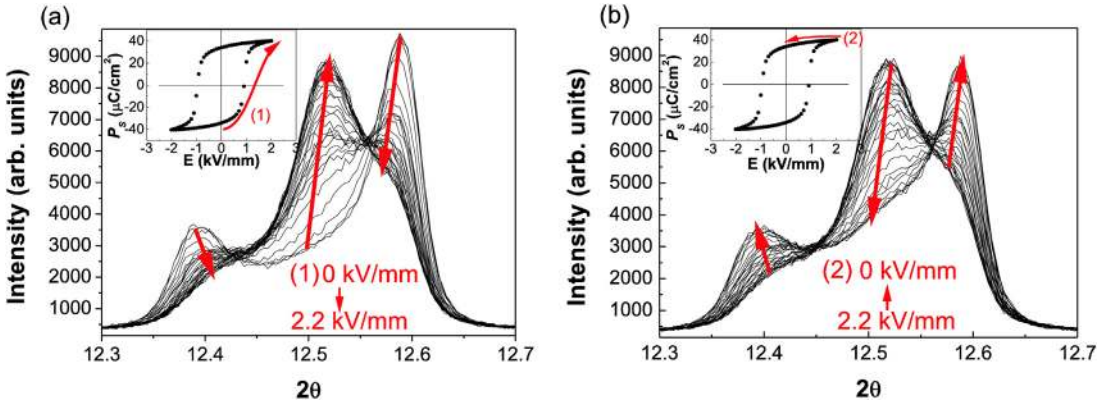

Fig. 2. Influence of the applied electric field on the $0\,0\,2_t$ reflection, (a) from 0 to 2.2 kV/cm and (b) from 2.2 to 0 kV/cm. The insets show the position in the corresponding hysteresis cycle for the same range of electric field (1)–(2) (Hinterstein et al. [48]).

terms of defect chemistry by the formation of oxygen vacancies and electronic defects. Strain measurements show indeed a reduced mobility of 90° domain walls corresponding to a hardening effect. Hagh et al. [41] also analyzed doping of modified KNN with up to 2.0 mol% Ba, but observed a softening effect. Copper is another additive that has been studied intensively to analyze its impact on densification and piezoelectric properties of KNN and (Li,Ta,Sb)-modified KNN [42–44]. Hagh et al. [44] proposed that Cu is incorporated into the perovskite structure and modifies the piezoelectric properties. B-site substitution would lead to the formation of oxygen vacancies, which could explain the higher mechanical quality factor and the decrease in remnant polarization. Since the coercive field is also decreasing, however, they assume that Cu also partially substitutes the A-site. This in agreement with ab-initio calculations that show a preferred B-site occupancy for Cu, but also some probability to occupy the A-site when the material is processed in reducing atmospheres [45]. Sintering studies and EPR measurements indicate a relatively small Cu solubility in the KNN-lattice and confirm a B-site occupancy as well as the formation of oxygen vacancies that form defect dipoles with Cu [46,47].

In summary, a decisive control of the defect chemistry to create softening and hardening of the piezoelectric properties similar to PZT ceramics is not yet achieved for the currently discussed lead-free systems with perovskite structure. First attempts have been made with KNN and modified KNN by adding Ba and Cu, but the effects are small compared to PZT. The majority of the investigations in case of Bi-based ceramics focus on isovalent doping and therefore the formation of solid solutions. Information on the generation of defects or defect dipoles, which are relevant for aging and fatigue of a material, is still rare.

1.2. Characterization of domain structures and defect dipoles

Recent progress in the development of advanced and resolution enhanced characterization methods provides new insights in the material behavior leading to a better understanding of the aging and fatigue mechanisms. This chapter will not cover standard methods well known to a materials scientist, instead it is focussing on techniques particularly useful for ferroelectric ceramics. They can be divided in imaging techniques, diffraction techniques, and spectroscopic methods. Frequently used imaging techniques for ferroelectrics are the piezoelectric force microscopy (PFM) [49,50] and transmission electron microscopy (TEM) equipped with sample holders to apply an electric field or to heat the specimen [51–55]. Both techniques permit not only a direct visualization of ferroelectric domains, but also in-situ observations of pressure-, electric field-, or temperature-induced domain wall movements. Electric field induced in-situ X-ray and neutron diffraction experiments combined with in-situ TEM observations form the basis to deduce new models for the enhanced piezoelectric properties of PZT and lead-free ceramics. For PZT it was shown that the tetragonal and rhombohedral domain features change in the coexistence region of both phases at the MPB and nanodomains are formed [56]. These nanodomains are often described as monoclinic on a larger length scale according to high resolution synchrotron data first published for undoped PZT by Noheda et al. [57–59]. However, the monoclinic phase can be interpreted as tetragonal, monoclinic, or rhombohedral depending on the structural parameters [56]. Hinterstein et al. [48] correlate the macroscopic ferroelectric properties of PZT with the structural changes during electrical loading by using high resolution synchrotron radiation. For a commercial PZT material with a composition near the MPB, they could show an electrical field induced phase transformation from tetragonal to monoclinic (Fig. 2). At the maximum loading (2.2 kV/mm), the volume fraction of the monoclinic phase has increased by 15%. The phase transformation is fully reversible when the electric field is switched off. These experiments give for the first time an experimental evidence of a field induced phase transformation at the MPB which could explain the well-known maximum of the piezoelectric properties for PZT compositions near the MPB.

Another most useful technique for ferroelectric ceramics, but on a different length scale, compared to X-ray diffraction and TEM, is the electron paramagnetic resonance (EPR) spectroscopy. It is a sensitive local probe for ceramics containing paramagnetic elements as dopants or impurities that does not only provide information about the element itself, but also about its immediate surrounding. Therefore, EPR is predestinated for the characterization of defect dipoles. Typical results show that dopants like copper or iron substitute as acceptor centers for (Zr,Ti) in PZT [60–62] or (Nb) in KNN [63]. A more detailed analysis indicates that oxygen vacancies $V_O^{\bullet\bullet}$ may form charged defect associates $(Fe'_{Ti} - -V_0^{\bullet\bullet})^{\bullet}$ with iron functional centers in acceptor doped PZT, whereas for copper neutral associates $(Cu''_{Ti} - V_0^{\bullet\bullet})^{x}$ are observed [64]. It was also possible to prove that charge compensation in case of donor doping of lead titanate (PT) with rare earth elements occurs only by generating lead vacancies V''_{Pb} [65]. EPR can also provide information on interactions between different types of aliovalent dopants as it is the case in co-doped PZT ceramics. Based on EPR measurements on Fe-containing co-doped PZT, Eichel et al. [66] postulate the existence of $(Fe'_{Ti} - V_0^{\bullet\bullet})^{\bullet}$ defect dipoles as it is known from acceptor-doped PZT. The corresponding spectra for a (Gd,Fe) doped PZT are shown in Fig. 3. The $(Fe'_{Ti} - V_0^{\bullet\bullet})^{\bullet}$ defect dipole can take two different arrangements with respect to the direction of the spontaneous polarization. Oxygen vacancies ($V_0^{\bullet\bullet}$) in one of the equatorial positions of the

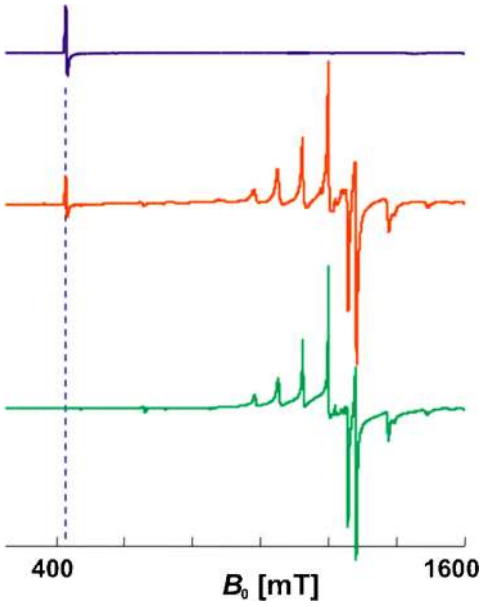

Fig. 3. Q-band (34 GHz) EPR spectra of purely Fe-doped PT (top), (Gd,Fe) co-doped PT (center) and purely Gd-doped PT (bottom): resonance at 420 mT (marked by vertical dashed line) is indicative for presence of $(Fe'_{Ti}–V_O^{\bullet\bullet})^{\bullet}$ defect associates (Eichel et al. [66]).

oxygen octahedra generate a $(Fe'_{Ti} - V_O^{\bullet\bullet})^{\bullet}$ defect dipole perpendicular to the spontaneous polarization, whereas $V_O^{\bullet\bullet}$ in the apical oxygen positions form defect dipoles collinear to the orientation of spontaneous polarization. Both arrangements were found in (La,Fe) co-doped PZT [67]. Changes in the position of the $V_O^{\bullet\bullet}$ within the oxygen octahedron via ionic hopping processes will result in a reorientation of the corresponding dipole [68]. It is interesting to mention that the macroscopic piezoelectric properties of co-doped PZT with charged defect dipoles are comparable to soft PZT as long as the concentration of donor dopants exceeds the acceptor dopant concentration.

The quality of characterization of charged point defects can be significantly enhanced by combining EPR analysis with calculations based on electronic density functional theory (DFT) which are both efficient and sufficiently reliable for assessing the energetics of point defect and associates. DFT calculations are able to cover important aspects such as the dependence of the formation energies on the Fermi level and the charge state for acceptor-doped PZT [69,68] and for Cu-doped KNN [45]. Calculated spin density patterns of different defects can be directly compared to EPR measurements, which give more reliable interpretations of the experimental data [64].

1.3. Aging and fatigue concepts

Ferroelectric ceramics are subject to degradation either during electrical loading (fatigue) or with time in the absence of an external mechanical or electrical load (aging). The underlying mechanisms of both are quite similar and closely related to point defects that are introduced intentionally by doping with aliovalent ions or unintentionally by impurities from the raw materials used to prepare the ceramics. Relevant defects are donor or acceptor dopants and mobile vacancies, electrons or holes. The dopants may form defect dipoles with vacancies as pointed out earlier. Fig. 4 shows a typical macroscopically detectable degradation of the piezoelectric properties due to either fatigue or aging of a ferroelectric ceramic. The aging phenomenon is most clearly visible in a pinching of the polarization hysteresis loop (Fig. 4a) of acceptor-doped materials [12,70,71]. Fatigue results in a reduction of the

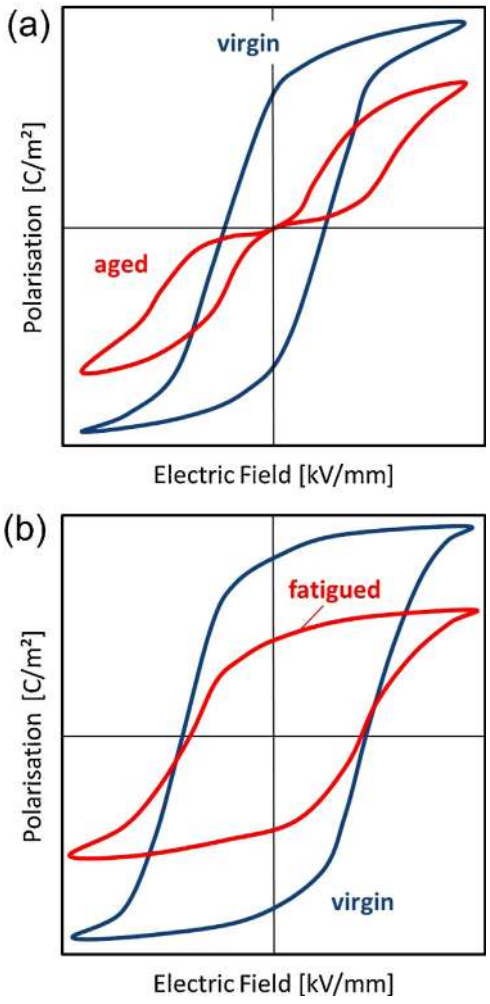

Fig. 4. Schematics of the macroscopic degradation behavior in a ferroelectric ceramic: aging (a) and fatigue (b).

remnant polarization during bipolar electric cycling of predominantly donor-doped materials with electric fields larger than the coercive field (Fig. 4b) [72].

The microscopic mechanisms causing fatigue and aging of ferroelectric ceramics are still under debate. Since the early 1970s three major mechanisms have been discussed. Common to all of them is that mobile charged defects stabilize a given domain configuration thereby generating an internal bias field that counteracts the polarization reversal when an electric field is applied. Carl and Härdtl [12] denoted three mechanisms as: (i) volume effect, (ii) domain effect and (iii) grain boundary effect according to their different length scales (Fig. 5). The volume effect is associated with defect dipoles mostly formed by an acceptor ion and an oxygen vacancy (Fig. 5a) having an electric dipole moment as well as an elastic dipole moment due to the deformation of the unit cell [73–75]. It occupies an energy minimum, but can be reoriented through the displacement of the oxygen vacancy within the octahedron as shown experimentally by EPR [76]. The domain effect describes a diffusion of charged defects to domain walls leading to pinning of their positions (Fig. 5b). The driving force is again a minimization of the local electric or elastic energy [77,78]. The interface effect involves the diffusion of ions, vacancies or electrons to grain boundaries or interfaces between dissimilar phases (electrodes, second phases) to form space charge layers (Fig. 5c) [79]. This effect is discussed in more detail in chapter 5. The formation of microcracks in the region close to the electrode, as also shown in Fig. 5c, is an

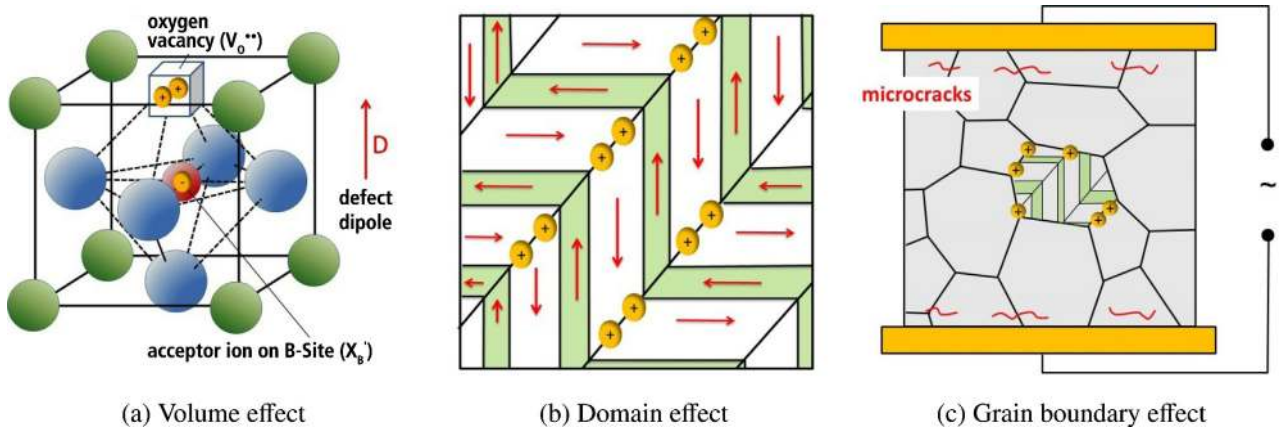

Fig. 5. Classification of the different domain stabilization mechanisms according to their length scales and irreversible microstructural changes.

additional and irreversible degradation mechanism, but only relevant for fatigue and not for aging. The scope of this paper is a critical review of the proposed mechanisms for aging and fatigue of ferroelectric ceramics. In Sections 2 and 3 we first summarize experimental data on fatigue and aging of PZT and lead-free compounds. In Sections 4 and 5 theoretical results of defects, volume and interface effects are presented before we conclude with a summary of the most dominant degradation mechanisms.

2. Fatigue: experimental results

The characteristics of fatigue degradation are determined by both the material's composition as well as the specific boundary conditions. This includes experimental factors such as applied electric field amplitude or frequency as well as sample specific factors such as electrode material or sample geometry. Additionally, it has to be distinguished between ferroelectric ceramics (which include non-ergodic relaxors transformed into a stable ferroelectric state after first field application) exhibiting a permanent domain structure and ergodic relaxors, which only exhibit a long-range order and consequently a domain structure during electric field application. The following sections will first introduce the relevant parameters used to describe fatigue effects and then give an overview of the relationship between fatigue conditions and observed degradation features. Where necessary the specific features of ergodic relaxors will be highlighted.

2.1. Large-signal and small-signal parameters

The characterization of ferroelectric ceramics under high electric fields is commonly based on a set of four parameters: polarization P, strain S, permittivity ε_{33} and piezoelectric coefficient d_{33} (see Fig. 6). Polarization and strain are called large-signal parameters, as they are only generated by high voltages applied. During measurement only the change of polarization and strain can be captured such that the measured values always depend on the initial state of the sample. For comparability the polarization loop in Fig. 6 is centered at the zero point along the ordinate, whereas for the strain hysteresis the zero point is often chosen to be the value at zero electric field or the minimum of the whole loop. Several parameters can be extracted from the large-signal loops, which help to characterize the material.

- remnant polarization $P_r^{+/-}$ and switchable polarization $2P_r$:
  By proper definition the remnant state is the residual polarization after first electric field application to a virgin sample. Switching the polarization state from anti-parallel to parallel orientation to the poling field can lead to different values. However, the term "remnant polarization" is widely used in the literature to describe the residual polarization state after electric field application in general and will be used as such in this manuscript. From the negative and positive remnant polarization the switchable polarization $2P_r$ can be calculated: $2P_r = P_r^+ + |P_r^-|$
- Coercive field $E_c^{+/-}$ and bias field E_{bias}:
  The coercive field $E_c^{+/-}$ is the threshold field at which most of the polarization reversal processes are initiated. It can be extracted from the polarization loops by taking the electric fields at which the polarization becomes zero. However, as the polarization is measured relative to the initial state, polarization offsets are obscured and false E_c values might be read out. An alternative source for E_c is the current density j, which is related to the polarization as such: $j = dP/dt$ (see Fig. 7). The maximum current density occurs at the coercive field. From the coercive field values E_c^+ and E_c^- the internal bias field $E_{\text{bias}} = (E_c^+ + E_c^-)/2$ can be calculated indicating a shift of the polarization loop along the abscissa [81].
- Maximum strain difference $\Delta S^{+/-}$ and asymmetry factor γ_S:
  The maximum strain difference can be extracted from the strain hysteresis loop, which is just the difference between the strain at maximum electric field applied and the strain minimum under same polarity of the electric field. These values are used to calculate the asymmetry factor $\gamma_S = (\Delta S^+ - \Delta S^-)/(\Delta S^+ + \Delta S^-)$ to quantify non-symmetric developments of the strain under positive compared to negative electric fields [81].

In contrast to the large-signal parameters the small-signal parameters permittivity ε and piezoelectric coefficient d are absolute values. They show the dependence of polarization and strain, respectively, on a small AC excitation field. The amplitude of the excitation field determines if the small-signal parameters reflect intrinsic and reversible domain wall contributions only or if irreversible components add to them as well [82,83]. For bulk ceramics the small signal values are mostly measured parallel to the applied electric field such that ε_{33} and d_{33} are the reported values, in which the permittivity is usually given relative to the permittivity of free space ε_0. The following characteristic parameters are extracted from the small-signal values:

- remnant permittivities $\varepsilon_{33,r}^{+/-}$, maximum permittivity difference $\Delta\varepsilon_{33}^{+/-}$ and asymmetry factor γ_ε:
  As described above the remnant values reflect the residual state after high voltage application, while the maximum permittivity differences are calculated from the permittivity maximum and

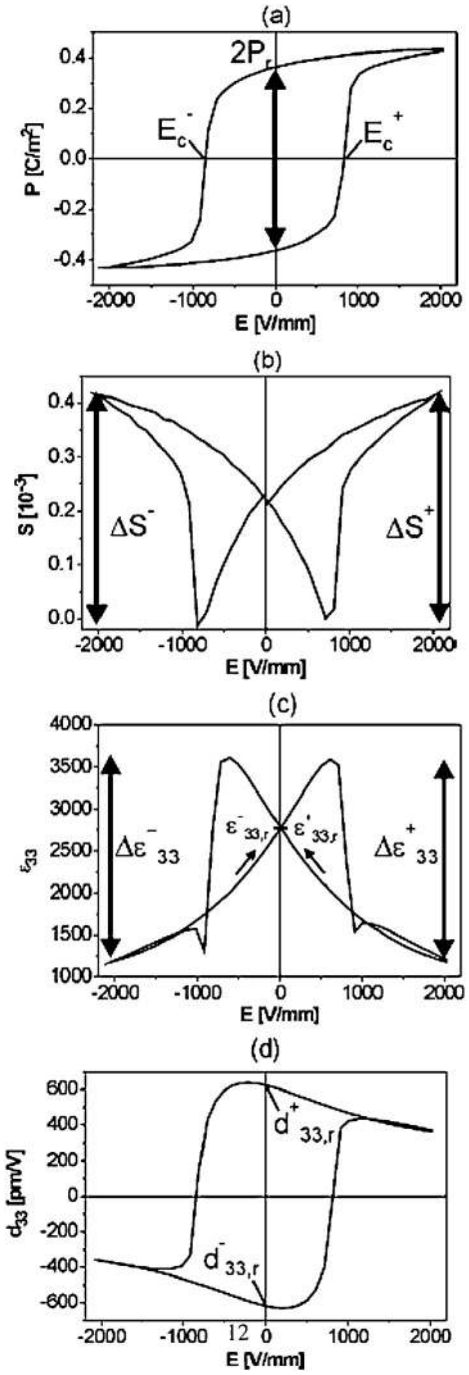

Fig. 6. Hysteresis loops of (a) polarization P, (b) strain S, (c) permittivity ε_{33} and (d) piezoelectric coefficient d_{33} for the PZT ceramic $Pb_{0.99}[Zr_{0.45}Ti_{0.47}(Ni_{0.33}Sb_{0.67})_{0.08}]O_3$ (PIC 151 from PI Ceramics, Germany) (Balke et al. [80]).

the value at maximum electric field under the same polarity. Similar to the strain asymmetry an asymmetry factor can be calculated for the permittivity: $\gamma_\varepsilon = (\Delta\varepsilon^+_{33} - \Delta\varepsilon^-_{33})/(\Delta\varepsilon^+_{33} + \Delta\varepsilon^-_{33})$

- remnant piezoelectric coefficient $d^{+/-}_{33,r}$ and polarization offset π:

As d_{33} is an absolute parameter a shift of the hysteresis loop along the ordinate indicates the existence of a polarization offset π. It can be expressed through the remnant values of polarization, piezoelectric coefficient as well as permittivity under the assumption that the dependence of the latter two on the small excitation field is linear: $\pi = P_r((d^+_{33,r}/\varepsilon^+_{33,r} - d^-_{33,r}/\varepsilon^-_{33,r})/(d^+_{33,r}/\varepsilon^+_{33,r} + d^-_{33,r}/\varepsilon^-_{33,r}))$ [84]

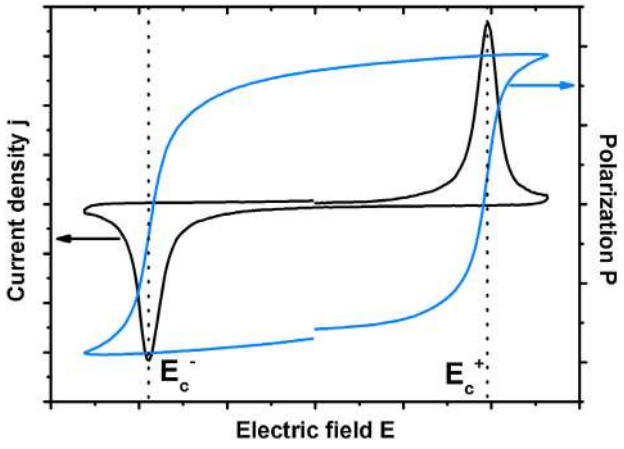

Fig. 7. Polarization and corresponding current density hysteresis loop.

2.2. Unipolar, bipolar, sesquipolar and DC conditions

For ferroelectric ceramics used in commercial devices the applied electric signal is determined by the specific application. Actuators are driven in unipolar or sesquipolar mode to avoid the occurrence of mechanical stresses due to domain reorientation while maximizing the strain output. However, the switching between two remnant polarization states due to domain reorientation is the essential feature for data storage applications which are thus driven in bipolar mode.

Fatigue of lead-based ferroelectric ceramics due to *unipolar electric loading* leads to slight degradation of remnant and maximum polarization only (Fig. 8) [85,86].

Sinusoidal electric loading up to 10^9 cycles was found to decrease the maximum unipolar polarization by ≈10% for a commercial soft PZT, the maximum unipolar strain [85] and the piezoelectric coefficient d_{31} degrade even less [87]. For non-commercial lead-free ceramics of the composition $0.94[Bi_{1/2}Na_{1/2}]TiO_3 - 0.06BaTiO_3$ about 35% of the switchable polarization is lost after 10^4 cycles already [88,89]. In both lead-based and lead-free materials the cycling procedure introduces asymmetries in both large and small signal hysteresis loops (Figs. 8 and 9). These are most noticeable for the strain and permittivity loop. For the former the cycling procedure leads to a larger maximum strain under electric fields with the same polarity as the cycling field compared to a smaller value if the polarity is opposite. The latter shows a larger value of the permittivity peak if the polarity of measurement and cycling field are the same and a smaller peak if they are opposite. This development is captured in the asymmetry factors γ_S and γ_ε (Fig. 10). The hysteresis loop of the piezoelectric coefficient d_{33} develops an asymmetric shape as well (Fig. 9) due to a general shift of the d_{33} loop along the positive ordinate, which appears to be more pronounced for positive d_{33} values compared to negative ones. This feature is described through the polarization offset value (Fig. 9). Besides the asymmetries all hysteresis loops appear to be shifted along the abscissa. The shift occurs anti-parallel to the cycling field polarity for all large and small signal hysteresis loops and is described as a bias field E_{bias}. Even after 10^8 cycles the degradation has not reached a state of saturation. However, the bias field develops independent of the cycling field amplitude if the latter is much larger than E_c [90]. For relaxor-type ceramics in the ergodic state such as 91BNT–6BT–3KNN a similar development of asymmetries and the build-up of an internal E_{bias} has been observed [91].

Long-term electric loading under a DC field was found to show similar degradation features upon unipolar loading [80]. A strong dependence of the fatigue effect on the field amplitude was

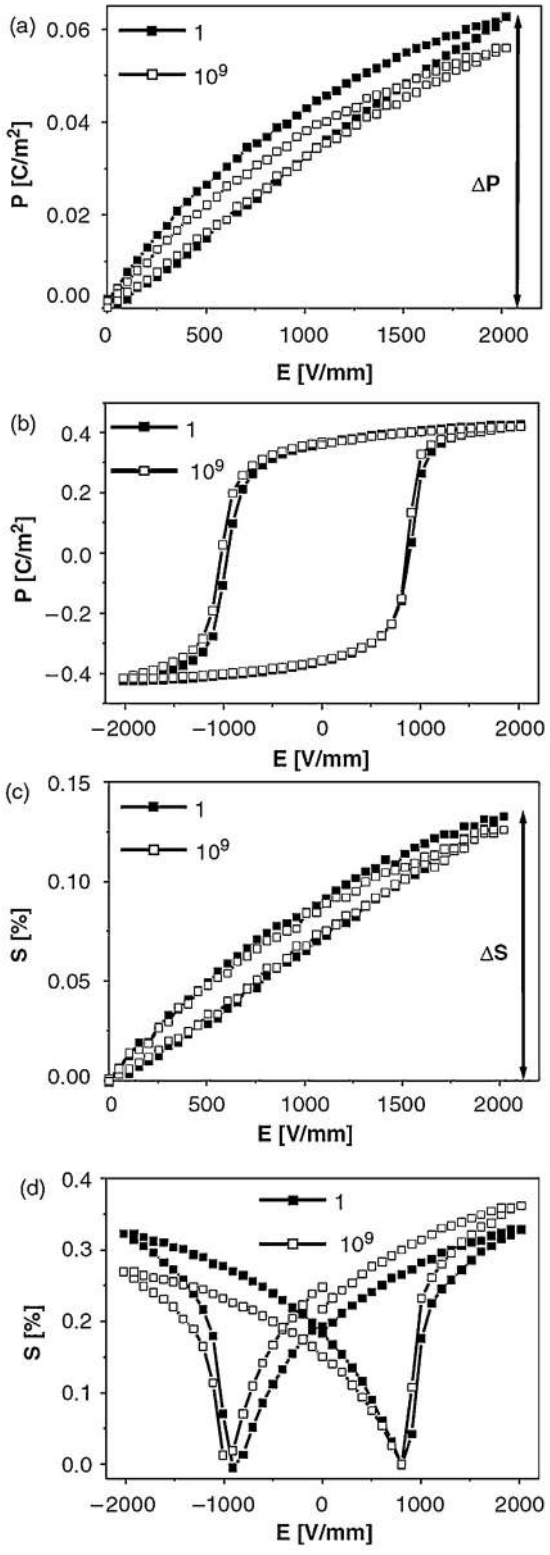

Fig. 8. Unipolar and bipolar hysteresis loops $P(E)$ and $S(E)$ after one and 10^9 unipolar electric cycles in commercial PZT ceramic PIC 151 (Balke et al. [85]).

observed. For DC amplitudes close to the coercive field the progress of fatigue degradation varies significantly. However, for electric fields higher than $2E_c$ the development of the material parameters becomes independent of the specific amplitude applied [80].

In contrast to unipolar and DC loading the degradation of remnant large and small signal values is severe if the applied

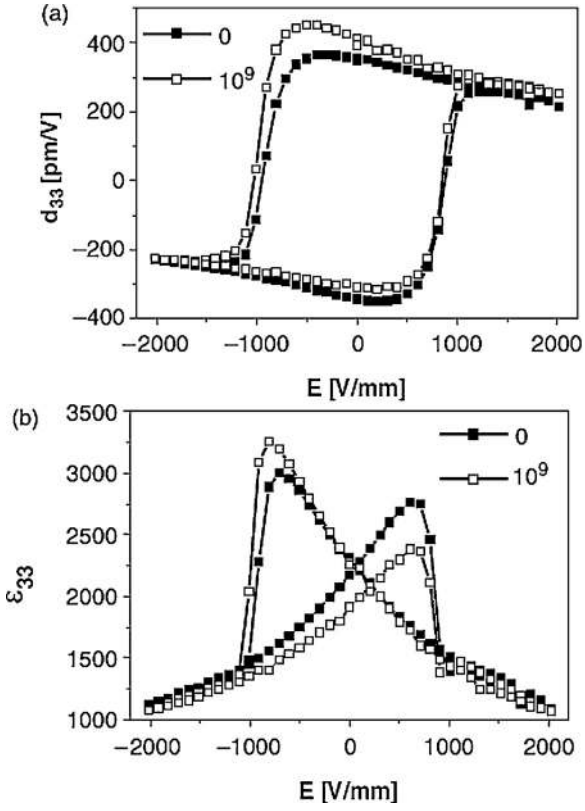

Fig. 9. Bipolar loops of piezoelectric coefficient d_{33} (a) and permittivity ε_{33} (b) in PZT ceramic (PIC 151) after one and 10^9 unipolar electric cycles (Balke et al. [85]).

electric signal is bipolar [83,87,88,92,93]. The dielectric and piezoelectric hysteresis loops in PZT (PIC 151) show strong degradation of maximum and remnant values and the switching kinetics under a DC poling field slows down with increasing fatigue level [94–96] (Fig. 11). In Fig. 12 the hysteresis loops of $0.94[Bi_{1/2}Na_{1/2}]TiO_3 - 0.06BaTiO_3$ keep their symmetric shape even in the strongly fatigued state. This behavior was observed as well for commercial soft PZT samples [97], whereas studies on La-doped PZT showed the appearance of a strong asymmetry most pronounced for the piezoelectric parameters [93]. An increasing cycling field amplitude above the coercive field leads to stronger degradation of both dielectric and piezoelectric parameters [87]. In contrast to that, only minor fatigue degradation upon bipolar

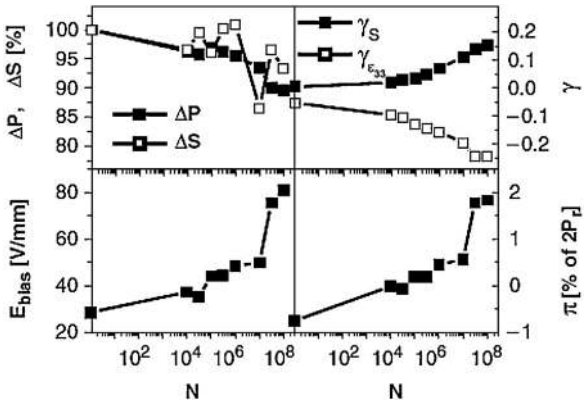

Fig. 10. Fatigue parameters extracted from the large and small signal hysteresis loops in PZT ceramic (PIC 151) plotted vs. number of unipolar electric cycles (Balke et al. [85]).

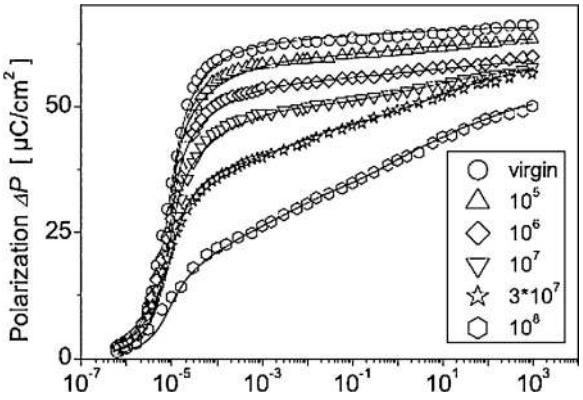

Fig. 11. Switchable polarization of a PZT sample (PIC 151) vs. poling time for different fatigue stages (Zhukov et al. [95]).

cycling was reported for PLZT [98] as well as BNT-based ceramics if they appear to be ergodic relaxors [91,99,100].

Sesquipolar loading is very attractive for actuator applications as it increases the strain output significantly while the electric losses are kept low. An early study on the strain degradation of different lead-based stack actuators under combined mechanical preload and sesquipolar electric loading showed that for most actuators the strain output is stable up to about 3×10^7 cycles [101].

A systematic study on soft PZT bulk ceramics revealed that electric cycling with a sesquipolar signal induces fatigue characteristics similar to unipolar loading conditions as long as the maximum reverse field is smaller than the coercive field [85]. The fatigue parameters characteristic for unipolar fatigue, such as E_{bias} and the asymmetry factors appear less pronounced under sesquipolar cycling and the loss in S is less than 15% for reverse fields up to E_c and 3×10^7 cycles. In contrast to that, the maximum polarization difference decreases by up to 56% under the same cycling conditions.

2.3. Influence of temperature

The dielectric and piezoelectric parameters of ferroelectric and relaxor-type ceramics are strongly dependent on temperature. Two competing mechanisms determine the specific development of the material parameters: (1) the spontaneous polarization decreases with increasing temperature such that less change in polarization and strain per switched unit cell is gained and (2) the domain wall mobility increases with increasing temperature as the lattice distortion decreases such that better alignment under electric field application can be achieved. The impact of this competition becomes visible e.g. in the strain hysteresis loop. Here the unipolar strain increases with increasing temperature while the total switchable strain S decreases [102]. For relaxor-type materials the proximity to the transition temperature between ergodic and non-ergodic state is another critical factor as it determines the stability of the ferroelectric long-range order induced during electric cycling. Just as the general material parameters the fatigue characteristics depend on the temperature as well.

Fatigue degradation of soft PZT ceramics under a bipolar signal appears to be more severe at lower temperatures [87]. While 10^6 bipolar cycles at $-20\,^\circ$C lead to a reduction of the polarization by 60%, the same cyclic loading scenario performed at $100\,^\circ$C reduces the polarization by less than 10% (the Curie temperature is $T_c = 190\,^\circ$C). For conventionally sintered relaxor PLZT ceramics a similar trend was found [103]. With increasing temperature the fatigue degradation becomes less severe and vanishes completely for temperatures larger than the temperature of the permittivity maximum T_m. However, hot-pressed ceramics exhibit stronger

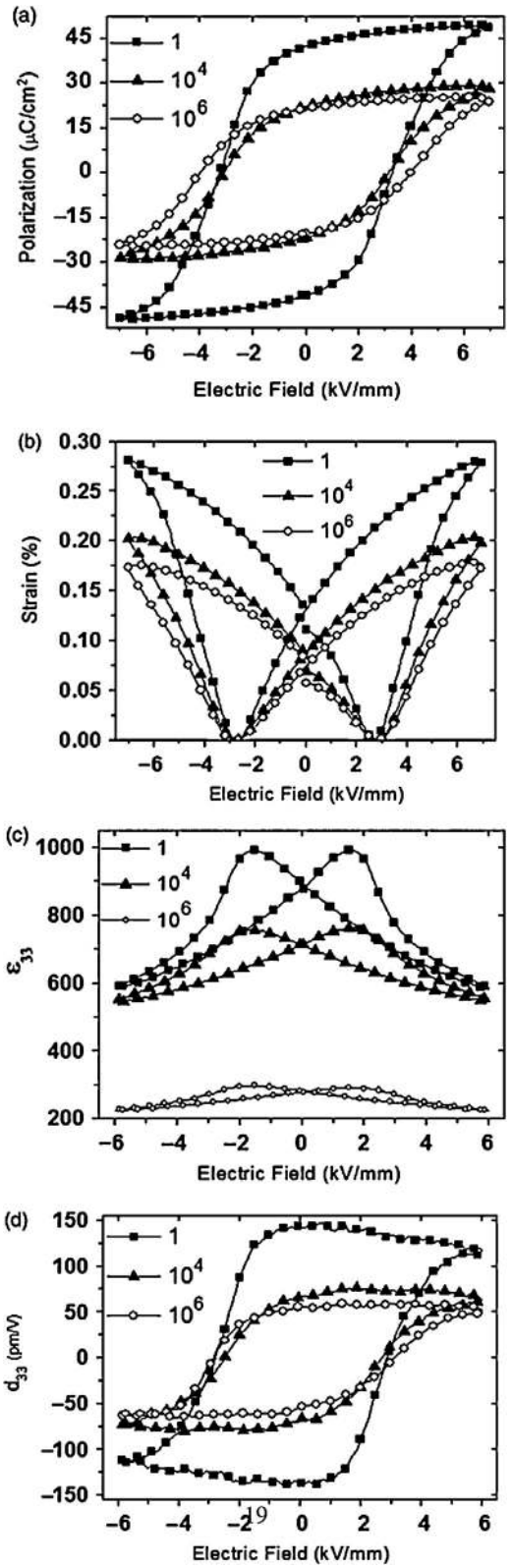

Fig. 12. Virgin and fatigued hysteresis loops of BNT–6BT (Luo et al. [88]).

polarization degradation with increasing temperature below T_m, while the fatigue free behavior above T_m is maintained.

Degradation of soft PZT due to unipolar electric loading exhibits a more complex pattern [90]. While degradation of remnant and maximum polarization is still negligible at higher temperatures, the bias field develops at different rates. Close to room temperature

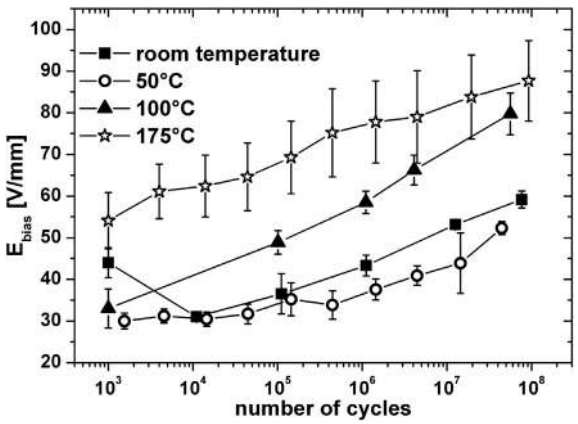

Fig. 13. Development of bias field E_{bias} of soft PZT (PIC 151) due the application of an unipolar electric field at different temperatures (Glaum et al. [90]).

and for temperatures as high as 175 °C the rate of E_{bias} increase is similar, whereas it was found to be higher for intermediate temperatures (Fig. 13). This indicates that E_{bias} might develop higher values for cycling at intermediate temperatures.

2.4. Cycling with electromechanical loading

The application of a small mechanical uniaxial preload to a piezoelectric material has been found to increase the unipolar strain per applied electric field unit. This knowledge is nowadays used for the optimization of the driving conditions for multi-layer actuators [104].

Several fatigue studies covering a variety of different electromechanical loading scenarios can be found in the literature. The combination of a fixed mechanical preload with a bipolar electric signal leads to better fatigue resistivity of the polarization with increasing preload for soft PZT disk specimen (Fig. 14) [105].

Chaplya et al. [101] investigated the fatigue behavior of different stack actuators under a sesquipolar electric field. The applied mechanical preload during cycling was chosen to optimize the strain output in the unfatigued state. All actuators showed stronger fatigue of the strain output if the mechanical preload was applied. However, the differences varied for different actuator types. For $Pb[Ni_{1/3}Nb_{2/3}Zr,Ti]O_3$ multi-layer actuators the application of a unipolar electric field combined with a low and a high fixed mechanical preload leads to less degradation of the unipolar strain if lower preload is applied. However, the unipolar polarization was found to decrease more under low preload [106]. In summary, the application of a fixed mechanical preload seems to reduce the fatigue degradation of the strain whereas it increases the

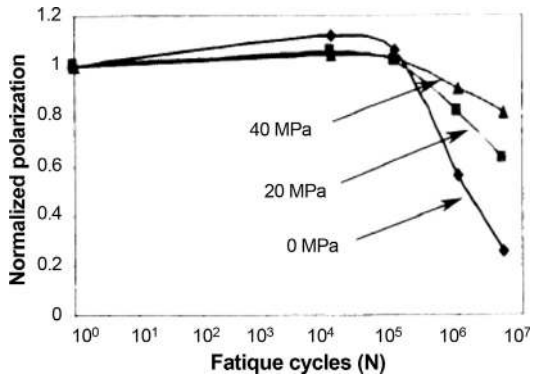

Fig. 14. Bipolar fatigue characteristics of PZT-5H ceramics depending on mechanical preload (Wang et al. [105]).

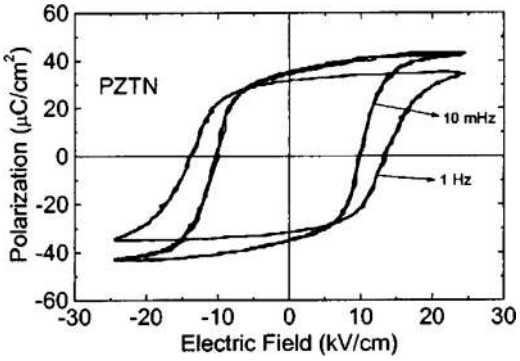

Fig. 15. Frequency dependent polarization hysteresis loops in soft PZTN ($Pb[Zr_{0.53}Ti_{0.47}]O_3$ doped with 1% Nb) (Lente et al. [110]).

polarization degradation independent of the applied electric signal type. However, if the uniaxial mechanical load is not fixed but applied as cyclic waveform as well, the degradation becomes stronger even compared to fatigue induced by an electric load alone. This was shown by Lupascu et al. [107] for unipolar electric loading combined with cyclic mechanical loading, where both signals were offset by 90° to each other. Applying a constant or cyclic mechanical load in a 4-point bending instead of a uniaxial rig, leads to a significant decrease of sample lifetime with increasing mechanical amplitude [108,109]. Additionally, it depends on the type of electric signal applied. The longest lifetimes are observed if no electric field is applied, which then get reduced if the applied electric signal changes from unipolar to sesquipolar to bipolar [109].

2.5. Frequency and cycle number

Domain switching is often described as a visco-elastic process and as such is dependent on loading frequency [110]. Increasing frequency leads to an increase of the coercive field (Fig. 15) as well as the dielectric losses and can induce self-heating of the sample. Both the change in switching field and the effect of self-heating have to be taken into account when studying the frequency dependence of electric fatigue. For bipolar electric cycling of ferroelectric PLZT as well as soft PZT ceramics it is reported that increasing frequency leads to less fatigue degradation in the range from 10 to 100 Hz [111,112]. In the case of PLZT the behavior even appears to be fatigue-free for frequencies in the kHz regime [111]. Additionally, it was found that increasing frequency reduces the rate of crack growth (Fig. 16) [112]. A study on the frequency dependence of unipolar and DC fatigue degradation in soft PZT revealed that most parameters degrade in a similar fashion if they are plotted against the integrated field instead of the cycle number (Fig. 17). Significant deviations were found only for the polarization offset as well as the maximum and remnant values of the permittivity ε_{33} [93].

2.6. Electrodes

The electrode-ceramic interface determines the electric field distribution throughout the sample. Besides the surface roughness, the electrode material and interface quality are important factors, especially in thin film devices. In this case, domain nucleation is mainly initiated at the sample surface [113]. Inhibition of the nucleation process would lead to degradation of the dielectric properties [114,115]. However, even for bulk ceramics the electrode–ceramic interface can strongly influence the dielectric properties.

A comparison of the dielectric and piezoelectric properties of soft PZT ceramics sputtered with either silver or platinum was

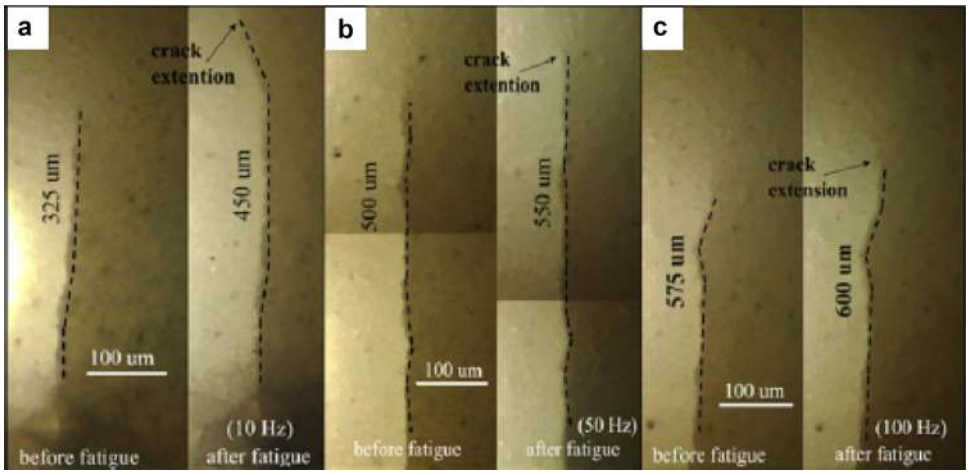

Fig. 16. Frequency dependence of the crack extension under bipolar electric loading for soft PZT (Pojprapai et al. [112]).

carried out to investigate the effect of electrode materials with different work functions. The work function of the electrode material can determine if charge injection during electric field application can take place and what kind of charge carriers are favored in this process. It was shown that platinum sputtering leads to slightly higher values of polarization, strain and permittivity in the fresh state. However, upon bipolar electric cycling the platinum sputtered samples fatigued much faster as compared to the Ag sputtered ones [97]. In contrast to that, no difference in properties or bipolar fatigue behavior was found for the same kind of soft PZT ceramic coated with Pt, RuO_2 or tin-doped In_2O_3, even though the differences in work function are significantly larger compared to the former study [116].

2.7. Sample geometry – actuators

Piezoelectric materials are nowadays used in a wide range of actuation applications such as miniature motors and high-precision positioning devices. Manufacturing of the materials in a multi-layer design allows the achievement of high strokes at low electric fields. Different electrode designs such as "ideal electrodes", "tab electrodes" or "interdigital electrodes" can be found [117,118] (Fig. 18), each afflicted with their specific challenges in processing.

The component design of active and non-active materials and especially the electrode configuration determines the boundary conditions for the piezoelectric response. Non-homogeneous electric field and stress distributions are present in tab-electrode and interdigitally designed actuators [117,119] distinguishing their characteristics from a bulk sample in a plane configuration of the parallel plate capacitor.

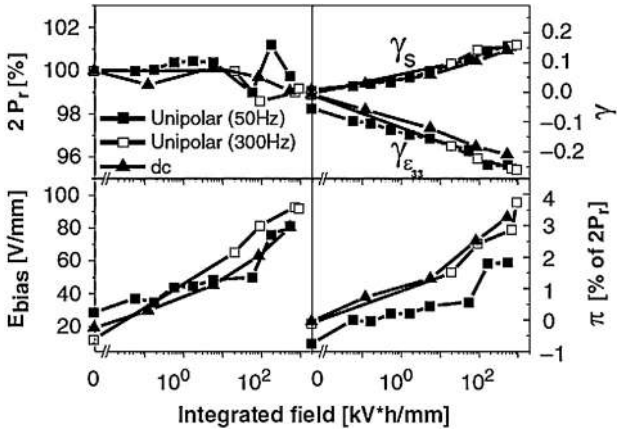

Fig. 17. Characteristic fatigue parameters of unipolar fatigued soft PZT cycled at different frequencies vs. integrated electric field (Balke et al. [93]).

Electric cycling leads to a reduction of the strain output with cycle number in most lead-based actuators. The detailed degradation characteristics depend on the type of actuator, the electric loading signal type and amplitude as well as mechanical preload and humidity. Specifically, bipolar loading of an interdigital-electroded actuator leads to very fast degradation within the first 10^4 cycles [119], whereas actuators are reported to withstand unipolar cycling up to 8×10^5 in interdigital configuration [118,120] and even 10^9 cycles in the plain electrode configuration [106]. Increase of the unipolar electric field amplitude leads to faster fatigue degradation [118,120] as does higher humidity [118] and mechanical preload [101,106,118]. Wang et al. reported a change in fatigue pattern for their commercial PZT actuator with normal electrode configuration if cycled higher than 0.85×10^8 cycles, changing from monotonic degradation to a more fluctuating pattern. The application of a cyclic field to a stack actuator usually leads to mechanical deterioration which is independent of the type of waveform used [118–120]. Strong mechanical deterioration was found as well for bending actuators under bipolar electric and constant mechanical loading [121]. However, PZT stack actuators with Ag/Pd electrodes loaded with a DC electric field show different characteristics [122,123]. No mechanical deterioration is observed. Instead, a strong increase in conductivity over time determines the device degradation. The conductivity rises faster over time with increasing electric field amplitude [123] and the probability of failure was found to increase rapidly with increasing Ag content of the electrodes [122]. Surface precipitates of silver, discoloration of single PZT layers and a strong enrichment of silver along the grain boundaries are observed in degraded PZT stacks. Precipitates are initiated at the anode and develop toward the cathode under DC field application leading to Ag depletion of the anode and strong redistribution of lead in the area of damage (Fig. 19) [124].

A comparison of the properties and degradation characteristics of lead-free materials in bulk and multi-layer actuator (MLA) geometry was presented by Sapper et al. [125]. They studied the unipolar fatigue characteristic of the non-ergodic relaxor $0.92(Bi_{1/2}Na_{1/2})TiO_3 - 0.08BaTiO_3$ (BNT–8BT) and the ergodic relaxor composition $0.91(Bi_{1/2}Na_{1/2})TiO_3 - 0.06BaTiO_3 - 0.03(K_{0.5}Na_{0.5})NbO_3$ (BNT–6BT–3KNN). For both compositions they reported lower unipolar polarization and strain values for the MLA configuration compared to the bulk properties. Unipolar electric cycling leads to an increase of actuator surface temperature by

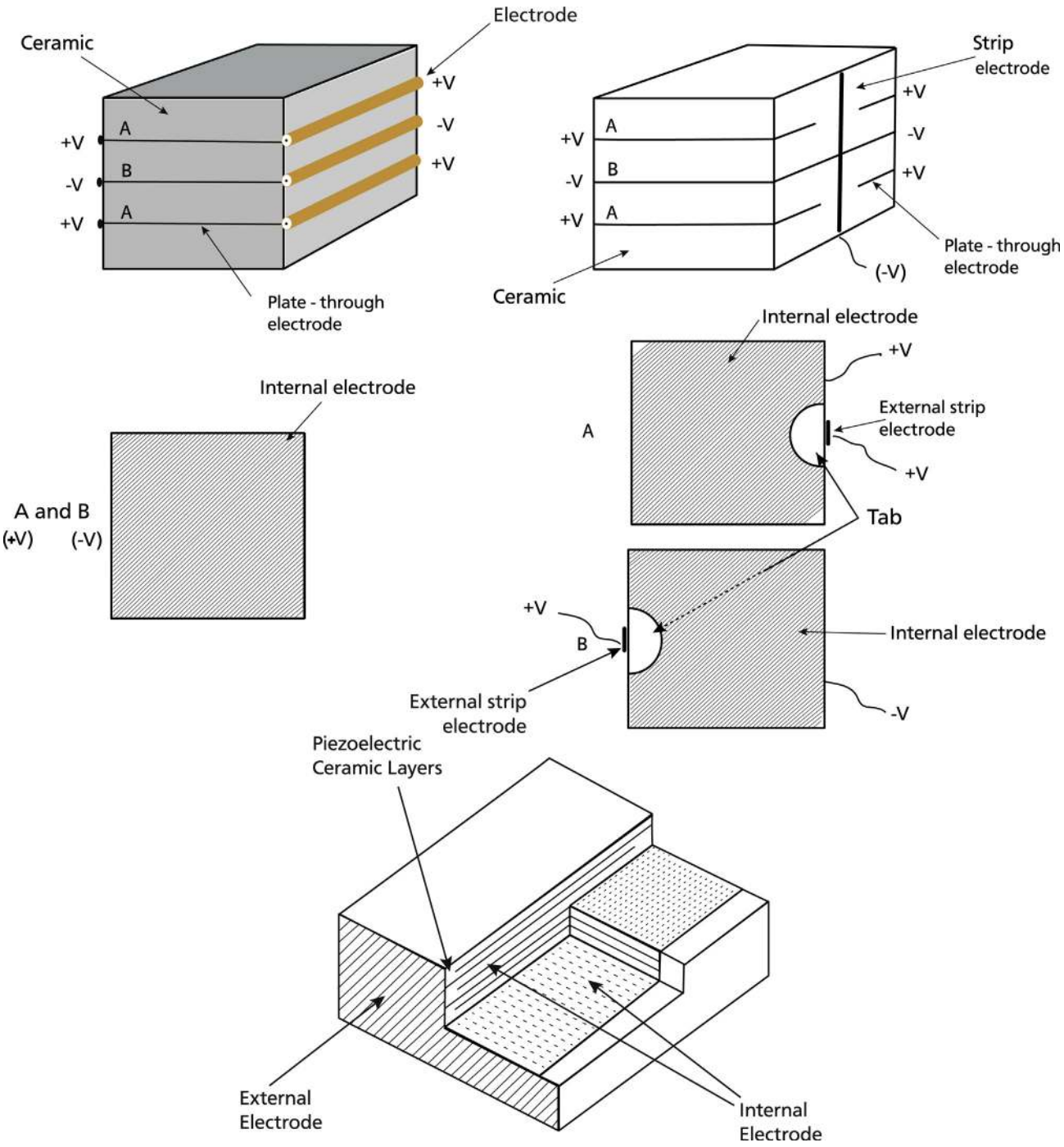

Fig. 18. Electrode geometries of multi-layer stack actuators (top) (Winzer et al. [117]). Interdigital electrode configuration of multi-layer stack actuators (bottom) (Thongrueng et al. [118]).

about 2 °C for the non-ergodic BNT–8BT, whereas a temperature change of $\Delta T = 13$ °C was found for the ergodic BNT–6BT–3KNN. No degradation of the unipolar strain of BNT–8BT up to 10^8 cycles was found for both MLA and bulk configuration. In contrast to that, unipolar cycling of BNT–6BT–3KNN leads to strong degradation of the unipolar strain in the MLA case from 10^4 cycles onwards, whereas the bulk material does not degrade significantly up to 10^7 cycles. The fatigue characteristics were identified to be caused by the appearance of electric breakdown between the ceramic and electrode material instead of the occurrence of cracks as commonly observed in PZT actuator. Therefore, adaptation of the processing conditions and electrode material is likely to improve the overall fatigue properties of these lead-free MLAs.

2.8. Experimental verification of fatigue models

The origins of fatigue can be separated in two main groups:

- Occurrence of microstructural changes such as crack initiation or element migration and
- Alteration of domain wall motion due to defect dipoles and charge carrier agglomeration.

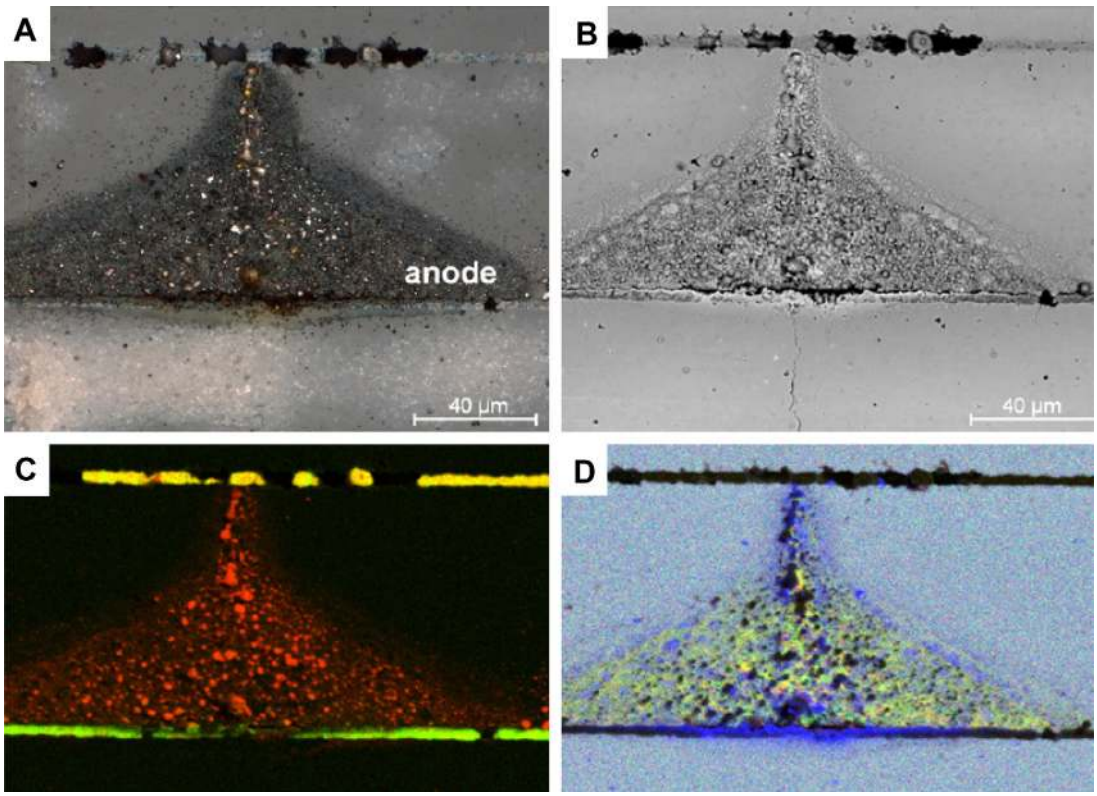

Fig. 19. Precipitation region formed under DC loading in PZT-based multi-layer actuator ($Pb[Zr_{0.52}Ti_{0.48}]O_3$ doped with 1.5% Nd): (A) light microscope image, (B) back-scattered electron micrograph, (C) elemental map from energy dispersive X-ray spectroscopy (EDX) (Ag: red, Pd: green): the precipitation area consists mostly of Ag, whereas the Ag/Pd anode is strongly depleted of Ag, (D) EDX elemental map (Pb: blue, Zr: green, Ti: red) showing that lead is redistributed in the precipitation region and accumulates close to the anode (Andreijs et al. [124]).

While microstructural changes are often easily observed on micrographs, charge carrier agglomeration either on grain boundaries or on domain walls is more difficult to prove. Additionally, both mechanisms are often active simultaneously and their contributions to the parameters difficult to separate. The following section summarizes experimental techniques used to validate the contribution of the above mentioned mechanisms to the fatigue characteristics observed.

2.8.1. Boundary effects

Microstructural changes induced by the fatigue process are often visible under the microscope or SEM or can even be seen by the naked eye. This includes the precipitation of the electrode material (Fig. 19) [123] as well as the development of cracks [81,126,127] and discoloration of the ceramic [81,123] (Fig. 20). Crack development is commonly explained by intensification and subsequent relief of mechanical stresses due to the domain switching process [112,127] and as such mostly observed after bipolar electric cycling. Regions of stress intensification can be pores or pre-existing microcracks or the interface between piezoelectrically active and inactive regions (Fig. 21) [93,119,126,128]. Discolouration and precipitation of electrode material is mostly found in multi-layer actuators with co-fired Ag-containing electrodes leading to resistance degradation and electrical breakdown of the material [123]. To determine which parts of the ceramic are affected by the microstructural changes a common approach is to subsequently remove material from the surface and re-measure the electric or piezoelectric properties after each grinding step. For PZT-based bulk ceramics with air-dried or low-temperature fired electrodes it was found that most of the mechanical degradation after bipolar fatigue is located at the ceramic-electrode interface up to a depth of about 150 μm. If the damaged area is removed the piezoelectric properties are restored to about 90% of the unfatigued values [93,129]. However, if the electrodes were fired at high temperatures above 700°C less recovery of the polarization is obtained by the grinding process and the switching dynamics still appear highly suppressed even after removal of 130 μm of the ceramic surface [81]. This indicates that high temperatures favor the migration of electrode material (in this case Ag) into the bulk ceramics similar to what has been reported for multilayer actuators [118,122,123]. Silver migration reduces the overall resistivity, which can be restored by grinding of the surface perpendicular to the inner electrodes (Fig. 22) [130]. This shows that the outer layers of the PZT stack degrade whereas the inner layers stay intact.

2.8.2. Cycling at large fields and high temperatures

If microstructural degradation can be ruled out as a cause of the observed fatigue effects the interaction of domain walls with free charge carriers in the material moves into focus (see Section 5 for detailed explanation). A common way to test if charge agglomerates are responsible for the parameter degradation is to thermally anneal the fatigued sample and measure the piezoelectric response after annealing. Bipolar fatigued PZT-based ceramics show strong re-juvenation of polarization and strain after bipolar fatigue, if the annealing temperature is higher than the Curie point [72,131,132]. Thermal annealing after unipolar electric cycling, in contrast, leads to recovery of the strain asymmetry γ_S and the switchable polarization $2P_r$ already at temperatures much lower than the Curie point [133]. This supports the hypothesis that bipolar cycling leads to stable pinning of domain walls which can only be removed when the domain structure vanishes above the Curie point. However, unipolar fatigue is governed by agglomeration of charges at grain

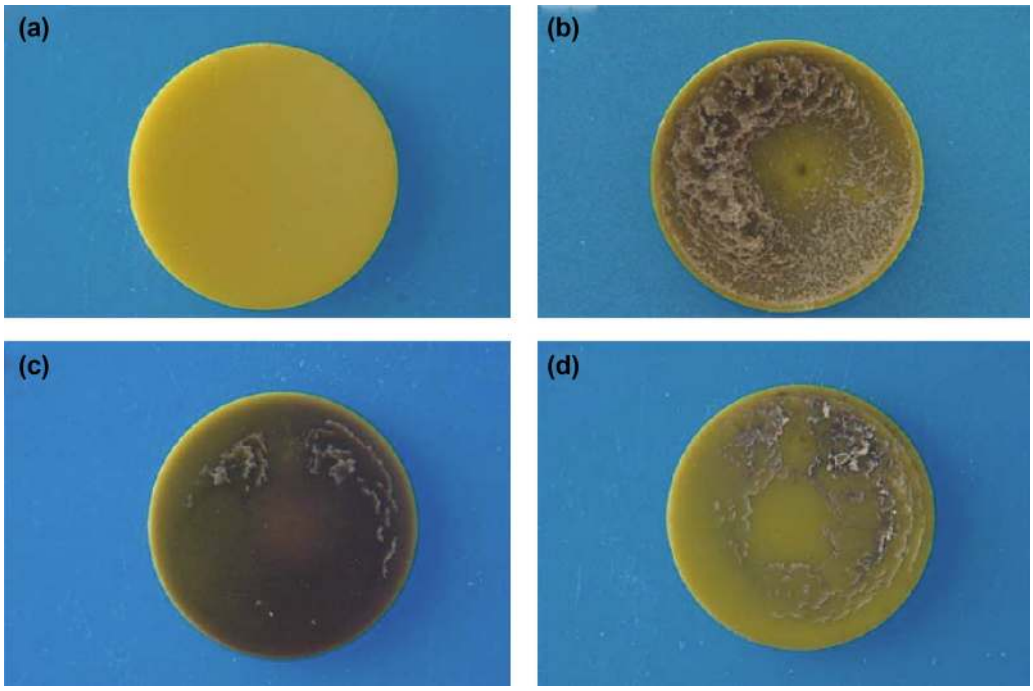

Fig. 20. Photographs of the surface of soft PZT samples (a) in the virgin state, (b) after 1.3×10^7 bipolar cycles showing high crack density in the electroded region but no cracks on the non-electroded rim, (c) and (d) both after 2.2×10^7 bipolar cycles showing strong discolouration and formation of cracks, respectively (Zhang et al. [81]).

boundaries. Their re-distribution is not coupled to the existence of a domain structure and can as such occur at lower temperatures already.

Another option to reduce the charge agglomeration is to subject the fatigued sample to bipolar electric loading [86,93,131]. For bipolar fatigued samples the application of a bipolar signal with an amplitude much higher than the cycling amplitude will lead to significant recovery of both polarization and strain hysteresis loops [81,131]. On the contrary, rejuvenation of unipolar and DC fatigued samples can be achieved by a bipolar electric signal of the same field amplitude as used for cycling [86,93]. In this case already one bipolar cycle reduces E_{bias} by about 80%. Continuous recovery of the asymmetry parameters and the offset polarization is observed as well even though none of the parameters fully rejuvenates even after 50 bipolar cycles (Fig. 23) [93]. This reflects the different stabilities of the charge agglomerates induced by cycling. While unipolar cycling induces weak agglomerates which can be easily redistributed by polarization re-orientation, the pinning of domain walls is much stronger and high electric fields are needed to free the domain walls from this constraint.

2.8.3. Results from piezo force microscopy (PFM)

Piezo force microscopy (PFM) is the perfect tool to investigate the impact of electric fatigue on domain walls on a local scale. Bipolar electric cycling of soft PZT leads to a change in domain structure from mostly 180° domains to a fine pattern of ferroelastic, "wavy" domains [134,135], which occur preferably close to the electrode interface. The "wavy" domain patterns in the fatigued state result from a deviation from the expected orientation given by the crystal structure. Similar patterns can be observed around defects in the ceramic. It can therefore be expected that interaction of domain walls with microdefects are the origin of the "wavy" structure. Annealing of the samples at 700 °C leads to reduction of the ferroelastic domains (Fig. 24), which is in accordance with the partial recovery of the macroscopic parameters. The domain alignment in poling direction decreases with increasing cycle number [97] reflecting the general reduction of the polarization due to fatigue. This reduction of polarization associated with less aligned domains after bipolar cycling was found for lead-free $Li_{0.06}(Na_{1/2}K_{1/2})_{0.94}NbO_3$ ceramics as well [136]. However, in contrast to the results above the authors observed a

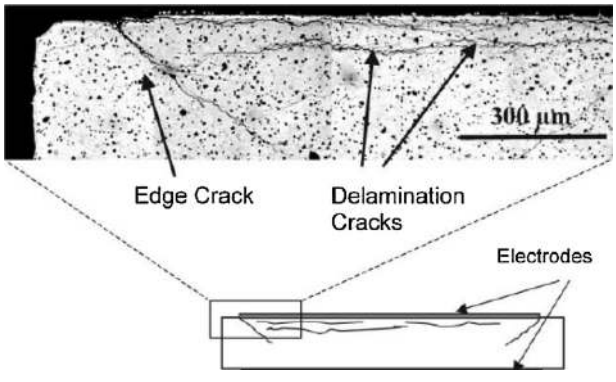

Fig. 21. Optical image and schematic showing the crack pattern below the electrode of a soft PZT after bipolar electric cycling (Nuffer et al. [126]).

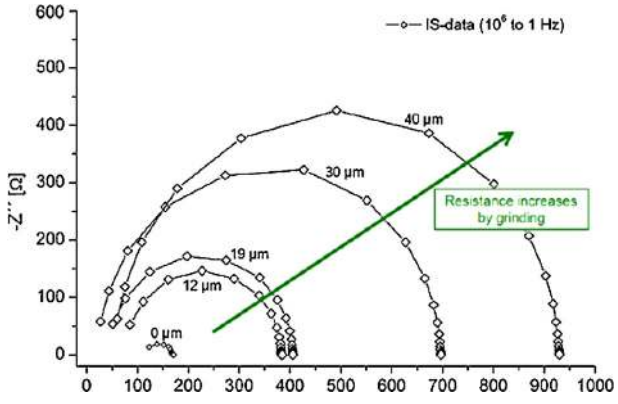

Fig. 22. Impedance spectra of a highly degraded PZT film showing the increase in resistivity after different grinding steps (Andreijs et al. [130]).

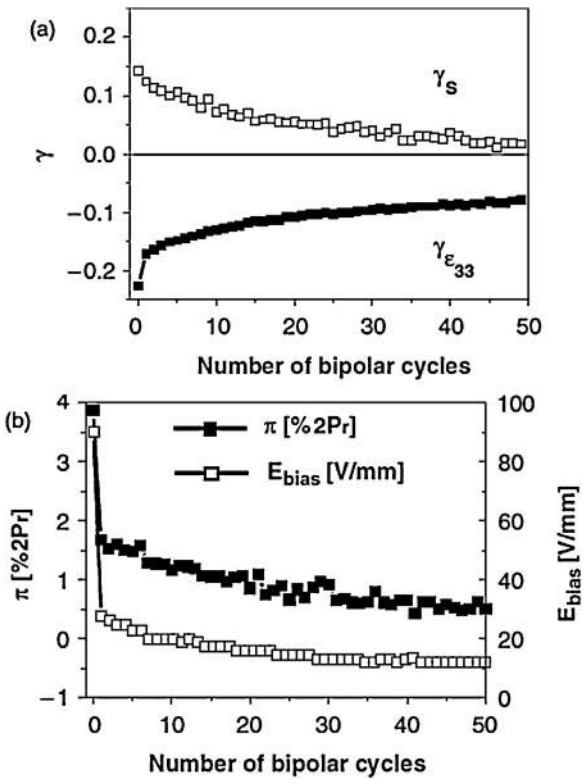

Fig. 23. Rejuvenation of the unipolar fatigued asymmetry factors, offset polarization and bias field in soft PZT (PIC 151) upon application of a bipolar electric field (Balke et al. [93]).

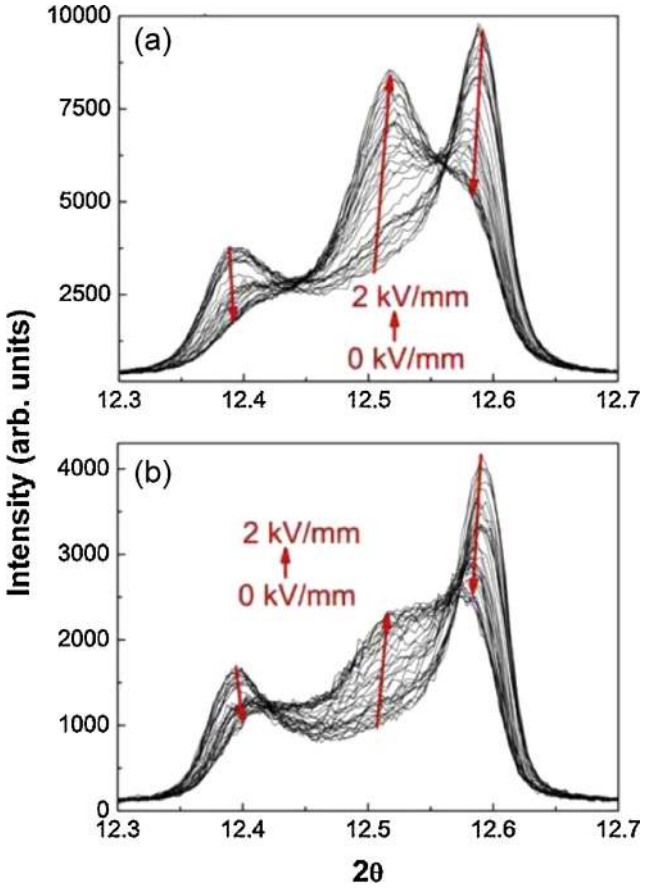

Fig. 25. Analysis of the switching behavior for a commercial PZT (PIC 151) using high resolution synchrotron radiation. (a) Unfatigued pre-cycled samples and (b) bipolar fatigued sample after 10^7 cycles (Hinterstein et al. [138]).

reduction of the fraction of 90° domains and an increase in size of the 180° domains with increasing cycle number. It remains unclear why the domain structure of these two materials develops in such a different way.

2.8.4. Results from in-situ X-ray diffraction analysis (XRD)

Structural experiments based on in-situ high resolution diffraction data, that had been taken in transmission with a sample orientation of $\psi = 45°$ relative to the incident beam in order to minimize texture effects, were used to study the field induced phase transformation for unfatigued and fatigued PZT. Hinterstein et al. [48] found for unfatigued PZT a pronounced electric field induced phase transition from tetragonal to monoclinic (pseudo-rhombohedral) which supports the hypothesis that the enhanced piezoelectric properties of PZT with compositions near the morphotropic phase boundary are attributed to a polarization rotation mechanism in the presence of a monoclinic phase [58]. Fig. 25 reveals the structural changes of the pseudocubic 200_c reflection, which is quantitatively representative of the relative fractions of the tetragonal and monoclinic phase. It is obvious that the tetragonal phase content decreases whereas the monoclinic one increases. Rietveld refinements of the X-ray diffraction patterns indicate a change of the monoclinic phase content of approximately 10–15% when an electric field of 2 kV/mm is applied [48].

When PZT is subjected to 10^7 bipolar cycles an alteration of the switching behavior is observed. Fig. 25b shows the corresponding changes of the X-ray pattern for electrics field between 0 and 2 kV/mm. There is a significant reduction of the relative peak intensities for the field induced tetragonal to monoclinic phase transformation compared to the unfatigued sample. Based on a

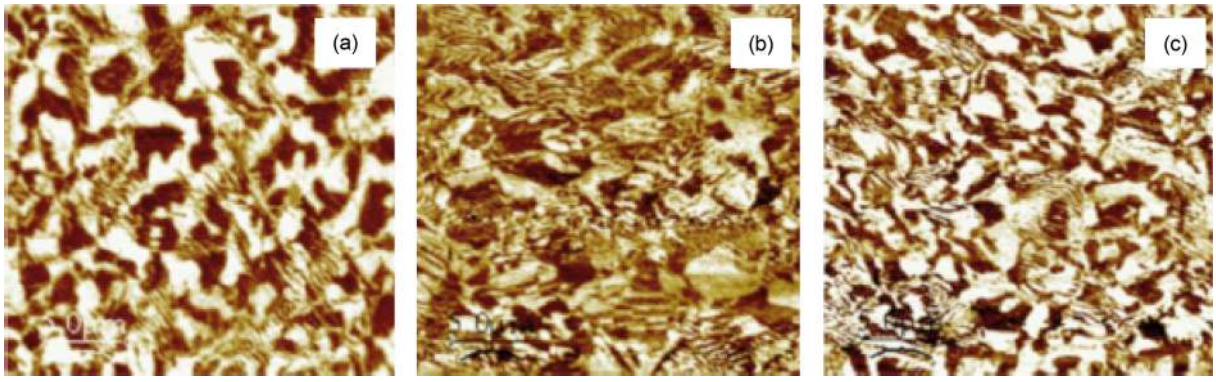

Fig. 24. Domain patterns of (a) a virgin, (b) a fatigued, and (c) an annealed at 700 °C for 10 h PZT sample (PIC 151) (Shvartsman et al. [134]).

Rietveld refinement of all spectra for unfatigued as well as fatigued samples using the same tetragonal-monoclinic two-phase model [48], Hinterstein et al. also determined a 10%-shift of the relative phase content from monoclinic to tetragonal for an unloaded material. Such a shift corresponds to a compositional modification of morphotropic PZT by approximately 0.4 mol% Zr [137]. Thus, the macroscopic strain is modified to the same extent as it is observed for bipolar fatigue depending on the Zr/Ti-ratio and the dopant concentration [7].

3. Aging and de-aging: experimental results

Ferroelectric materials are subject to degradation with time also when no external mechanical or electrical load is applied. This phenomenon is called aging and is characterized by similar parameters as fatigue. Generally, aging reveals itself through deformation of the polarization loop as well as decrease of maximum polarization, strain and permittivity. However, essential features of this process depend on the particular composition, properties of available defects and the initial polarization state of the material. The donor doped (soft) ferroelectrics exhibit much weaker aging than the acceptor doped (hard) ferroelectrics, which are in the focus of this section. The most common reason for aging considered in the literature is the rearrangement of charged defects and electronic carriers and their interaction with the polarization in the bulk and at the domain walls. Typical defects include vacancies of the constituting elements, in particular mobile oxygen vacancies, but also donor and acceptor dopants and their associates with vacancies. Migration of oxygen vacancies and, particularly, the reorientation of the polar associates of acceptors with oxygen vacancies (defect dipoles) play a prominent role in aging (see Section 4). Thus, in this section a number of representative classical and recent experimental results on aging are highlighted, which are relevant in the context of defect reordering and/or migration.

Aging of hard ferroelectrics in a poled state leads to a shift of the hysteresis *P–E* loop along the field axis opposite to the polarization direction as sketched in Fig. 26a [12] and illustrated by an example of 1% Fe-doped PZT(58/42) in Fig. 26c [139]. Aging of the same material in an unpoled state results in a pinched hysteresis *P–E* loop, shown schematically in Fig. 26b [12] and illustrated exemplarily in Fig. 26c. The strength of the loop deformation is characterized by the internal bias field defined graphically as is shown in Fig. 26. This field increases with time exhibiting a progressively frozen initial – poled or unpoled – polarization state. The domain pattern in an aged unpoled state is reproduced exactly after application and removal of an electric field exceeding the corresponding coercive field as is illustrated in the case of a Mn-doped $BaTiO_3$ single crystal (Fig. 27).

The internal bias field typically exhibits a quasilinear rise on the logarithmic time scale eventually reaching a maximum value, which increases with increasing acceptor doping and decreasing temperature as shown in Fig. 28 for the example of Ni-doped $BaTiO_3$ [73]. This maximum is reached in a shorter (aging) time when the temperature is higher.

Indications of saturation of the internal bias field in the course of aging are apparent for a Ni concentration of 1 mol% at all temperatures (Fig. 28(middle)), but at a temperature of 45 °C it is only seen for the highest doping level of 1 mol% (Fig. 28(top)). This reveals the

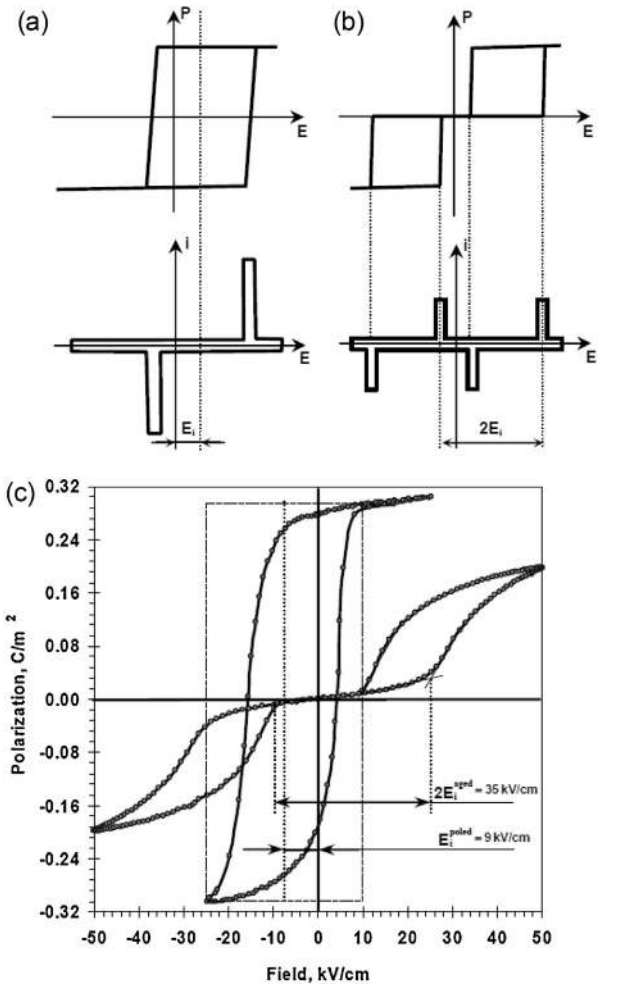

Fig. 26. Hysteresis loops and corresponding current for (a) poled aged and (b) unpoled aged ceramics; (c) the experimental hysteresis loops of hard (1.0 at.% Fe-doped) PZT (58/42) ceramics: in aged state and poled at 120 °C, 10 min, cooling down to room temperature under applied dc field [by courtesy of M. Morozov, Fig. 7.12 from [139], p. 128]. Note a definition of the internal bias field for the poled case in (c) slightly different from that in (a).

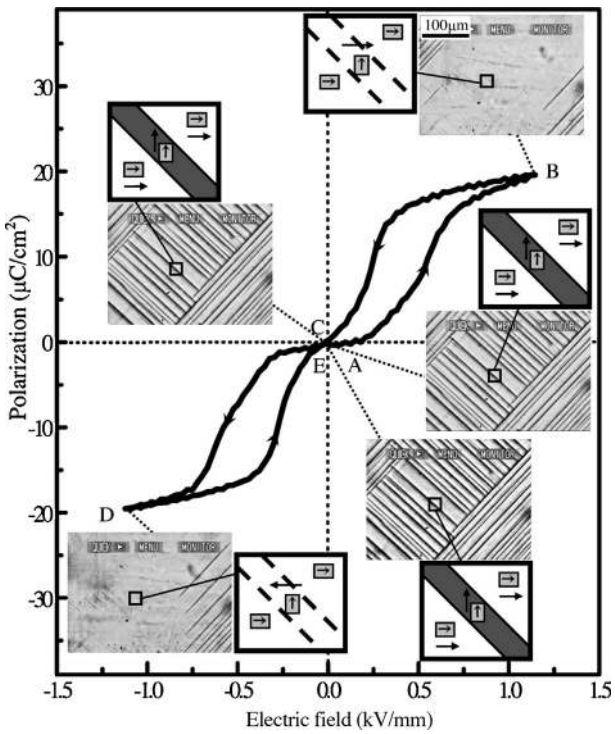

Fig. 27. Visualization of aging in a Mn-doped $BaTiO_3$ single crystal (Zhang et al. [140]).

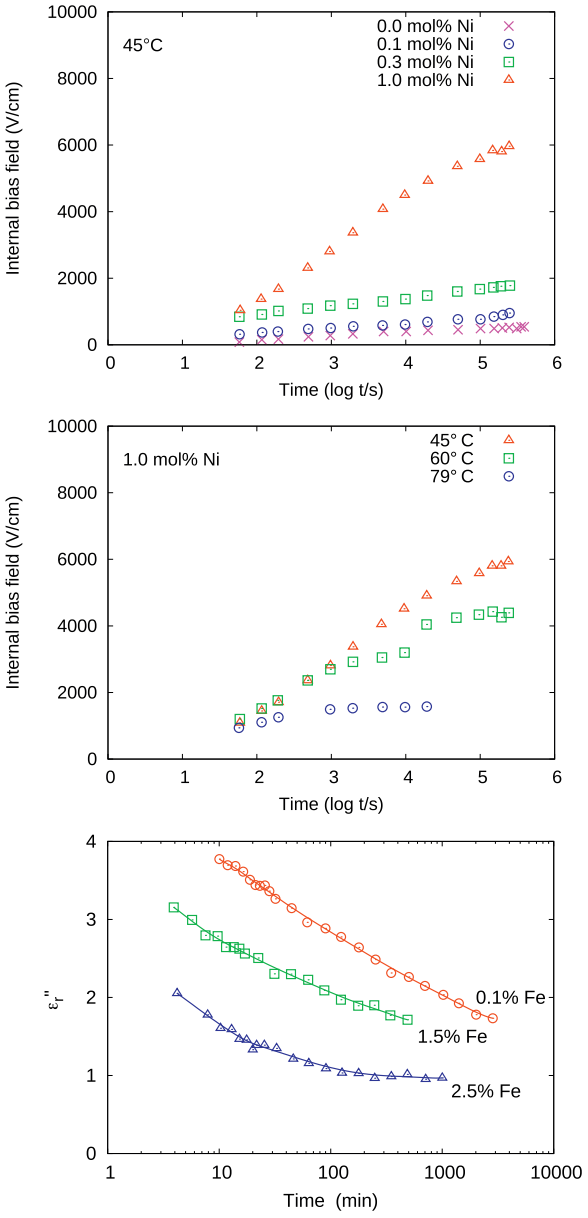

Fig. 28. Internal bias field in Ni-doped $BaTiO_3$: Time dependencies for different doping levels (top) and for different temperatures (middle) (Arlt et al. [73]). Time dependence of the imaginary part of dielectric permittivity for PZT differently doped with Fe (bottom) (Herbiet et al. [141]).

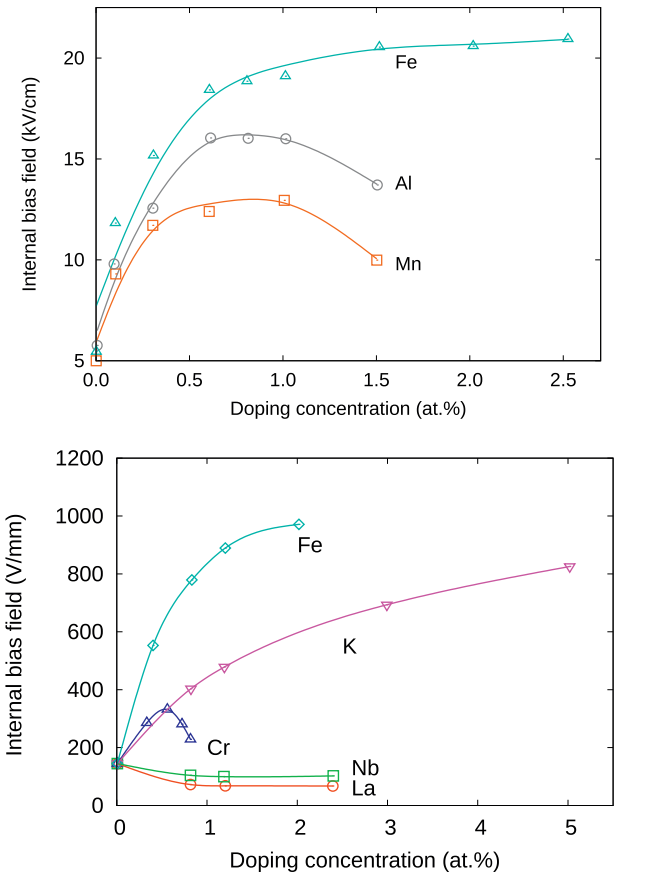

Fig. 29. Doping effects on the internal bias field emerging in PZT from Carl et al. [12] (top) and Takahashi et al. [142] (bottom).

decreasing dependence of the characteristic aging time on doping concentration. Similar indications are apparent for the concentration dependence of losses (Fig. 28(bottom)) [141]. Systematic studies of aging effects due to different acceptors [12,142] have shown that the doping dependence of the maximum internal bias field is nonlinear even at low doping levels and saturates at a few mol% (Fig. 29).

The aged state of ferroelectrics can be relaxed (de-aged) by applying a bipolar AC electric field, as shown for the case of 0.1%-doped PZT aged in the unpoled state (Fig. 30), or by heating over the ferroelectric/paraelectric transition temperature.

Note the remarkable difference between characteristic aging and de-aging times apparent from Figs. 28 and 30. The former are typically by orders of the magnitude larger than the latter. On the other hand, in the state which is usually qualified as a de-aged one [12,139] the virgin form of the hysteresis loop is, in fact, not restored completely. Thus, a pinched loop (Fig. 30) is opened after several dozens of bipolar cycles but remains slanted. Recovering to the initial rectangular shape of the virgin state like that in Fig. 6a takes much longer time [70]. De-aging times (as well as aging times) exhibit substantial dependence on the type and concentration of doping ions as seen in Fig. 31.

Restoring the permittivity in the high-temperature paraelectric state of Mn-doped $Ba_{0.80}Sr_{0.20}TiO_3$ after aging in the ferroelectric state is shown in Fig. 32. The kinetics of this evolution follows essentially the Debye relaxation function $1-\exp(-t/\tau)$, while the de-aging time τ exhibits the Arrhenius temperature dependence with an activation energy of 0.43 eV.

Aging and de-aging processes are inherently related to the electric conductivity of ferroelectric materials. Donor doped (soft) ferroelectrics exhibit low conductivity and almost no aging while acceptor doped (hard) ferroelectrics possess medium conductivity and exhibit strong aging. Different electronic and ionic processes with distinct activation energies may contribute to AC and DC conductivity. Dielectric spectroscopy performed by Morozov and Damjanovic [146] allowed to discriminate between AC processes involving a short-distance migration of charge carriers and quasi-DC processes provided by the charge migration over longer distances in $Pb(Zr_{0.58}Ti_{0.42})_{1-x}Me_xO_3$ with Me = Fe or Nb. Fig. 33 (top) demonstrates the saturation of $\omega\varepsilon''$ that is reached at low frequencies ω indicating DC conductivity. Moreover, DC conductivity exhibits an Arrhenius-type temperature dependence in both Nb- and Fe-doped PZT as is shown in Fig. 33 (bottom). Increasing doping leads to an enhanced DC conductivity in the acceptor (Fe) doped material, but to a reduced DC conductivity in the donor (Nb) doped one. The former reveals considerably larger

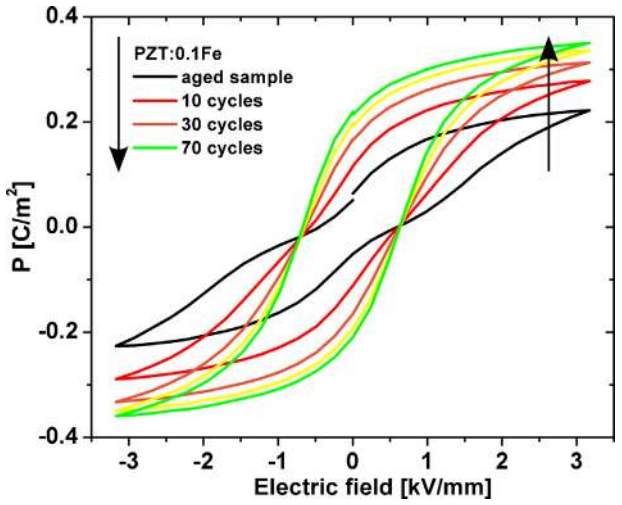

Fig. 30. De-aging of 0.1% Fe-doped $Pb(Zr_{0.54}Ti_{0.46})O_3$ subject to several cycles of bipolar sinusoidal electric field with amplitude of 5 kV/mm and frequency of 55 mHz (Glaum et al. [143]).

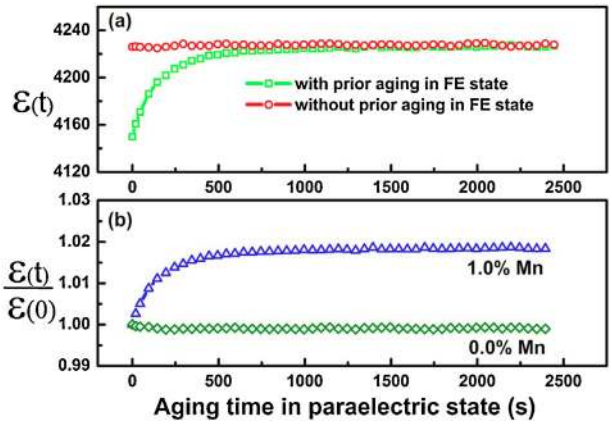

Fig. 32. Evolution of the dielectric permittivity in the paraelectric state of Mn-doped BST: (a) with and without previous aging in the ferroelectric state, (b) as compared to the non-doped material (Xue et al. [144], Zhou et al. [145]).

conductivities and smaller activation energies (slope of Arrhenius plots) than the latter. In turn, activation energies of the DC conductivity are remarkably larger than those of the AC conductivity in acceptor doped materials (see Fig. 34).

The observation that characteristic energies of de-aging and of the ac-conductivity are very similar (see Fig. 34) allows to conclude that pinching and de-pinching transformations of the polarization loops are associated with the local re-orientation of defect dipoles formed by acceptors and oxygen vacancies [146].

On the other hand, further opening of the hysteresis loop toward a more rectangular shape [70] seems to be related to long-range charge redistribution involving higher activation energies typical for DC conductivity. The latter is indicative for the dominant role of ionic conduction in hard PZT-based materials, namely hopping of oxygen vacancies. This understanding is supported by data from Smyth et al. [147,148], which reveal the ionic nature of the conductivity with typical hopping energies of oxygen vacancies around 1 eV.

Different experiments present evidences in favor of defect dipole re-orientation due to oxygen vacancy hopping within one

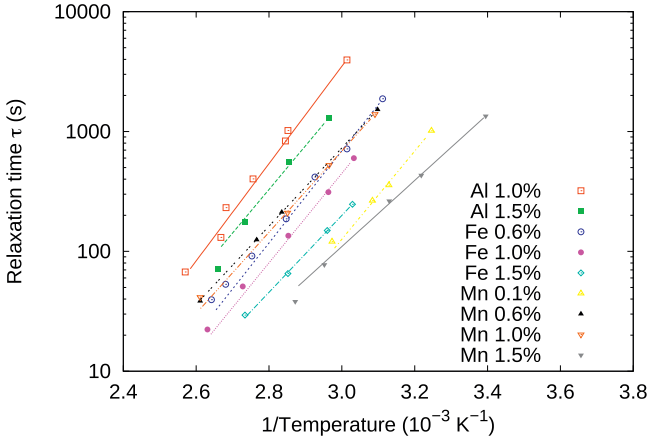

Fig. 31. Temperature and concentration dependence of the de-aging time under bipolar cycling with 2.5 kV/mm at 50 mHz for different dopants (Carl et al. [12]).

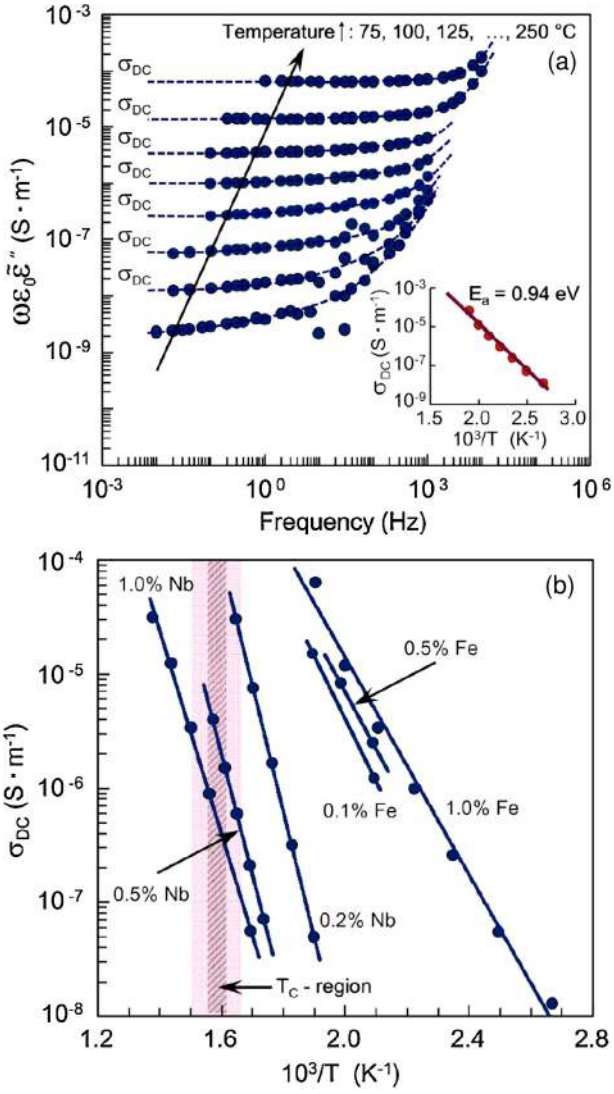

Fig. 33. (a) The frequency dispersion of the imaginary part of the permittivity for hard (1 at.% Fe-doped) PZT (58/42) ceramics; the inset shows the temperature dependence of the DC conductivity and the related activation energy. (b) Arrhenius plots for temperature dependence of the DC conductivity in Fe- and Nb-doped PZT with different doping levels (Morozov et al. [146]).

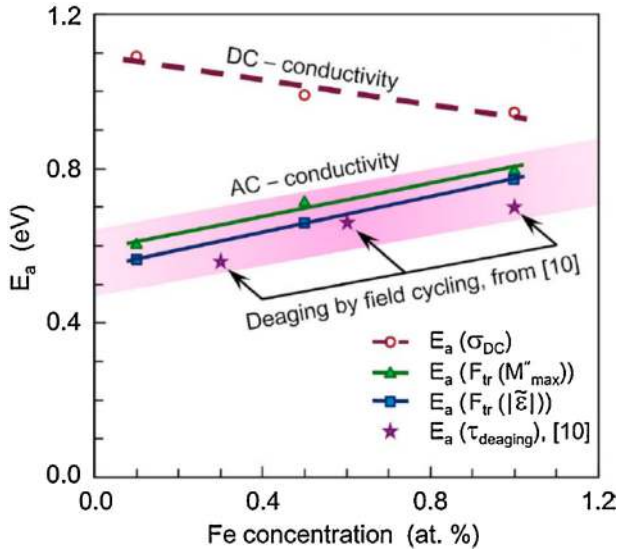

Fig. 34. The doping dependences of the activation energies for the DC and AC conductivities in Fe-doped PZT [146] together with activation energies for de-aging (Carl et al. [12]).

crystal cell and, at a longer time scale, of the charge migration over longer distances. Thus, formation of polar associates $(Fe' - V_O^{\bullet\bullet})^{\bullet}$ [149] and $(Cu'' - V_O^{\bullet\bullet})^{x}$ [64] in Fe- and in Cu-doped $PbTiO_3$, respectively, and their expected orientation along the spontaneous polarization were established by EPR. The observation of aging during two weeks in the single domain poled state of Mn-doped $BaTiO_3$ [150] points to a bulk effect due to re-orientation of defect dipoles as opposed to domain wall and grain boundary mechanisms, related to charge migration over longer distances. In this experiment, however, a charge accumulation in a low-dielectric constant or non-switching nearby-electrode layer [151] can hardly be excluded. In another recent experiment, resistive switching to a metal-like state was observed for $PbTiO_3$ samples previously aged for 24 years and then annealed in the ferroelectric state at 720 K [152,153]. The samples of the same batch annealed in the paraelectric phase at 820 K as well as fresh ceramics have not revealed such properties. This observation can be understood by the accumulation of charged defects on internal interfaces such as domain walls and grain boundaries, where the charge migration over longer distances is accelerated. In the following sections, we will discuss to which extent first-principles calculations and phenomenological models can explain the experimentally observed aging features.

4. Point defects and dipoles

The influence of point defects on aging and fatigue of ferroelectrics has been investigated for a long time [68,70,73,154,155], as outlined in the previous sections. Especially the role of oxygen vacancies that (i) form defect associates with acceptors and (ii) can contribute to charge transport by ionic motion has been subject of a number of detailed studies [64,156–162].

A direct quantitative analysis of defect concentrations and mobilities is experimentally challenging, since there is a wide range of possible defect reactions that can lead to the formation of vacancies and defect associates in ferroelectric materials. Traditionally, the defect chemistry of perovskites is discussed in the framework of the Brouwer approximation [163,164]. However, with the increasing performance of electronic structure calculations that allow to calculate defect formation energies of individual, differently charged defect types, there is now a conceptually more fundamental approach to address the problem of defect equilibria in metal oxides and to quantify, which concentrations can be expected under equilibrium conditions (see e.g. Refs. [165–168]). In the following, we will briefly describe the methodology of ab-initio thermodynamics of defects and then discuss results from first-principles calculations on the formation and switching of defect associates in the context of aging and fatigue.

4.1. Defect formation

Conceptually, the formation energy of a point defect in charge state q depends on the chemical potentials μ_i of the constituents ("the chemical environment") and the electron chemical potential μ_e as follows [169,170],

$$\Delta G^d = (G_{def} - G_{host}) - \sum_j \Delta n_j \mu_j + q(E_{\mathrm{VBM}} + \mu_e), \tag{1}$$

where G_{def} and G_{host} are the Gibbs free energies of the system with and without the defect, respectively. The difference in the number of atoms of type i between these two systems is denoted Δn_j and the sum runs over the elements present in the system. It is convenient to separate the chemical potential into the chemical potential of the ground state μ_j^0 and the variation relative to the ground state chemical potential $\Delta\mu_j$, i.e.

$$\mu_j = \mu_j^0 + \Delta\mu_j. \tag{2}$$

Finally, the position of the valence band, E_{VBM}, defines the reference of the energy scale for the electron chemical potential, μ_e.

Knowledge of the defect formation energy allows to calculate the defect concentration as a function of temperature, which is given by

$$c_i^d = c_i^0 \exp\left(-\frac{\Delta G_i^d(\mu_j, \mu_e)}{k_B T}\right), \tag{3}$$

where c_i^0 denotes the number of sites available for defects on the respective sublattice per volume.

The electron chemical potential μ_e, which appears in Eq. (1), is actually not a free parameter but fixed by the charge neutrality condition [171],

$$n_e + n_A = n_h + n_D, \tag{4}$$

which links the concentration of intrinsic electrons n_e and holes n_h to the concentration of charge carriers induced by acceptors n_A and donors n_D.

The formation energy given in Eq. 1 can be directly calculated from electronic structure calculations. In supercell calculations finite-size effects are an important issue, which needs to be addressed [167,172,173]. However, in oxide materials the dielectric screening is sufficiently large so that elecrostatic multipole interactions play a minor role, if the supercell geometries are chosen accordingly. Erhart et al. [162,174] have carried out a self-consistent treatment of intrinsic defects in the prototypical ferroelectric $BaTiO_3$ that provides an excellent testbed for a stringent comparison between calculated and experimental data. In Fig. 35 the grand-canonical phase diagram is shown that defines the stability limits of cubic $BaTiO_3$.

The formation energies for various intrinsic point defects are shown in Fig. 36 for different equilibrium conditions. The large formation enthalpy of $BaTiO_3$ is the reason that the defect formation energies vary strongly with the chemical equilibrium conditions. In the metal-rich limit (along A–B) oxygen vacancies prevail. They have comparably small formation energies and therefore are abundant defects. Note that the formation energies become negative

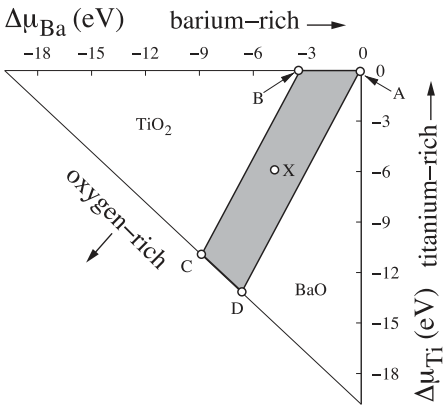

Fig. 35. Stability diagram for cubic barium titanate as determined from density functional theory calculations. The area confined between points A, B, C and D is the chemical stability range of $BaTiO_3$. The line through points C and D corresponds to maximally oxygen-rich conditions and an oxygen chemical potential of $\Delta\mu_O = 0$ eV. Along lines parallel to C–D the oxygen chemical potential is constant. The most negative value of $\Delta\mu_O = \Delta H_f/3 = -6.61$ eV is obtained in the upper right corner of the diagram (point A). (Erhart et al. [174],).

for certain Fermi levels which determines the so-called pinning energy, ε_{pin}. This implies that under equilibrium conditions the material cannot assume a Fermi level which is closer to the valence band maximum than ε_{pin} [170].

If the Fermi level position would electrochemically be shifted beyond one of the pinning levels, defect formation would be thermodynamically favorable and occur spontaneously if kinetically allowed. Local defect generation might thus be the reason for inhomogeneous polarization or structural degradation. Recent experimental studies of interfaces of $BaTiO_3$ and other perovskites with metal and oxide electrodes [175–178] have revealed by photoelectron spectroscopy that the variation of Fermi level positions is comparable in the bulk, at the surface, and at interfaces of these oxides. The electrochemical stability limit may be reached at any of these locations.

4.2. Dipole formation

In a seminal paper, Lambeck and Jonker [179] proposed that the aging phenomenon is due to a gradual alignment of defect dipoles in the perovskite lattice. From the analysis of the hysteresis loop and microscopical observation of moving domain walls, they concluded that the ferroelectric domain stabilization in Mn-doped $BaTiO_3$ crystals is due to bulk effects. Electron paramagnetic spin resonance (ESR) measurements revealed that in reduced crystals $(Mn''_{Ti} - V_O^{\bullet\bullet})^x$ associates exist, having an excess orientation parallel to the spontaneous polarization [74,180,181]. In lead based perovskites a variety of defect associates exists including $(Cu''_{Ti/Zr} - V_O^{\bullet\bullet})^x$ [64,182] and $(Fe'_{Ti/Zr} - V_O^{\bullet\bullet})^\bullet$ [62,183–187] that have been confirmed by ESR data and electronic structure calculations.

Also, in the lead-free piezoelectric sodium potassium niobate (KNN) two kinds of mutually compensating charged defect associates were recently observed, namely the $(Cu''_{Nb} - V_O^{\bullet\bullet})'$

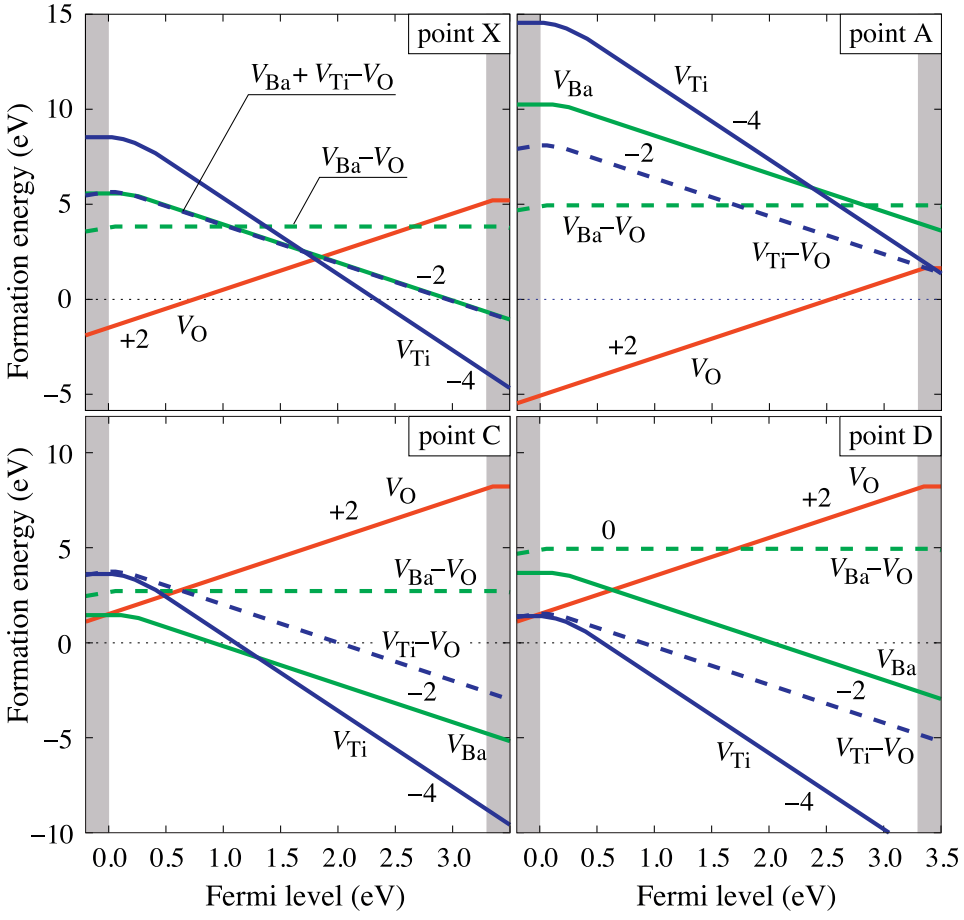

Fig. 36. Variation of defect formation energies with Fermi level for representative thermodynamic conditions indicated in Fig. 35. The numbers indicate the charge states. Parallel lines correspond to identical charge states. The solid and dashed lines correspond to mono and di-vacancies, respectively (Erhart et al. [162]).

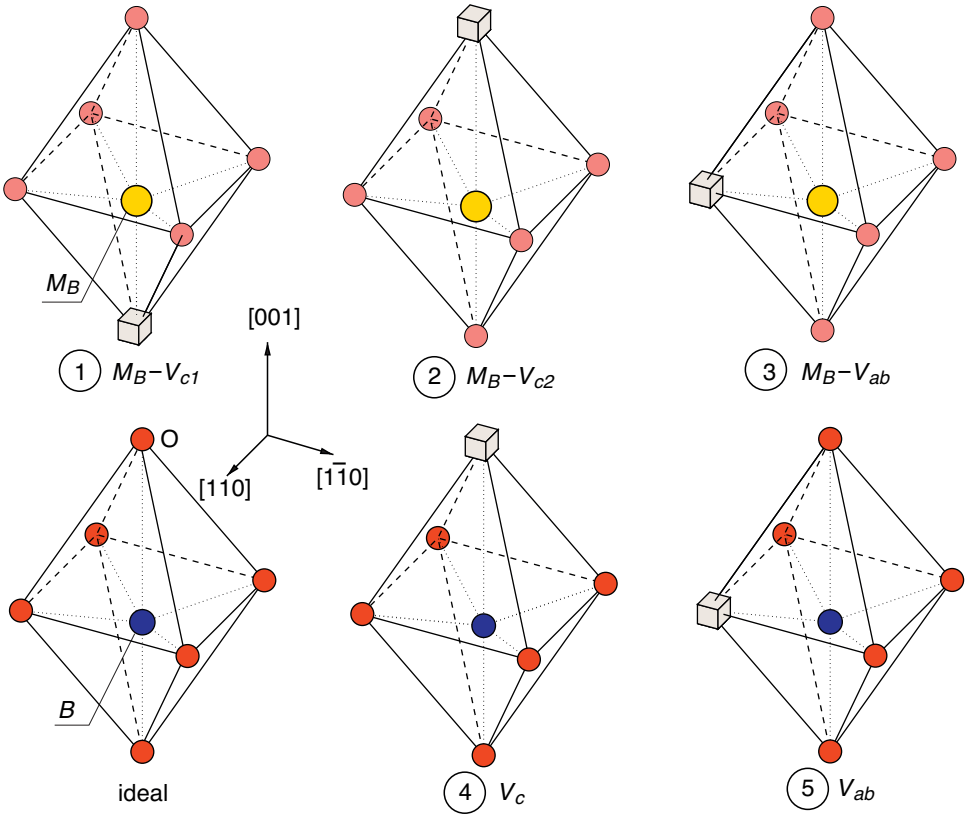

Fig. 37. Unit cell of a tetragonal perovskite (ABO_3) lattice. Shown are three possible configurations for the dipole-acceptor associate. (1) Showing the configuration, where the microdipole is aligned parallel to the spontaneous polarization, (2) is representing the case of antiparallel orientation, and (3) is showing the configuration with the microdipole perpendicular to the to the spontaneous polarization. The vacancy positions in the matrix material are shown in (4) and (5). Note that vacancy configurations along the *c*-axis in the undoped unit cell are equivalent, while the presence of the dopant breaks the symmetry and allows to distinguish the two distinct configurations.

and $(V_O^{\bullet\bullet} - Cu''_{Nb} - V_O^{\bullet\bullet})^{\bullet}$ defect associates [47]. Similarly, for $[Bi_{1/2}Na_{1/2}]TiO_3$ ferroelectrics clear evidence for the existence of $(Fe'_{Ti} - V_O^{\bullet\bullet})^{\bullet}$ microdipoles was found [188,189] which explains the "hardening" effect in Fe_2O_3-doped samples (Fig. 37).

While there is no doubt about the existence of microdipoles of vacancy–acceptor pairs at ambient conditions, much less is known on their thermodynamic stability [190]. For the ionic conductor $SrTiO_3$, e.g. it was shown by temperature dependent ESR-measurements, that iron-vacancy associates dissolve at elevated temperatures. For the Cu- and Fe-doped ferroelectric $PbTiO_3$ DFT calculations have been recently carried out by Erhart et al. [68].

The binding energy of Cu''_{Ti} with the oxygen vacancy was calculated for various positions and distances between both defects (see Fig. 38). Vacancies in the direct neighbor shell of the dopant exhibit thermodynamically significant binding energies larger than −0.5 eV. Thus, the dissociation reaction $(Cu''_{Ti} - V_O^{\bullet\bullet})^{x} \rightleftharpoons Cu''_{Ti} + V_O^{\bullet\bullet}$ is fully on the left hand side at ambient conditions and even at typical processing temperatures where the oxygen diffusivity is sufficiently high. Thus, in equilibrium all dopants should be decorated by a vacancy and only a small fraction of thermal vacancies does exist. At this point it is worth to note that comparable binding energies were also found for the defect associate $(Cu''_{Nb} - V_O^{\bullet\bullet})'$ in KNN [47].

Next to the acceptor–vacancy complexes also intrinsic vacancy associates do exist. Cockayne and Burton [158] showed by means of DFT calculations that the $(V''_{Pb} - V_O^{\bullet\bullet})^{x}$ vacancy associate has a significant dipole moment. Similarly, Erhart and Albe [174] calculated for the $(V''_{Ba} - V_O^{\bullet\bullet})^{x}$ di-vacancy and the $(V''''_{Ti} - V_O^{\bullet\bullet})''$ di-vacancy in $BaTiO_3$ binding energies of −0.62 eV and −1.93 eV, respectively (see Fig. 39).

In a recent paper Eichel [155] sketched the defect equilibria in a Brouwer-diagram for acceptor doped $Pb(Zr,Ti)O_3$ as shown in Fig. 40. From the calculated binding energies of di-vacancy and acceptor-vacancy complexes it can be concluded that these associates acting as microdipoles are the prevailing defect types at large dopant concentrations.

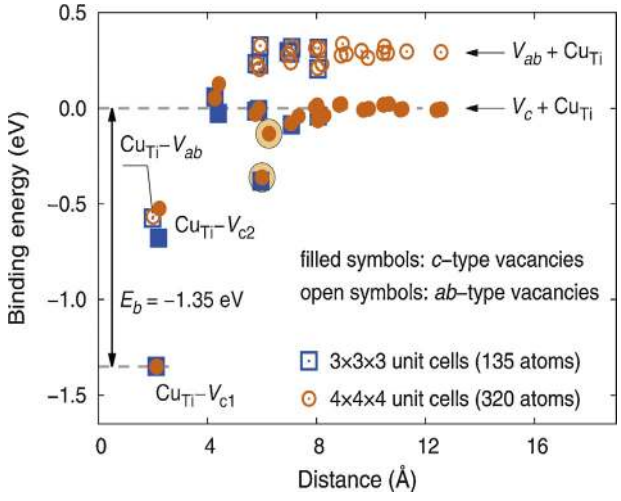

Fig. 38. Binding energy of the $(Cu''_{Ti} - V_O^{\bullet\bullet})^{x}$ defect associate in $PbTiO_3$ calculated for various distances between the vacancy and the Cu dopant. The reference energy is the formation energy of the isolated Cu''_{Ti} and $V_O^{\bullet\bullet}$ position on the *c*-axis of the oxygen octhedron (Erhart et al. [68]).

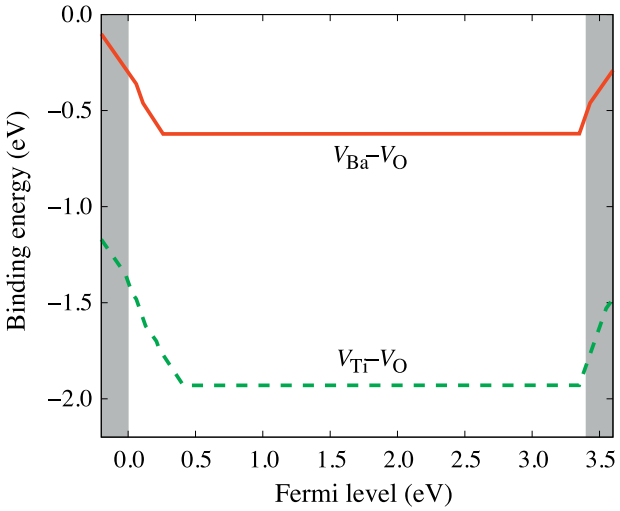

Fig. 39. Calculated binding energy of divacancies in $BaTiO_3$ as a function of the Fermi energy. The kinks are due to charge transition points of the isolated defects (Erhart et al. [68]).

4.3. Dipole switching

The ability to observe the alignment of defect dipoles by EPR had a broad impact on the understanding of materials degradation with time. The characteristic time scales for the switching kinetics with and without field are, however, difficult to resolve by experimental means. At this point advances have been made by DFT calculations.

Defect complexes such as di-vacancies or impurity-vacancy associates carry a dipole moment (see e.g. Ref. [158] for a quantitative calculation). On a cubic lattice different orientations of these microdipoles are energetically degenerate. In the presence of an electric field [73,191] or for non-cubic lattices [184] this degeneracy is, however, lifted (i.e. the energies for di-vacancy pairs e.g. oriented along the [001] and [100] axes differ). Depending on the barriers the transition temperature and the cooling rate defect dipoles might not have enough time to achieve the orientation with the lowest energy. Since metal vacancies are rather immobile, reorientation of these dipoles is much more likely to occur by oxygen vacancy jumps. The gradual re-orientation of defect dipoles is then determined by the barrier for oxygen vacancy jumps in the first neighborhood of metal vacancies.

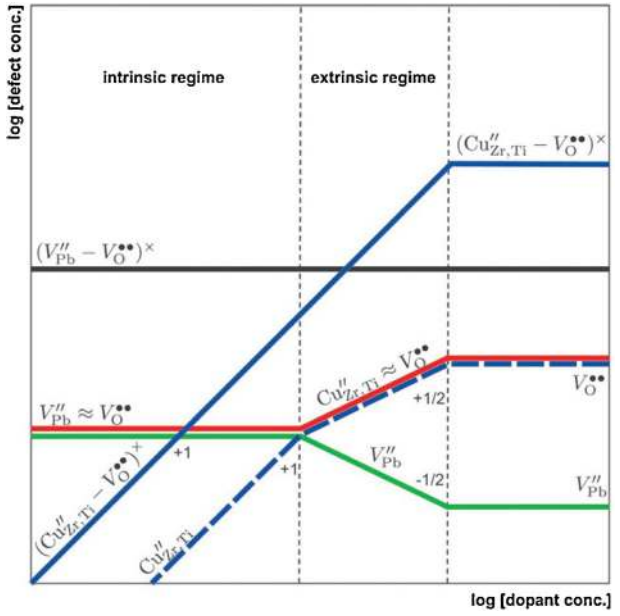

Fig. 40. Schematic draft of defect concentrations in PZT as a function of copper-doping considering the presence of defect associates (Eichel [155]).

Arlt and Neumann [73,191] have attributed the occurrence of internal bias fields to the switching of defect dipoles and described the transient orientation of dipoles by a kinetic model based on a simple electrostatic estimate of the energy difference. They obtained for the energetic asymmetry between the parallel and anti-parallel dipoles in doped $BaTiO_3$ about 30 meV and thus a much smaller value than the energy differences calculated more recently by first-principles methods for $PbTiO_3$, [69,192,193] which revealed that the energetic asymmetry is actually as large as the barriers for oxygen migration. Marton and Elsässer [194] showed by DFT calculations that in Fe-doped lead titanate the barrier for reorientation also depends on the position of the migrating oxygen vacancy with respect to the iron atom and the spontaneous polarization. During fast field cycling, the defect-dipoles are expected not to change orientation, because the characteristic rate for oxygen jumps around the acceptor center should be lower than the domain switching process.

Experimentally, Zhang et al. [180] studied the dynamics of $(Mn''_{Ti} - V''_O)^x$ dipoles in barium titanate by electron paramagnetic resonance studies and found evidence that non-switching defect dipoles impose a restoring force for reversible domain switching [75]. Jakes et al. could show that in Fe^{3+} doped PZT defect dipoles are not preferentially located at domain walls but within the domains [195]. Morozov et. al. [70] studied aging–deaging processes in hard PZT ceramics and assigned an activation energy of about 0.6 eV to short-range charge hopping, which could be due to local reorientation of microdipoles.

Similar values were found in recent calculations on migration barriers [68] ranging from 0.62 to 1.17 eV for the various possible vacancy jumps in the vicinity of the Cu dopant (see Fig. 41). Slighly lower values are found for the Fe-vacancy associate.

Erhart et al. [68] used the calculated migration barriers to determine the effective jump rates and solved a set of rate equations in order to determine the population of the distinct vacancy positions with time. The temporal evolution of the relative vacancy concentrations is exemplarily shown in Fig. 42 for a temperature of 300 K and a Cu dopant concentration of 5%. Initially, all vacancies are statistically distributed, then the vacancy distribution changes in three stages. At the first stage unbound vacancies move to the energetically preferred V_c sites. Then dopants begin to capture vacancies and $Cu_{Ti} - V_{c2}$ associates dominate over $Cu_{Ti} - V_{c1}$ and $Cu_{Ti} - V_{ab}$ dipoles, since they are more easily accessible even though energetically less favored. Finally, vacancy–dopant associates take over with $Cu_{Ti} - V_{c1}$ being the dominant defect, where virtually all vacancies occupy the lowest energy site. At this time the material has reached the fully aged state, which for the given model parameters occurs after several days at room temperature.

Fig. 43 shows the vacancy redistribution of an aged sample after an oscillating field is applied in the model. The plot shows that a dynamic balance between the two dipole orientations is established with time.

Bipolar cycling leads to a dynamic equilibrium between defect dipoles that are aligned parallel and anti-parallel to the lattice polarization, respectively, and thus can be seen as one major contribution to deaging of PZT ceramics. This is in line with the experimental observation of deaging by the application of AC fields [143,196]. In Cu-doped lead titanate the dynamic equilibration takes several months at 300 K, but is massively accelerated if temperature is slightly increased. In Fe-doped samples the process

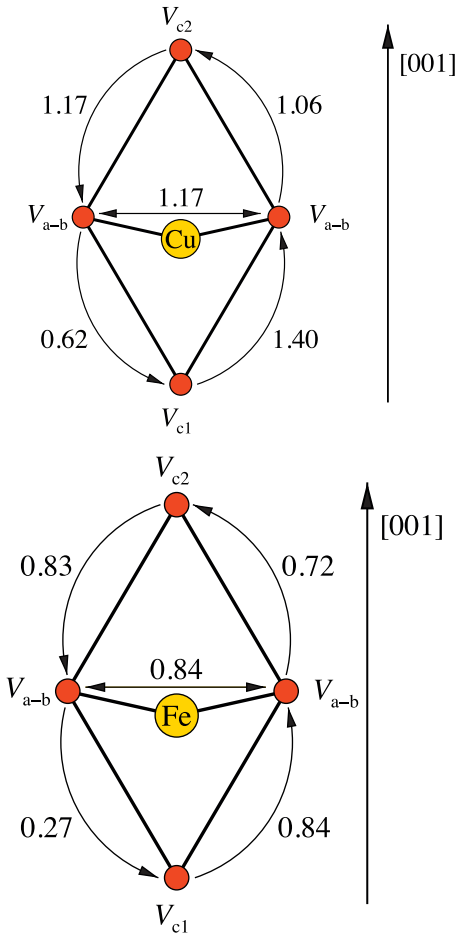

Fig. 41. Activation barriers of complexed oxygen vacancies in the vicinity of Cu in units of eV. The figure shows the projection of a BO_6 octahedron onto the (1 0 0) plane. Possible vacancy sites are shown as red circles while the position of the Cu-cation is shown in yellow. (For interpretation of the references to color in this figure legend, the reader is referred to the web version of this article.)
Figure taken from [68]

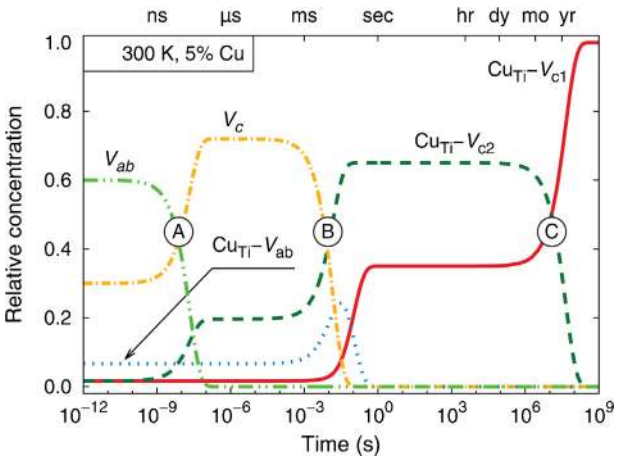

Fig. 42. Vacancy redistribution in the absence of electric field for Cu-doped lead titanate. Shown is the temporal evolution of the relative concentrations of different vacancy types at a temperature of 300 K and for a Cu concentration of 5% (Erhart et al. [68]).

takes, however, only about two weeks. This points to the importance of closely monitoring the sample temperature during testing and studying aging and deaging processes.

For the M_B–V_{c1} associate, which for both Cu and Fe is the ground state configuration, the local polarization is parallel to the polarization of the surrounding matrix [69]. Since, in contrast, M_B–V_{c2} defects are aligned anti-parallel to the lattice polarization, an increase in their concentration causes an overall loss of switchable polarization. This direct contribution scales linearly with the number of impurity atoms in the sample. In lead titanate and tetragonal PZT one typically observes 90° domain wall configurations, as schematically indicated in Fig. 44. It has been shown by first-principles calculations that the head-to-tail domain wall configuration as shown in Fig. 44, is energetically more stable than head-to-head or tail-to-tail configurations [197]. In the pristine material after cooling (middle panel of Fig. 44) all defect dipoles are aligned with the lattice polarization and thus follow the

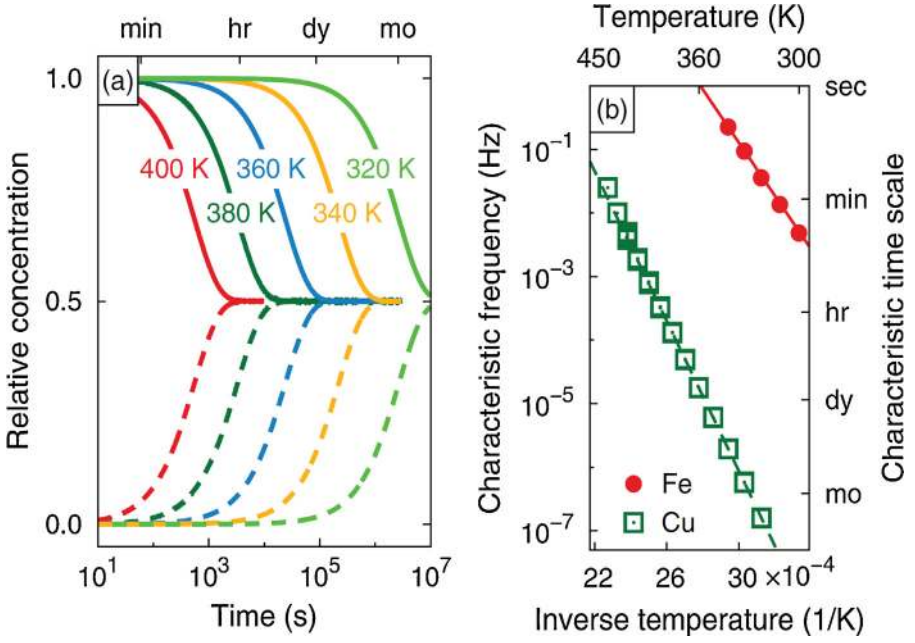

Fig. 43. Vacancy redistribution in the presence of an external bipolar field oscillating with 1 Hz: (a) equilibration over vacancy types $Cu_{Ti} - V_{c1}$ (solid lines) and $Cu_{Ti} - V_{c2}$ (dashed lines), (b) temperature dependence of time after which the relative concentration of M_B–V_{c1} associates is reduced to 55% where M is either Cu or Fe (Erhart et al. [68]).

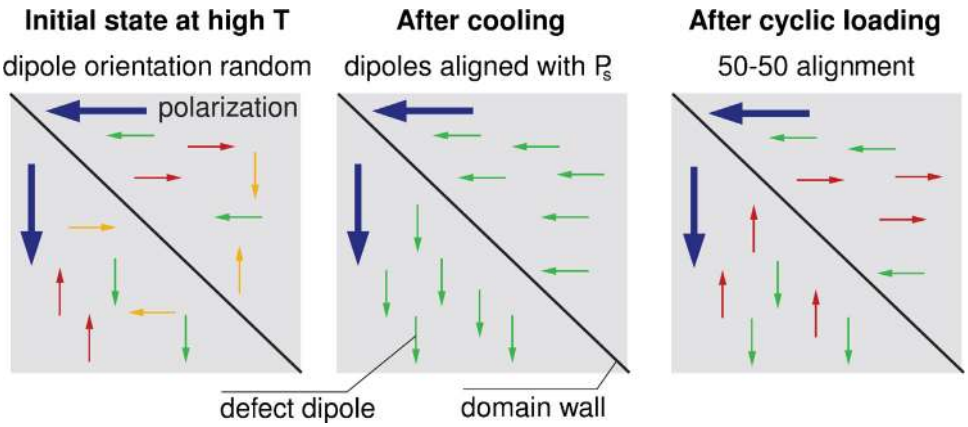

Fig. 44. Defect dipole rearrangements for different conditions. The large value arrows indicate the matrix polarization in different domains while the small arrows represent defect dipoles. The thick solid line illustrates the position of a 90° domain wall (Erhart et al. [68]).

head-to-tail pattern. This situation changes significantly after cyclic loading (right panel of Fig. 44), since now half of the defect dipoles oppose the lattice polarization and thus create local high-energy head-to-head and tail-to-tail configurations. Even though the direct contribution of defect dipoles to the macroscopic polarization is small they can have a significant indirect impact by pinning domain walls and reducing their mobility. Since domain wall motion occurs via nucleation and growth [198], it should be strongly influenced by local defect dipoles.

5. Drift-diffusion models

5.1. Charge migration model for aging

The role of space charges of various natures – electronic, ionic or mixed – was discussed in many studies in the context of aging and fatigue of ferroelectrics [12,142,199]. A realistic quantitative model for bulk ferroelectrics, however, has not been elaborated for a long time because 2D or 3D treatments are rather complicated and simple one-dimensional (1D) considerations are only relevant for a parallel plate capacitor geometry [200,201]. A consistent 1D-consideration makes sense only for peculiar domain arrangements, where the electric field is localized by screening, such as tail-to-tail and head-to-head configurations [202]. Nevertheless, a 1D model can be used for estimating upper limits of clamping forces exerted upon domain walls due to aging by the space-charge mechanism [203].

5.2. 2D drift-diffusion model of aging in unpoled ceramics

In disordered, particularly in polycrystalline ferroelectrics internal bound charges due to discontinuities of polarization at domain and grain boundaries cannot be completely deleted because of random crystallite orientations. This causes local remnant depolarization fields inside a bulk material. If some mobile charge species are available inside the grains or in grain boundaries, they will be driven by the depolarization fields in order to compensate their sources, namely, the remnant bound charges. Thus the main hypotheses of a model describing a space charge evolution include (i) the presence of local depolarization fields at least near charged faces of domains, for example, at grain boundaries, and (ii) availability of mobile charged defects, presumably oxygen vacancies introduced by acceptor doping, as discussed before in Section 4. Oxygen vacancies with small but finite mobility are considered as a main agent of space charge formation, because they can be present in amounts sufficiently high to substantially compensate bound charges at the domain boundaries according to intentional or unintentional acceptor doping [204], in contrast to much more mobile but sparse intrinsic electronic charge carriers.

To describe the field-driven charge migration in unpoled ferroelectrics a two-dimensional (2D) model of an isolated ferroelectric grain was suggested [205], which allows detailed tracing of the space charge formation and increasing stabilization of a domain pattern during aging. The geometry of the problem is presented in Fig. 45. An isolated quadratic grain is filled with a periodic array of domains cut by the interfaces with surrounding dielectric. If the length of the domains L is much larger than their width a, which is typically the case in experiments, electric field lines are effectively closed at the same side of the grain. Finite-element simulations of the electric field in the finite domain array show a virtually periodic field pattern along the x-axis everywhere except for the ends of the array [206]. Therefore a periodic domain array along the x-axis can be considered as a representative model for a finite multidomain grain. Since the depolarization field of a domain array decays exponentially at the scale of the domain width a,

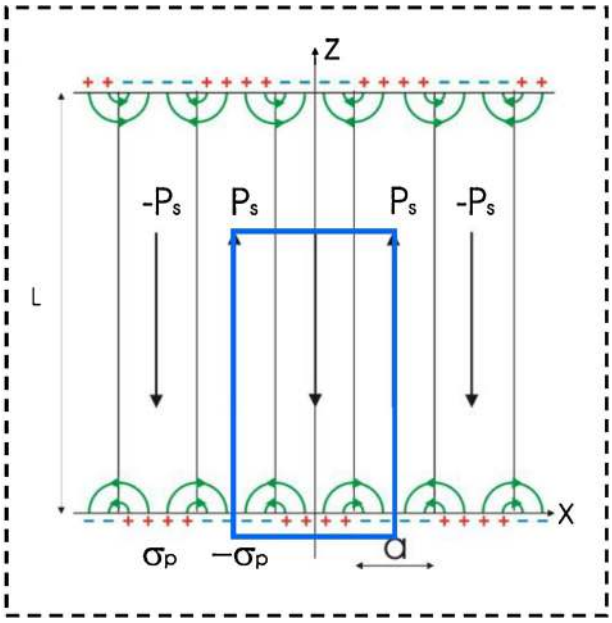

Fig. 45. Sketch of a two-dimensional ferroelectric grain filled with a 180-domain array (Genenko et al. [205]). Straight black and semicircle green arrows indicate polarization and electric field vectors, respectively. Blue frame displays the representative area for which the numerical analysis is performed.

it suffices to assume the intergrain spacing larger than a to get the neighbor grains electrically decoupled. For simplicity, both dielectric and ferroelectric media are assumed to be isotropic and only the redistribution of oxygen vacancies within the grain is considered although oxygen migration through grain boundaries can also significantly contribute to aging [207].

The evolution of the system is governed by the coupled Poisson and drift-diffusion equations:

$$\nabla \mathbf{F} = \frac{q}{\varepsilon_f \varepsilon_0}(c - c_0) \tag{5a}$$

$$\frac{\partial c}{\partial t} = -\nabla(\mu\, c\mathbf{F}) + D\Delta c \tag{5b}$$

where $\mathbf{F}$ is the electric field, c and c_0 the concentrations of positively charged mobile species (oxygen vacancies) and negatively charged immobile species (acceptor ions), respectively, q, D and μ are the charge, the diffusivity and the mobility of mobile species, respectively. We assume, for simplicity, that the two latter quantities are isotropic and connected by the Einstein relation, $D = \mu kT/q$, with k the Boltzmann constant and T absolute temperature.

By quenching the as-prepared material from high to room temperature, oxygen vacancies are distributed uniformly so that they locally compensate the background charge density of acceptors. Thus, in the initial state the right-hand side of Eq. (5a) is zero. As soon as a domain pattern is formed below the ferroelectric transition temperature, the emerging depolarization fields start to move charged species along the field lines. This motion progressively reduces the depolarization fields until the equilibrium at a lower energy is reached. In the final aged state, the diffusion current is outweighed by the drift so that the right-hand side of Eq. (5b) vanishes. Due to charge migration oxygen vacancies are accumulated in a thin layer in front of the negatively charged domain faces while the negative space charge due to uncompensated acceptors emerges in front of positively charged domain faces. Energy gain in the unpoled aged state hinders polarization switching of the system if an external electric field is applied. This explains the pinched polarization loop in Figs. 26 and 27. The strength of this hindrance is characterized by the internal bias field E_{bias} which was introduced in Section 3.

The system of Eqs. (5) was numerically solved for differently acceptor doped $BaTiO_3$ [208] and the field E_{bias} was evaluated as a function of time. The bias field increases with time and reaches maximum after a characteristic aging time τ_r (Fig. 46, top) while the maximum of E_{bias} increases with doping and saturates at $c_0 \cong 0.5\,\%$ (Fig. 46, bottom). The saturation of E_{bias} with doping by arbitrary acceptors in the range $c_0 \cong 0.5$ and 2% is also observed in experiments (Fig. 29).

Particularly, it was noted by Morozov that changes in P–E loops of PZT are well pronounced already at very small concentration of Fe and then saturate fast so that the responses of samples doped with 0.5 at.% Fe or higher concentrations are almost indistinguishable [139]. This fast and nonlinear doping dependence is in agreement with calculation results shown in Fig. 46 (bottom). Also shown here is the inverse aging time which exhibits virtually linear dependence on doping.

Saturation of E_{bias} as well as the reduction of aging time with increasing concentration c_0 has a simple physical reason. The depth h of the space–charge area emerging near the positively charged domain face is defined by the amount of acceptors needed to fully compensate the surface bound charge P_s and is of the order of P_s/qc_0. For a concentration of c_0=1 mol% the depth is about 5 nm which is by orders of magnitude smaller than the domain width a. This means that, at such high concentrations, the electrostatic depolarization field is compensated virtually in the whole specimen volume due to charge migration so that the maximum possible energy gain and,

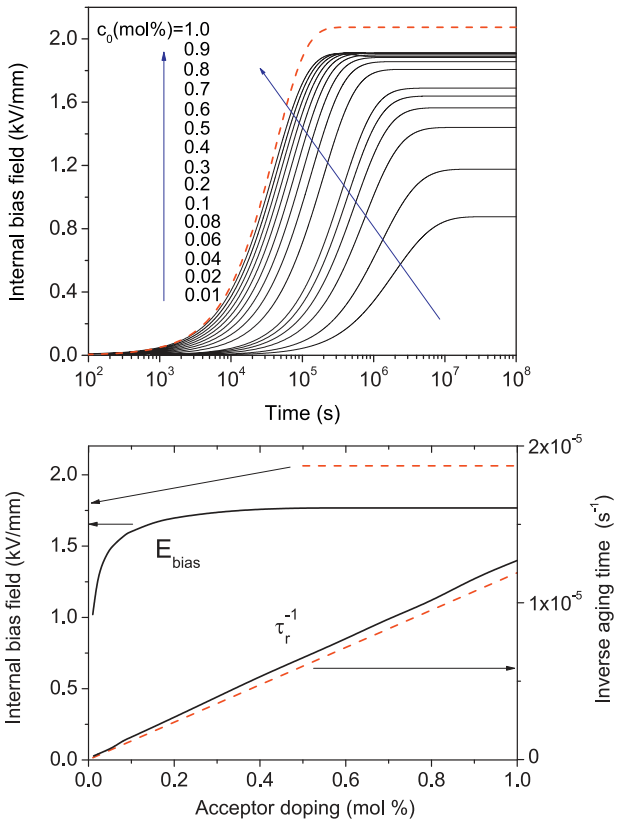

Fig. 46. Time dependence of the internal bias field E_{bias} at different acceptor doping levels as indicated (top). Dependence of the saturated internal bias field E_{bias} and of the inverse aging time $1/\tau_r$ on the acceptor concentration (bottom) (Genenko [208]). Analytical results are shown with dashed lines while numerical results are indicated with solid lines.

consequently, the maximum magnitude of E_{bias} is achieved, which is concentration independent. The aging time τ_r is determined, in turn, by the distance h the charge carriers have to cover and is obviously proportional to $h/\mu E_z(0) \propto 1/c_o$.

For moderate doping levels $c_0 > 0.5\%$ the equation system (5) can be solved analytically (dashed lines in Fig. 46). The internal bias field in this limit is given by the formula

$$E_{\text{bias}}(t) \cong \frac{0.85}{\pi}\frac{a}{L}\frac{P_s}{\varepsilon_0\varepsilon_f}\left[1 - \exp\left(\frac{-t}{\tau_r}\right)\right] \tag{6}$$

with the aging time τ_r presented by the Maxwell relaxation time due to ionic conductivity

$$\tau_r = \varepsilon_0(\varepsilon_f + \varepsilon_d)/q\mu c_0. \tag{7}$$

This aging time is temperature dependent due to the temperature dependence of permittivity and the thermally activated mobility $\mu \propto \exp(-E_a/kT)$ where E_a is the activation energy of the ionic DC conductivity discussed in Section 3, see particularly Fig. 33. In fact, the activation energy for the migration of oxygen vacancies in many perovskites is still not known accurately and often estimated as $E_a = (1 \pm 0.1)$ eV. Assuming as in Ref. [209] that E_a is a spatially random variable distributed with a Gaussian $\approx \exp[-(E_a - \bar{E})^2/2s^2]$ and using $\bar{E} = 1$ eV and $s/\bar{E} = 0.1$, E_{bias} can be averaged over this distribution resulting in a quasi-logarithmic time dependences shown by the dashed lines for different temperatures in Fig. 47.

These dependences properly capture main observed features of the evolution of the internal bias field with time and temperature presented in Fig. 28 and provide the field and aging time amplitudes comparable with experimental ones.

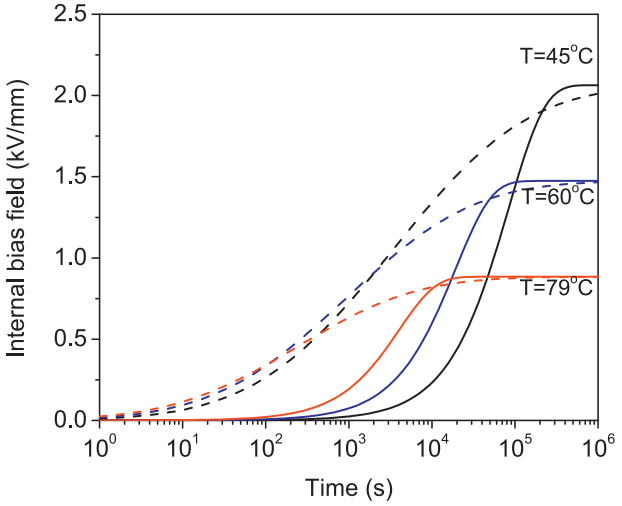

Fig. 47. Time dependence of the internal bias field E_{bias} at different temperatures in unpoled $BaTiO_3$ for an acceptor doping level of 1%. Solid lines assume a unique value of the activation barrier for migration of 1 eV. Dashed lines assume randomly distributed activation energies in the range 1 ± 0.1 eV (Genenko [208]).

5.3. 3D drift-diffusion model of aging in poled ceramics

A model of poled PZT ceramics [210] is represented by a regular cubic lattice of equal tightly contacted single-crystalline cubic grains of mesoscopic size R adopting single domain states Fig. 48 (top). Crystal axes orientations in different grains are supposed to be absolutely arbitrary and uncorrelated. Mismatching polarizations of neighboring grains result in uncompensated local bound charges producing depolarization fields even in the poled state. The variance of local field fluctuations in this model is about $P_s/4\pi\varepsilon_0\varepsilon_f \approx 10^7$ V/m which exceeds by far typical coercive fields $E_c \approx 10^6$ V/m. Such high fluctuation fields ΔE_d cannot be realized for various physical reasons. The most straightforward one is building of domains (neglected in the actual model) until the local field ΔE_d falls below the coercive field. Another one is the field screening of the semiconducting nature discussed in the next section. In any case the remnant field ΔE_d will be assumed smaller than E_c.

If mobile charge defects with concentration c_0 are present (e.g. oxygen vacancies), they will be driven by the local fields ΔE_d until the local bound charges are compensated (if the quantity of mobile charges suffices). To this end, they have to cover distances of $h \cong P_s/q_f c_0$ estimated in the previous section and amounting to few nm which is much smaller than a typical grain size of 1 μm. This results, like in the above case of unpoled ferroelectrics, in a time dependent internal bias field $E_{bias}(t) = \Delta E_d[1 - \exp(-t/\tau_r)]$ with the aging time given by the same Maxwell relaxation time τ_r as in the unpoled case. Averaged over the distribution of activation energies in the range 1 ± 0.1 eV the time dependences of E_{bias} are shown in Fig. 48 (bottom) by dashed lines for different doping levels together with experimental data for Fe-doped PZT shown by solid lines [210]. *P–E* loops in this case retain their shape but are shifted along the field axis by E_{bias} as in Fig. 26c.

5.4. Space charge effects in ferroelectrics with semiconducting features

Local depolarization fields in both cases of poled and unpoled ferroelectrics play a crucial role in the space charge mechanism of aging. However, calculated within a dielectric model of ferroelectrics they appear to be far too large in comparison with coercive fields as mentioned above. On the other hand, they produce electrostatic potential variations exceeding typical band gaps

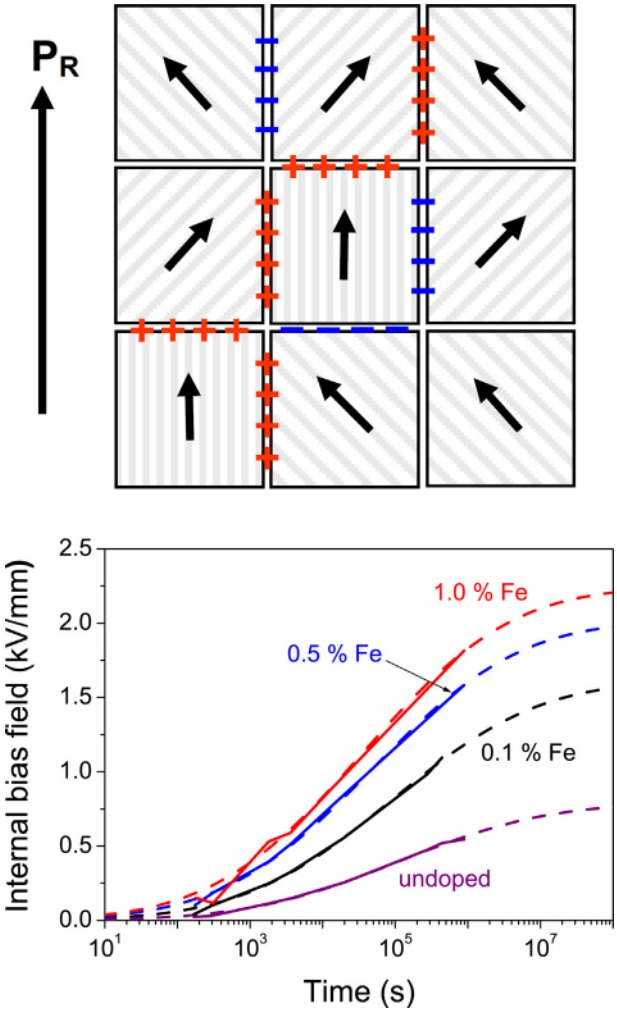

Fig. 48. Scheme for a 3D regular array of arbitrary oriented single crystalline cubic grains (top). Time dependent experimental (solid lines) and theoretical (dashed lines) magnitudes of the internal bias field in poled bulk PZT (bottom) (Genenko et al. [210]).

of ferroelectric perovskites as indicated by Watanabe [211]. This means that they should cause substantial band bending which in turn creates local space charge pockets of electrons and holes screening the electric field. These effects make it necessary to consider ferroelectrics as wide-band semiconductors and account for the interplay of all charged species involved: electrons, holes and charged defects.

Considering an unpoled ferroelectric grain within the 2D frame presented in Fig. 45 and using the nonlinear Poisson equation [211], which accounts self-consistently for all typical intrinsic charged defects in $BaTiO_3$ [162,174], reveals the following traits of nonlinear field screening [212]. While in the absence of free charges the electrostatic potential varies periodically along the ferroelectric/dielectric interface sweeping symmetrically the range from −3V to +3V (solid line in Fig. 49a), the presence of electronic carriers reduces this range to exactly the magnitude of the band gap of this compound $E_g = 3.4$ eV. Further account of charged defects shifts the mean value of the surface potential from zero to a positive value depending on the concentration of defects and their energy levels.

This surface potential is related to an effective dipole layer which is formed at the interface $z = 0$ as is seen from the potential step in Fig. 49b. The physical reason of the effective dipole layer is the distinction between the extensions of space charge regions in front of the positive and the negative domain boundaries

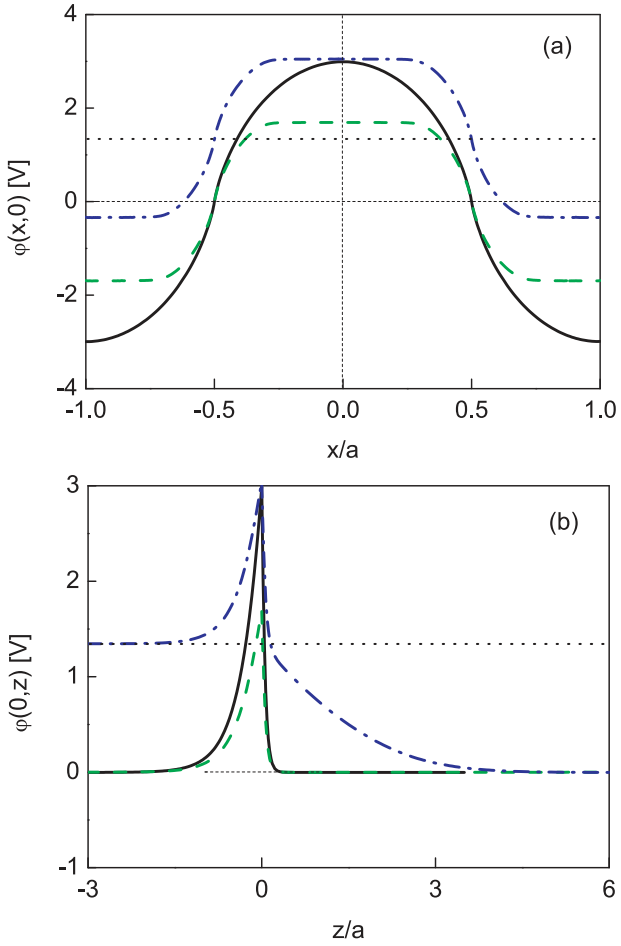

Fig. 49. Electrostatic potential profiles in x direction along the ferroelectric/dielectric interface at $z=0$ (a) and perpendicular to the latter along the line $x=0$ (b) referred to the blue frame in Fig. 45. Black solid lines show profiles in the absence of free charges, the green dashed lines account for the electronic charges p and n only, while the dash-dotted lines account for both electronic and defect charges. The thin dotted horizontal line indicates the mean value of the potential (Genenko et al. [212]).

depending on the nature and amount of dopants. Introduction of extrinsic acceptor or donor dopants changes the sign and magnitude of the surface potential but not the variance of the electrostatic potential which remains equal to E_g. Physical consequences from this fact are that, (i) the surface potential should trigger charge migration to grain boundaries at a larger scale than the domain width a, and (ii) the depolarization fields in ferroelectrics are globally restricted by the maximum electrostatic potential variation of E_g. The latter fact sets upper bounds to local depolarization fields of $E_{max} \cong E_g/a \approx 10^7$ V/m » E_c in unpoled ferroelectrics and of $E_{max} \cong E_g/R \approx 10^6$ V/m ≃ E_c in poled ceramics. Since the grain size R decreases monotonically with increasing doping c_0 [210], the field E_{max} limiting the internal bias field E_{bias}, has to increase, too, which is in agreement with results in Fig. 48 (bottom). The latter conclusion revises the statement on the doping independence of E_{max} in [210] where the semiconducting screening of the depolarization fields was not considered.

5.5. Phase-field modeling of ferroelectrics with semiconducting features

Semiconducting features have also a great impact on formation and stabilization of domain structures in ferroelectrics. Based on the approach by Bhattacharya [213–215] and continuum mechanic models [216,217], 2D phase-field simulations have been performed

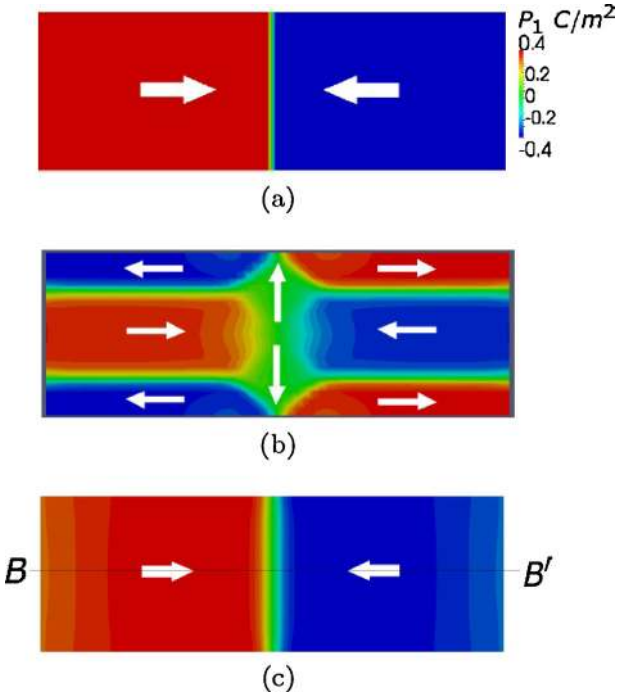

Fig. 50. (a) The initial head-to-head domain configuration. (b) The equilibrium domain configuration without semiconducting features. (c) The equilibrium domain configuration with an oxygen vacancy concentration of $N_d = 5 \times 10^{23}$ m^{-3} (Zuo et al. [218]).

by means of the finite-element method, which show that the consideration of electronic carriers and charged defects modifies stripe domain arrays and, particularly, makes otherwise unstable head-to-head and tail-to-tail domain configurations possible [218] and electrically conducting [219]. The latter two configurations were recently considered theoretically [202] and observed experimentally [220,221].

In the phase field model, mechanical and electrical phenomena are considered in a coupled way, as is necessary in electrostrictive and piezoelectric materials, with account of the spontaneous strain and polarization. Evolution of an initial trial structure proceeds according to a kinetic equation formulated in the spirit of the time dependent Ginzburg–Landau approach [218]. Exemplarily, an effect of space charges on equilibrium 2D domain configurations in barium titanate is displayed in Fig. 50. The left and the right boundaries of the computation frame are short-circuited, i.e. set potential-free, while the top and the bottom boundaries are set charge-free. All the boundaries are supposed to be traction-free. Starting from the initial head-to-head domain configuration (Fig. 50a) the system develops spontaneously to a periodic stripe-like structure (Fig. 50b) which exhibits 180°- as well as 90°-domain walls, if no space charges are involved. This is in contrast to the phase-field modeling by Wang and Kamlah [222], where the domain configuration in a ferroelectric nanotube was imposed by a prescribed surface charge density. If, however, a sufficient amount of donors (oxygen vacancies) is introduced, the initial head-to-head configuration is stabilized and remains stable also with respect to rotation (Fig. 50c).

The described domain formation with account of semiconductor properties is a fast process resulting in a domain pattern with extended space charge regions near the domain walls with an uncompensated polarization bound charge. Within these space charge regions, a significant depolarization field is still present which should drive the much slower ionic charge carriers like oxygen vacancies thus providing aging according to the space charge mechanism.

6. Summary

The physical mechanisms underlying aging and fatigue of ferroelectrics have much in common. The latter phenomenon, however, involves a much wider variety of causes and regimes of material degradation, depending on loading conditions, device geometry etc.

Thus, we will start the conclusions with the more general case of aging mechanisms and then summarize the current status on the understanding of fatigue mechanisms.

6.1. Aging

Considering the classification of aging mechanisms into bulk, domain and interface effects (e.g. grain boundaries) as suggested by Carl and Härdtl [12] it can be concluded that all three groups deal with mobile, mostly charged defects and thus are closely related to issues such as intrinsic defects and doping of materials. Depending on the materials composition, crystal structure and dopants the resulting defects can move over a short-range (hopping within a crystal unit cell) or a long-range (several unit cells) distance. The former mechanism particularly backs up reorientation of defect dipoles [73,179], while the latter contributes to long-range charge transport, i.e. DC conductivity, and eventually results in formation of space charge of any nature (ionic or electronic) [199].

Short- and long-range motion/rearrangement of most mobile defects in perovskites – oxygen vacancies – can explain the majority of observed aging features, such as stabilization of domain patterns in poled and unpoled states, pinching and/or shifting of polarization loops and gradual deterioration of dielectric and piezoelectric properties. Especially, much can be learned from experiments on de-aging of the aged samples by heating above the Curie temperature or by application of an AC field. These are able to shed some light on the nature of a particular aged state.

Thus, experiments on opening of the pinched polarization loops by application of an AC field in PZT doped with different acceptors [12,143] and on AC conductivity in Fe-doped PZT [146] exhibit characteristic activation energies about $E_a \sim 0.5$–0.7 eV. The recovery of the dielectric permittivity induced by heating of Mn-doped $BaTiO_3$ above T_c [144] exhibits an activation energy of $E_a = 0.43$ eV similar to the values observed for Fe-doped PZT. The corresponding characteristic times typically show Arrhenius temperature behavior, strong dependence on the type and concentration of dopants [12] and are by orders of magnitude shorter than characteristic aging times observed in the same materials [12,73]. These phenomena can be attributed to the short-range motion of oxygen vacancies, particularly, to defect dipole re-orientation. The related energies and aging times are in agreement with DFT calculations [69,174,223] and kinetic simulations [68].

On the other hand, the further opening of the pinched polarization loops in Fe-doped PZT up to their virgin, rectangular form [146], like that in Figs. 7 and 8(b), as well as the shifting of the P–E loop in the poled state, as in Fig. 48, needs much longer times [210]. Typical activation energies for these processes are about $E_a \sim 0.9$–1.2 eV and coincide with activation energies of DC conductivity in these materials [146,224]. Such activation energies can satisfactorily explain the time, temperature and doping concentration dependence of aging in acceptor doped $BaTiO_3$ [73,208]. These phenomena can thus be attributed to the long-range migration of oxygen vacancies [146] and are characterized by the Maxwell relaxation time. It is worth noting that fast Maxwell times related to free electrons or holes available in perovskites have nothing to do with aging processes because the density of these charge carriers is far too small to compensate bound charges originating from the mismatch of local polarizations. Oxygen vacancies, in contrast, are always available in perovskites in concentrations 10^{20}–10^{26} m^{-3} depending on the kind of doping and the presence of other intrinsic defects [162,174]. Because of these high concentrations, oxygen vacancies do not need to cover macroscopic distances to compensate internal bound charges. In both cases of unpoled [208] and poled [210] ferroelectrics it suffices when they move over several crystal unit cells covering a few nanometers.

Thus, both short-range rearrangement and long-range migrations of oxygen vacancies obviously contribute to aging of ferroelectric materials. The proportions of these two contributions depend on processing conditions, dopant concentration and material type, which all determine the fraction of acceptor-oxygen vacancy or divacancy complexes. The availability of different vacancies of constitutive elements depending on the fabrication process and, particularly, on the ambient oxygen pressure has therefore to be taken into account [162,174].

6.2. Fatigue

The orientation of polar defects in the bulk and agglomeration of charge defects at internal interfaces expected in the case of aging may also contribute to fatigue phenomena. The latter, however, involve additionally various reversible and irreversible changes in the material. The relation between reversible and irreversible fatigue features is clearly seen in degradation of switching kinetics in the course of the bipolar cycling and a subsequent recovery by heating above the phase transition temperature. Strong reduction of maximum and remanent polarization values and slowing down of switching kinetics are typical of fatigue in the case of bipolar loading (Fig. 11). Thereby fatigue in PZT ceramics exhibits two different mechanisms at work: one leading to a (reversible) reduction of the switchable volume of the sample and another leading to (irreversible) changes which cause the slow polarization dynamics. While the latter persistent effect is related to crack formation after long cycling (more than 5×10^7 cycles for PIC 151), the former reversible one, accompanied by variation in dielectric and piezoelectric properties, can be completely removed by annealing at high temperature of 400 °C for 24 h [96]. The fatigued state can also be relaxed by application of an AC field of large amplitude [12,143].

Similar to aging, a shift of the polarization P–E loop occurs, for all large and small signal hysteresis loops in the case of a DC electric load or a unipolar cycling field, in the direction anti-parallel to the applied field polarity and is described as a bias field E_{bias} [80]. Typically, increasing the cycling field amplitude above the coercive field leads to stronger degradation of both dielectric and piezoelectric parameters. This indicates that additionally polarization and related bound charges and/or strains substantially contribute to the gradual transformation of the material, which is also in agreement with the bulk and interface aging mechanisms.

Reversible fatigue features, however, extend far beyond the before mentioned mechanisms related to aging. This holds especially true for more complicated loading regimes, like sesquipolar and bipolar electric cycling. In these cases, phenomena like kinetic imprint [225] and piezoelectric blocking of polarization [226] were predicted in numerical simulations. These mechanisms may also result in irreversible damage due to microcracking during long cycling periods. General experimental observations reveal the longest lifetimes when no electric field is applied, which are progressively reduced when applying electric load from unipolar to sesquipolar to bipolar.

Mechanical preload has ambigous effects. On the one hand, the combination of a fixed mechanical pre-load with a bipolar electric signal leads to better fatigue resistivity of the polarization with increasing preload for soft PZT disk specimen [105]. On the other hand, mechanical preload was observed to provide faster fatigue degradation in the case of unipolar electric loading [227].

Other important factors with impact on fatigue behavior are temperature and the frequency of electric cycling. Fatigue features are more severe at lower temperatures [87] which can be related to higher spontaneous polarizations. For bipolar electric cycling of ferroelectric PLZT as well as soft PZT ceramics, increasing frequency results in decreasing fatigue degradation.

The electrode-ceramic interface can strongly influence the dielectric properties, especially for thin films. The work function of the electrode material can determine whether or not the charge injection during electric field application occurs, which can even affect the phase stability of a material. Eventually, it may cause delamination of the electrodes or changes of the material microstructure [228]. The observed effects, however, do not present an unanimous picture. For example, no substantial differences in bipolar fatigue behavior were found for soft PZT ceramics coated with Pt, RuO_2 or tin-doped In_2O_3 [229], irrespective of the work functions being significantly different [116]. Related to the electrode issue, some fatigue features appear to be relevant to concrete device geometries, particularly, due to partially very inhomogeneous and concentrated electric field distributions in them. Thus managing device geometries and manufacturing of electrode-ceramic interfaces can help to avoid phenomena like electric breakdown and crack formation.

The issue of phase transformations during fatigue appears to be one of the most significant findings of late. As was recently established by in-situ measurements [48], phase changing may occur in a reversible way during routinely polarization switching. When in the course of fatigue some phase becomes stabilized, this results in a substantial reduction of achievable strain.

Acknowledgements

The financial support from the German Science Foundation (DFG) of the collaborative research center SFB 595 “Electrical fatigue in functional materials” for three funding periods (2003–2014) is gratefully acknowledged. The authors thank all former and present colleagues that contributed to this work, namely N. Balke, A.G. Balogh, W. Becker, C. Björn, M. Blömker, P. Braga Groszewicz, H. Breitzke, G. Buntkowsky, K.-P. Dinse, R. Dittmer, W. Donner, P. Erhart, R. Eichel, E. Erdem, C. Feng, H. Fueß, S. Gottschalk, O. Goy, T. Granzow, D. Gross, S. Gumann, S. Hayn, M. Hinterstein, S. Hummelt, H.-J. Kleebe, A. Klein, J. Kling, J. Koruza, H. Kungl, S. Laubach, St. Laubach, D. Lupascu, V. Mehling, H. Mestric, R. Müller, N. Nestle, F. Pforr, W. Rheinheimer, J. Rödel, E. Sapper, R. Schafranek, R. Schierholz, T. Schlegel, P.C. Schmidt, Ch. Schmitt, L. Schmitt, T. Schrade, K. Seifert, H. von Seggern, K. Webber, B. Xu, Y. Xu, S. Yampolskii, M. Zakhozeva, S. Zhukov, R. Zuo, Y. Zuo.

References

[1] W. Heywang, K. Lubitz, W. Wersing (Eds.), Piezoelectricity – Evolution and Future of a Technology, Springer Series in Materials Science, vol. 114, 2008.
[2] K. Uchino, J. Electroceram. 20 (2007) 301.
[3] N. Setter (Ed.), Piezoelectric Materials and Devices, Ceramics Laboratory EPFL, Lausanne, 2002.
[4] Y. Xu, Ferroelectric Materials and their Applications, Elsevier, Amsterdam, 1991.
[5] J.-M. Sallese, P. Fazan, Sens. Actuat. A 109 (2004) 186.
[6] B.C.W.R.J.H. Jaffe, Piezoelectric Ceramics, Academic Press, London/New York, 1971.
[7] M.J. Hoffmann, H. Kungl, Curr. Opin. Solid State Mater. Sci. 8 (2004) 51.
[8] E. Achleitner, S. Berger, H. Enzel, M. Klepatsch, V. Warnecke, MRT Worldwide 65 (2004) 2.
[9] C.A. Randall, A. Kelnberger, G.Y. Yang, R.E. Eitel, T.R. Shrout, J. Electroceram. 14 (2005) 177.
[10] R. Payri, F.J. Salvador, J. Gimeno, J. De la Morena, Appl. Energy 88 (2011) 1068.
[11] R. Payri, F.J. Salvador, J. Gimeno, J. De la Morena, Appl. Energy 88 (2011) 1130.
[12] K. Carl, K. Härdtl, Ferroelectrics 17 (1978) 473.
[13] D. Lupascu, J. Rödel, Adv. Eng. Mater. 7 (2005) 882.
[14] EU-Directive 2002/95/EC, Restriction of the Use of Certain Hazardous Substances in Electrical and Electronic Equipment (RoHS), Off. J. Eur. Union, 46 [L37], Tech. rep., 2003.
[15] EU-Directive 2002/96/EC, Waste Electrical and Electronic Equipment (WEEE), Off. J. Eur. Union, 46 [L37], Tech. rep., 2003.
[16] J. Rödel, W. Jo, K.T.P. Seifert, E.-M. Anton, T. Granzow, D. Damjanovic, J. Am. Ceram. Soc. 92 (2009) 1153.
[17] T. Takenaka, K.-I. Maruyama, K. Sakata, Jpn. J. Appl. Phys. 30 (1991) 2236.
[18] L.A. Schmitt, K.A. Schönau, R. Theissmann, H. Fuess, H. Kungl, J. Michael, M.J. Hoffmann, J. Appl. Phys. 101 (2007) 074107.
[19] M. Hinterstein, K.A. Schönau, J. Kling, H. Fuess, M. Knapp, H. Kungl, M.J. Hoffmann, J. Appl. Phys. 108 (2010) 024110.
[20] A.M. Glazer, K.Z. Baba-Kishi, G.K.H. Pang, C.W. Tai, Phys. Rev. B 70 (2004) 184123.
[21] N.J. Donnelly, T.R. Shrout, C.A. Randall, J. Am. Ceram. Soc. 90 (2007) 490.
[22] R. Zuo, C. Ye, X. Fang, J. Li, J. Eur. Ceram. Soc. 28 (2008) 871.
[23] M. Chen, Q. Xu, B.H. Kim, B.K. Ahn, J.H. Ko, W.J. Kang, O.J. Nam, J. Eur. Ceram. Soc. 28 (2008) 843.
[24] B.-J. Chu, D.-R. Chen, G.-R. Li, Q.-R. Yin, J. Eur. Ceram. Soc. 22 (2002) 2115.
[25] J. Suchanicz, Ferroelectrics 172 (1995) 455.
[26] J. Suchanicz, J. Kusz, H. Bo, H. Duda, J.P. Mercurio, K. Konieczny, J. Eur. Ceram. Soc. 23 (2003) 1559.
[27] Y. Makiuchi, R. Aoyagi, Y. Hiruma, H. Nagata, T. Takenaka, Jpn. J. Appl. Phys. 44 (2005) 4350.
[28] Y. Hiruma, H. Nagata, T. Takenaka, Jpn. J. Appl. Phys. 45 (2006) 7409.
[29] W.E.N. Chen, Y. Li, Q. Xu, J. Zhou, J. Electroceram. 15 (2005) 229.
[30] X.X. Wang, S.H. Choy, X.G. Tang, H.L.W. Chan, J. Appl. Phys. 97 (2005) 104101.
[31] S.-T. Zhang, A.B. Kounga, E. Aulbach, H. Ehrenberg, J. Rödel, Appl. Phys. Lett. 91 (2007) 112906.
[32] S.-T. Zhang, A.B. Kounga, E. Aulbach, W. Jo, T. Granzow, H. Ehrenberg, J. Rödel, J. Appl. Phys. 103 (2008) 034108.
[33] E. Dul'kin, E. Mojaev, M. Roth, W. Jo, T. Granzow, Scripta Mater. 60 (2009) 251.
[34] M. Ahtee, A.M. Glazer, Acta Crystallogr. A 32 (1976) 434.
[35] M. Ahtee, A.W. Hewat, Acta Crystallogr. A 34 (1978) 309.
[36] L. Egerton, D.M. Dillon, J. Am. Ceram. Soc. 42 (1959) 438.
[37] D. Damjanovic, J. Am. Ceram. Soc. 88 (2005) 2663.
[38] Y. Saito, H. Takao, T. Tani, T. Nonoyama, K. Takatori, T. Homma, T. Nagaya, M. Nakamura, Nature 432 (2004) 84.
[39] M.I. Morozov, H. Kungl, M.J. Hoffmann, Appl. Phys. Lett. 98 (2011) 132908.
[40] M.I. Morozov, M.J. Hoffmann, K. Benkert, C. Schuh, J. Appl. Phys. 112 (2012) 114107.
[41] N.M. Hagh, B. Jadidian, E. Ashbahian, A. Safari, IEEE Trans. Ultrason. Ferroelectr. Freq. Control 55 (2008) 214.
[42] M. Matsubara, T. Yamaguchi, W. Sakamoto, K. Kikuta, T. Yogo, S.-I. Hirano, J. Am. Ceram. Soc. 88 (2005) 1190.
[43] M. Matsubara, T. Yamaguchi, K. Kikuta, S.-I. Hirano, Jpn. J. Appl. Phys. 43 (2004) 7159.
[44] M.N. Hagh, K. Kerman, B. Jadidian, A. Safari, J. Eur. Ceram. Soc. 29 (2009) 2325.
[45] S. Körbel, P. Marton, C. Elsässer, Phys. Rev. B 81 (2010) 174115.
[46] M.J. Hoffmann, H. Kungl, J. Acker, C. Elsässer, S. Körbel, P. Marton, R.-A. Eichel, E. Erunal, P. Jakes, Influence of the A/B stoichiometry on defect structure, sintering and microstructure in undoped and Cu-doped KNN, in: S. Priya, S. Nahm (Eds.), Lead Free Piezoelectrics, Springer Media, New York, 2012.
[47] R.-A. Eichel, E. Erünal, P. Jakes, S. Körbel, C. Elsässer, H. Kungl, J. Acker, M.J. Hoffmann, Appl. Phys. Lett. 102 (2013) 242908.
[48] M. Hinterstein, J. Rouquette, J. Haines, P. Papet, M. Knapp, J. Glaum, H. Fuess, Phys. Rev. Lett. 107 (2011) 077602.
[49] G.A. Schneider, T. Scholz, J. Munoz-Saldana, M.V. Swain, Appl. Phys. Lett. 86 (2005) 192903.
[50] J. Munoz-Saldana, G.A. Schneider, L.M. Eng, Surf. Sci. 480 (2001) L402.
[51] X. Tan, H. He, J.-K. Shang, J. Mater. Res. 20 (2011) 1641.
[52] L.A. Schmitt, R. Theissmann, J. Kling, H. Kungl, M.J. Hoffmann, H. Fuess, Phase Trans. 81 (2008) 323.
[53] R. Theissmann, L.A. Schmitt, J. Kling, R. Schierholz, K.A. Schönau, M. Knapp, H. Kungl, M.J. Hoffmann, J. Appl. Phys. 102 (2007) 079902.
[54] R. Theissmann, L.A. Schmitt, J. Kling, R. Schierholz, K.A. Schönau, H. Fuess, M. Knapp, H. Kungl, M.J. Hoffmann, J. Appl. Phys. 102 (2007) 024111.
[55] C. Ma, X. Tan, J. Am. Ceram. Soc. 94 (2011) 4040.
[56] K.A. Schonau, M. Knapp, H. Kungl, M.J. Hoffmann, H. Fuess, Phys. Rev. B 76 (2007), 144112.
[57] B. Noheda, D.E. Cox, G. Shirane, J.A. Gonzalo, L.E. Cross, S.-E. Park, Appl. Phys. Lett. 74 (1999) 2059.
[58] B. Noheda, J.A. Gonzalo, L.E. Cross, R. Guo, S.-E. Park, D.E.S.G. Cox, Phys. Rev. B 61 (2000) 8687.
[59] R. Guo, L. Cross, S. Park, B. Noheda, D. Cox, G. Shirane, Phys. Rev. Lett. 84 (2000) 5423.
[60] W.L. Warren, D. Dimos, G.E. Pike, K. Vanheusden, R. Ramesh, Appl. Phys. Lett. 67 (1995) 1689.
[61] R.A. Eichel, H. Kungl, M.J. Hoffmann, J. Appl. Phys. 95 (2004) 8092.
[62] H. Mestric, R.-A. Eichel, K.-P. Dinse, A. Ozarowski, J. van Tol, L. Brunel, J. Appl. Phys. 96 (2004) 7440.
[63] E. Erünal, R.-A. Eichel, S. Körbel, C. Elsässer, J. Acker, H. Kungl, M.J. Hoffmann, Funct. Mater. Lett. 03 (2010) 19.
[64] R.A. Eichel, P. Erhart, P. Träskelin, K. Albe, H. Kungl, M.J. Hoffmann, Phys. Rev. Lett. 100 (2008) 095504.

[65] R.-A. Eichel, H. Mestric, H. Kungl, M.J. Hoffmann, Appl. Phys. Lett. 88 (2006) 122506.
[66] R.-A. Eichel, H. Kungl, P. Jakes, Mater. Technol.: Adv. Perf. Mater. 28 (2013) 241.
[67] E. Erdem, H. Kungl, M.J. Hoffmann, A. Ozarowski, J.V. Tol, L.C. Brunel, A. Ferroelectric, IEEE Trans. Ultrason. Ferroelectr. Freq. Control 55 (2008) 1061.
[68] P. Erhart, P. Träskelin, K. Albe, Phys. Rev. B 88 (2013) 024107.
[69] P. Erhart, R.-A. Eichel, P. Träskelin, K. Albe, Phys. Rev. B 76 (2007) 174116.
[70] M.I. Morozov, D. Damjanovic, J. Appl. Phys. 104 (2008) 034107.
[71] G.H. Jonker, J. Am. Ceram. Soc. 55 (1972) 57.
[72] D. Lupascu, J. Rödel, Adv. Eng. Mater. 7 (2005) 882.
[73] G. Arlt, H. Neumann, Ferroelectrics 87 (1988) 109.
[74] L. Zhang, X. Ren, Phys. Rev. B 71 (2005) 174108.
[75] X. Ren, Nat. Mater. 3 (2004) 91.
[76] R.-A. Eichel, J. Electroceram. 19 (2007) 11.
[77] V.S. Postnikov, V.S. Pavlov, S.K. Turkov, J. Phys. Chem. Solids 31 (1970) 1785.
[78] W. Warren, D. Dimos, B. Tuttle, R. Nasby, G. Pike, Appl. Phys. Lett. 65 (1994) 1018.
[79] M. Takahasahi, Jpn. J. Appl. Phys. 9 (1970) 1236.
[80] N. Balke, T. Granzow, J. Rödel, J. Appl. Phys. 105 (2009) 104105.
[81] Y. Zhang, D. Lupascu, E. Aulbach, I. Baturin, A. Bell, J. Rödel, Acta Mater. 53 (2005) 2203.
[82] D.A. Hall, J. Mater. Sci. 36 (2001) 4575.
[83] J. Glaum, T. Granzow, J. Rödel, J. Appl. Phys. 107 (2010) 104119.
[84] N. Balke, Ermüdung von $Pb(Zr,Ti)O_3$ für unterschiedliche elektrische belastungsformen, Ph.D. thesis, Technische Universität Darmstadt, 2006.
[85] N. Balke, D.C. Lupascu, T. Granzow, J. Rödel, J. Am. Ceram. Soc. 90 (2007) 1081.
[86] C. Verdier, D. Lupascu, J. Rödel, J. Eur. Ceram. Soc. 23 (2003) 1409.
[87] D. Wang, Y. Fotinich, G.P. Carman, J. Appl. Phys. 83 (1998) 5342.
[88] Z. Luo, J. Glaum, T. Granzow, W. Jo, R. Dittmer, M. Hoffman, J. Rödel, J. Am. Ceram. Soc. 94 (2011) 529.
[89] H. Simons, J. Glaum, J.E. Daniels, A.J. Studer, A. Liess, J. Rodel, M. Hoffman, J. Appl. Phys. 112 (2012) 044101.
[90] J. Glaum, T. Granzow, L.A. Schmitt, H.-J. Kleebe, J. Rödel, Acta Mater. 59 (2011) 6083.
[91] Z. Luo, T. Granzow, J. Glaum, W. Jo, J. Rödel, M. Hoffman, J. Am. Ceram. Soc. 94 (2011) 3927.
[92] V. Shur, E. Rumyantsev, E. Nikolaeva, E. Shishkin, I. Baturin, J. Appl. Phys. 90 (2001) 6312.
[93] N. Balke, D.C. Lupascu, T. Granzow, J. Rödel, J. Am. Ceram. Soc. 90 (2007) 1088.
[94] D. Lupascu, S. Fedosov, C. Verdier, J. Rödel, H. von Seggern, J. Appl. Phys. 95 (2004) 1386.
[95] S. Zhukov, S. Fedosov, J. Glaum, T. Granzow, Y.A. Genenko, H. von Seggern, J. Appl. Phys. 108 (2010) 014105.
[96] S. Zhukov, Y.A. Genenko, O. Hirsch, J. Glaum, T. Granzow, H. von Seggern, Phys. Rev. B 82 (2010) 014109.
[97] N. Balke, D.C. Lupascu, A. Gruverman, T. Blair, J. Appl. Phys. 100 (2006) 114117.
[98] W. Pan, C. Yue, O. Tosyali, J. Am. Ceram. Soc. 75 (1992) 1534.
[99] E.A. Patterson, D.P. Cann, Appl. Phys. Lett. 101 (2012) 042905.
[100] N. Kumar, D.P. Cann, J. Appl. Phys. 114 (2013) 054102.
[101] P.M. Chaplya, M. Mitrovic, G.P. Carman, F.K. Straub, J. Appl. Phys. 100 (2006) 124111.
[102] H. Kungl, M. Hoffmann, Acta Mater. 55 (2007) 5780.
[103] Q. Jiang, E. Subbarao, L. Cross, J. Appl. Phys. 75 (1994) 7433.
[104] I. Kerkamm, P. Hiller, T. Granzow, J. Rödel, Acta Mater. 57 (2009) 77.
[105] D. Wang, G.P. Carman, Smart Structures and Materials 1998: Smart Structures and Integrated Systems, Pts 1 and 2, vol. 2, 1998, pp. 210.
[106] H. Wang, A.A. Wereszczak, H.-T. Lin, J. Appl. Phys. 105 (2009) 014112.
[107] D.C. Lupascu, E. Aulbach, J. Rödel, J. Appl. Phys. 93 (2003) 5551.
[108] Y. Zhang, X. Cheng, R. Qian, Mater. Sci. Eng. A 351 (2003) 81.
[109] H. Makino, N. Kamiya, Jpn. J. Appl. Phys. 37 (1998) 5301.
[110] M. Lente, J. Eiras, J. Phys.: Condens. Matter 12 (2000) 5939.
[111] N. Zhang, L. Li, Z. Gui, J. Eur. Ceram. Soc. 21 (2001) 677.
[112] S. Pojprapai, J. Russell, H. Man, J.L. Jones, J.E. Daniels, M. Hoffman, Acta Mater. 57 (2009) 3932.
[113] V. Shur, Ferroelectricity and Related Phenomena, vol. 10, Gordon and Breach, Amsterdam, Ch. Fast Polarization Reversal Process: Evolution of Ferroelectric Domain Structure in Thin Films Ferroelectric Thin Films: Synthesis and Basic Properties, 1996.
[114] E. Colla, A. Tagantsev, D. Taylor, A. Kholkin, Integr. Ferroelectr. 18 (1997) 19.
[115] E. Colla, D. Taylor, A. Tagantsev, N. Setter, Appl. Phys. Lett. 72 (1998) 2478.
[116] F. Chen, R. Schafranek, A. Wachau, S. Zhukov, J. Glaum, T. Granzow, H. von Seggern, A. Klein, J. Appl. Phys. 108 (2010) 104106.
[117] S.R. Winzer, N. Shankar, A.P. Ritter, J. Am. Ceram. Soc. 72 (1989) 2246.
[118] J. Thongrueng, T. Tsuchiya, K. Nagata, Jpn. J. Appl. Phys. 37 (1998) 5306.
[119] A. Furuta, K. Uchino, J. Am. Ceram. Soc. 76 (1993) 1615.
[120] F.W. Zeng, H. Wang, H.-T. Lin, J. Appl. Phys. 114 (2013) 024101.
[121] S.-C. Woo, N.S. Goo, Smart Mater. Struct. 18 (2009) 104021.
[122] N.J. Donnelly, C.A. Randall, J. Am. Ceram. Soc. 92 (2009) 405.
[123] L. Andrejs, J. Fleig, J. Eur. Ceram. Soc. 33 (2013) 779.
[124] L. Andrejs, H. Oßmer, G. Friedbacher, J. Bernardi, A. Limbeck, J. Fleig, Solid State Ionics 244 (2013) 5.
[125] E. Sapper, A. Gassmann, L. Gjodvad, W. Jo, T. Granzow, J. Rödel, J. Eur. Ceram. Soc. 34 (2014) 653.
[126] J. Nuffer, D. Lupascu, A. Glazounov, H. Kleebe, J. Rödel, J. Eur. Ceram. Soc. 22 (2002) 2133.
[127] D.A. Hall, T. Mori, T.P. Comyn, E. Ringgaard, J.P. Wright, J. Appl. Phys. 114 (2013) 024103.
[128] J. Nuffer, D.C. Lupascu, J. Rödel, J. Eur. Ceram. Soc. 21 (2001) 1421.
[129] Z. Luo, S. Pojprapai, J. Glaum, M. Hoffman, J. Am. Ceram. Soc. 95 (2012) 2593.
[130] L. Andrejs, H. Oßmer, G. Friedbacher, J. Fleig, J. Eur. Ceram. Soc. 33 (2013) 1165.
[131] J. Nuffer, D. Lupascu, J. Rödel, Appl. Phys. Lett. 80 (2002) 1049.
[132] C. Verdier, D. Lupascu, H. von Seggern, J. Rödel, Appl. Phys. Lett. 85 (2004) 3211.
[133] C. Verdier, D. Lupascu, J. Rödel, Appl. Phys. Lett. 81 (2002) 2596.
[134] V. Shvartsman, A. Kholkin, C. Verdier, D. Lupascu, J. Appl. Phys. 98 (2005) 094109.
[135] V. Shvartsman, A. Kholkin, C. Verdier, Z. Yong, D. Lupascu, J. Eur. Ceram. Soc. 25 (2005) 2559.
[136] S. Tsurekawa, H. Hatao, H. Takahashi, Y. Morizono, Jpn. J. Appl. Phys. 50 (2011) 09NC02.
[137] H. Kungl, M.J. Hoffmann, J. Appl. Phys. 107 (2010) 054111.
[138] M. Hinterstein, J. Rouquette, J. Haines, P. Papet, J. Glaum, M. Knapp, J. Eckert, M. Hoffman, Phys. Rev. B 90 (2014) 094113.
[139] M.I. Morozov, EPFL, Ph.D. thesis, Lausanne, 2005.
[140] L.X. Zhang, X. Ren, Phys. Rev. B 71 (2005) 174108.
[141] H.T.R. Herbiet, G. Arlt, Ferroelectrics 76 (1987) 319.
[142] S. Takahashi, Ferroelectrics 41 (1982) 143.
[143] J. Glaum, Y.A. Genenko, H. Kungl, L.A. Schmitt, T. Granzow, J. Appl. Phys. 112 (2012) 034103.
[144] D. Xue, J. Gao, L. Zhang, H. Bao, W. Liu, C. Zhou, X. Ren, Appl. Phys. Lett. 94 (2009) 082902.
[145] Y. Zhou, D. Xue, X. Ding, L. Zhang, J. Sun, X. Ren, J. Phys.: Condens. Matter 25 (2013) 435901.
[146] M.I. Morozov, D. Damjanovic, J. Appl. Phys. 107 (2010) 034106.
[147] D.M. Smyth, Ferroelectrics 151 (1994) 115.
[148] M.V. Raymond, D.M. Smyth, J. Phys. Chem. Solids 57 (1996) 1507.
[149] H. Mestric, R.-A. Eichel, T. Kloss, K.-P. Dinse, S. Laubach, S. Laubach, P.C. Schmidt, K.A. Schönau, M. Knapp, H. Ehrenberg, Phys. Rev. B 71 (2005) 134109.
[150] L.X. Zhang, X. Ren, Phys. Rev. B 73 (2006) 094121.
[151] A. Tagantsev, I. Stolichnov, E. Colla, N. Setter, J. Appl. Phys. 90 (2001) 1387.
[152] M. Pilch, A. Molak, J. Alloys Compd. 586 (2014) 488.
[153] M. Pilch, A. Molak, K. Szot, Ferroelectrics 466 (2014) 51.
[154] H. Dederichs, G. Arlt, Ferroelectrics 68 (1986) 281.
[155] R.-A. Eichel, Phys. Chem. Chem. Phys. 13 (2011) 368.
[156] C.H. Park, D.J. Chadi, Phys. Rev. B 57 (1998) R13961.
[157] S. Pöykkö, D.J. Chadi, Appl. Phys. Lett. 76 (2000) 499.
[158] E. Cockayne, B.P. Burton, Phys. Rev. B 69 (2004) 144116.
[159] C.H. Park, J. Korean Phys. Soc. 42 (2003) S1420.
[160] L. He, D. Vanderbilt, Phys. Rev. B 68 (2003) 134103.
[161] Z. Zhang, P. Wu, L. Lu, C. Shu, Appl. Phys. Lett. 88 (2006) 142902.
[162] P. Erhart, K. Albe, J. Appl. Phys. 104 (2008) 044315.
[163] R.-A. Eichel, E. Ernal, M.D. Drahus, D.M. Smyth, J. van Tol, J. Acker, H. Kungl, M.J. Hoffmann, Phys. Chem. Chem. Phys. 11 (2009) 8698.
[164] D. Smyth, Ann. Rev. Mat. Sci. 15 (1985) 329.
[165] E. Rauls, T. Frauenheim, Phys. Rev. B 69 (2004) 155213.
[166] S.A. Centoni, B. Sadigh, G.H. Gilmer, T.J. Lenosky, T. Diaz de la Rubia, C.B. Musgrave, Phys. Rev. B 72 (2005) 195206.
[167] P. Erhart, K. Albe, A. Klein, Phys. Rev. B 73 (2006) 205203.
[168] P. Erhart, K. Albe, J. Appl. Phys. 102 (2007) 084111.
[169] G.-X. Qian, R.M. Martin, D.J. Chadi, Phys. Rev. B 38 (1988) 7649.
[170] S.B. Zhang, S.-H. Wei, A. Zunger, Phys. Rev. Lett. 84 (2000) 1232.
[171] A.R. Allnatt, A.B. Lidiard, Atomic Transport in Solids, Cambridge University Press, Cambridge, 2003.
[172] S. Lany, A. Zunger, Phys. Rev. B 78 (2008) 235104.
[173] C. Freysoldt, J. Neugebauer, C.G. Van de Walle, Phys. Rev. Lett. 102 (2009) 016402.
[174] P. Erhart, K. Albe, J. Appl. Phys. 102 (2007) 084111.
[175] R. Schafranek, S. Li, F. Chen, W. Wu, A. Klein, Phys. Rev. B 84 (2011) 045317.
[176] F. Chen, R. Schafranek, S. Li, W.B. Wu, A. Klein, J. Phys. D 43 (2010) 295301.
[177] F. Chen, R. Schafranek, W. Wu, A. Klein, J. Phys. D 44 (2011) 255301.
[178] F. Chen, A. Klein, Phys. Rev. B 86 (2012) 094105.
[179] G.P.V. Jonker, P.V. Lambeck, Ferroelectrics 21 (1978) 641.
[180] L. Zhang, E. Erdem, X. Ren, R.-A. Eichel, Appl. Phys. Lett. 93 (2008) 202901.
[181] L.X. Zhang, X.B. Ren, Phys. Rev. B 73 (2006) 094121.
[182] R.R. Garipov, J.M. Spaeth, D.J. Keeble, Phys. Rev. Lett. 101 (2008) 247604.
[183] H. Meštrić, R.A. Eichel, K.P. Dinse, A. Ozarowski, J. van Tol, L.C. Brunel, H. Kungl, M.J. Hoffmann, K.A. Schönau, M. Knapp, H. Fuess, Phys. Rev. B 73 (2006) 184105.
[184] H. Meštrić, R.-A. Eichel, T. Kloss, K.-P. Dinse, S. Laubach, S. Laubach, P.C. Schmidt, K.A. Schönau, M. Knapp, H. Ehrenberg, Phys. Rev. B 71 (2005) 134109.
[185] M. Iwata, N. Iijima, Y. Ishibashi, Ferroelectrics 428 (2012) 1.
[186] D.J. Keeble, M. Loyo-Menoyo, Z.I.Y. Booq, R.R. Garipov, V.V. Eremkin, V. Smotrakov, Phys. Rev. B 80 (2009) 014101.
[187] S. Pöykkö, D. Chadi, Phys. Rev. Lett. 83 (1999) 1231.
[188] E. Aksel, E. Erdem, P. Jakes, J.L. Jones, R.A. Eichel, Appl. Phys. Lett. 97 (2010) 012903.
[189] W. Ge, H. Cao, J. Li, D. Viehland, Q. Zhang, H. Luo, Appl. Phys. Lett. 95 (2009) 162903.
[190] R. Merkle, J. Maier, Phys. Chem. Chem. Phys. 5 (2003) 2297.
[191] H. Neumann, G. Arlt, Ferroelectrics 76 (1987) 303.

[192] S. Pöykkö, D.J. Chadi, Phys. Rev. Lett. 83 (1999) 1231.
[193] H. Meštrić, R.-A. Eichel, K.-P. Dinse, A. Ozarowski, J. van Tol, L. Brunel, J. Appl. Phys. 96 (2004) 7440.
[194] P. Marton, C. Elsässer, Phys. Rev. B 83 (2011) 020106.
[195] P. Jakes, E. Erdem, R.-A. Eichel, L. Jin, D. Damjanovic, Appl. Phys. Lett. 98 (2011) 072907.
[196] T. Granzow, E. Suvaci, H. Kungl, M.J. Hoffmann, Appl. Phys. Lett. 89 (2006) 262908.
[197] B. Meyer, D. Vanderbilt, Phys. Rev. B 65 (2002) 104111.
[198] Y.-H. Shin, I. Grinberg, I.-W. Chen, A.M. Rappe, Nature 449 (2007) 881.
[199] M. Takahashi, Jpn. J. Appl. Phys. 9 (1970) 1236.
[200] A.K. Tagantsev, I.A. Stolichnov, Appl. Phys. Lett. 74 (1999) 1326.
[201] L. Baudry, J. Appl. Phys. 86 (1999) 1096.
[202] M.Y. Gureev, A.K. Tagantsev, N. Setter, Phys. Rev. B 83 (2011) 184104.
[203] D.C. Lupascu, Y.A. Genenko, N. Balke, J. Am. Ceram. Soc. 89 (2006) 224.
[204] D.M. Smyth, The Defect Chemistry of Metal Oxides, Oxford University Press, New York, 2000, chapter 14.
[205] Y.A. Genenko, D.C. Lupascu, Phys. Rev. B 75 (2007) 184107.
[206] Y.A. Genenko, N. Balke, D.C. Lupascu, Ferroelectrics 370 (2008) 196.
[207] T. Frömling, H. Hutter, J. Fleig, J. Am. Ceram. Soc. 95 (2012) 1692.
[208] Y.A. Genenko, Phys. Rev. B 78 (2008) 214103.
[209] R. Lohkämper, H. Neumann, G. Arlt, J. Appl. Phys. 68 (1990) 4220.
[210] Y.A. Genenko, J. Glaum, O. Hirsch, H. Kungl, M.J. Hoffmann, T. Granzow, Phys. Rev. B 80 (2009) 224109.
[211] Y. Watanabe, Phys. Rev. B 57 (1998) 789.
[212] Y.A. Genenko, O. Hirsch, P. Erhart, J. Appl. Phys. 115 (2014) 104102.
[213] Y. Xiao, V.B. Shenoy, K. Bhattacharya, Phys. Rev. Lett. 95 (2005) 247603.
[214] P. Suryanarayana, K. Bhattacharya, J. Appl. Phys. 111 (2012) 034109.
[215] V.B. Shenoy, Y. Xiao, K. Bhattacharya, J. Appl. Phys. 111 (2012) 084105.
[216] D. Schrade, R. Müller, B.X. Xu, D. Gross, Comp. Meth. Appl. Mech. Eng. 196 (2007) 4365.
[217] B.X. Xu, D. Schrade, R. Müller, D. Gross, T. Granzow, J. Rödel, ZAMM 90 (2010) 623.
[218] Y. Zuo, Y.A. Genenko, A. Klein, P. Stein, B.X. Xu, J. Appl. Phys. 115 (2014) 084110.
[219] Y. Zuo, Y.A. Genenko, B.X. Xu, J. Appl. Phys. 116 (2014) 044109.
[220] D. Meier, J. Seidel, A. Cano, K. Delaney, Y. Kumagai, M. Mostovoy, N.A. Spaldin, R. Ramesh, M. Fiebig, Nat. Mater. 11 (2012) 284.
[221] T. Sluka, A.K. Tagantsev, P. Bednyakov, N. Setter, Nat. Commun. 4 (2013) 1808.
[222] J. Wang, M. Kamlah, Appl. Phys. Lett. 93 (2008) 042906.
[223] A. Chandrasekaran, D. Damjanovic, N. Setter, N. Marzari, Phys. Rev. B 88 (2013) 214116.
[224] S. Gottschalk, H. Hahn, S. Flege, A.G. Balogh, J. Appl. Phys. 104 (2008) 114106.
[225] V.Y. Shur, E.L. Rumyantsev, E.V. Nikolaeva, E.I. Shishkin, I.S. Baturin, J. Appl. Phys. 90 (2001) 6312.
[226] E. Anton, R. Garcia, T. Key, J. Blendell, K. Bowman, J. Appl. Phys. 105 (2009) 024107.
[227] J. Thongrueng, T. Tsuchiya, K. Nagata, Jpn. J. Appl. Phys. 37 (1998) 5306.
[228] N. Balke, H. Kungl, T. Granzow, D.C. Lupascu, M.J. Hoffmann, J. Rödel, J. Am. Ceram. Soc. 90 (2007) 3869.
[229] N. Balke, D.C. Lupascu, A. Gruverman, T. Blair, J. Appl. Phys. 100 (2006) 114117.